

Exploring configuration-based relaxometry and imaging with balanced steady-state free precession

INAUGURALDISSERTATION

zur

Erlangung der Würde eines Doktors der Philosophie
vorgelegt der
Philosophisch-Naturwissenschaftlichen Fakultät
der Universität Basel

von

Damien Nguyen
aus Val-de-Travers, NE

Basel, 2019

Originaldokument gespeichert auf dem Dokumentenserver der Universität Basel
edoc.unibas.ch



Diese Werk ist lizenziert unter eine Creative Commons
Namensnennung – Nicht kommerziell – Keine Bearbeitungen 4.0 International Lizenz

Genehmigt von der Philosophisch-Naturwissenschaftlichen Fakultät auf Antrag
von

Prof. Dr. Bernd Krusche
Fakultätsverantwortlicher

Prof. Dr. Oliver Bieri
Dissertationsleiter

Prof. Dr. Sebastian Kozerke
Korreferent

Basel, den 22-05-2018

Prof. Dr. Martin Spiess
Dekan

*I think physicists are the Peter Pans of the
human race. They never grow up,
and they keep their curiosity.*

— Isidor Isaac Rabi

To my family, friends and colleagues without whom all of this would not have been possible...

Acknowledgements

While this thesis has been written solely by me, all the work that lead to it can most definitely not be attributed only to my own efforts . All the projects and articles presented in later chapters, plus those works that have not been published yet and will remain secret for the time being, could not have been possible without the help and support from a lot of people and I would like to express here my most sincere gratitude and appreciation to each and every one of them for their help and support over the years.

First and foremost, I wish to thank

- ... Oliver Bieri for his thoughtful and kind supervision over the course of this adventure. His everyday support and patience as well as his trust and the freedom he gave me in my day-to-day work contributed not the least to the success of this thesis;
- ... Bernd Krusche for accepting to be me faculty representative and allowing me to do my thesis at the Faculty of Science of the University of Basel;
- ... Sebastian Kozerke for evaluating my thesis as my co-examiner.

I would also like to acknowledge and deeply thank my friends and colleagues from the Radiological Physics group in Basel for an extremely pleasant working atmosphere with countless hours spent drinking tea or coffee, discussing and chatting, as well as hanging out together outside of work

- ... Xenia Deligianni for her kind nature and never ending enthusiasm, not forgetting her godly ;
- ... Tanja Haas for her positive energy both in and outside of work and her expertise with MRI;
- ... Rahel Heule for introducing me to the subject and her guidance and overall help;

Acknowledgements

- ... Orso Pusterla for bringing the “ticinese” attitude and energy to work, for fun sport outings and for being measured too many times;
- ... Francesco Santini his friendship and hospitality, for innumerable insightful discussions about sequence programming as well as introducing me to scuba diving;
- ... Matthias Weigel for his kindness, patience and wisdom in answering my countless physical or linguistic questions.

Many thanks also to

- ... Tom Hilbert and Tobias Kober from the Siemens ACIT group in Lausanne for fruitful and enjoyable collaborations;
- ... Carl Ganter from the Clinic right of the Isar of the Technical University of Munich for his wisdom and expertise;
- ... Philipp Eheses and Klaus Scheffler from the Max-Planck Institute in Tübingen for letting me apply some of my methods at ultra high field strengths;
- ... Mark E. Ladd and Benjamin Knowles from the German Cancer Research Center (DKFZ) in Heidelberg for access to their high field system;
- ... Najat Salameh for taking the time to proofread this thesis despite a very busy schedule;
- ... the Swiss National Science Foundation (SNF) for the financial support.

And last but certainly not least, I would like to thank my parents, my brother and the rest of my family around the world for always being there when I needed it the most and without whom I would have not made it this far.

Basel, June 30, 2018

Damien Nguyen

Abstract

Over the years, magnetic resonance (MR) imaging has become a fundamental part of the diagnostic process in hospitals worldwide. While the underlying physics dates back more than 60 years with the development of nuclear magnetic resonance, methods that aim to accurately measure the multitude of parameters governing the signal formation are still a topic of active research and developments today. The main aim of this work is to explore the possibilities of developing quantification techniques based on a particular type of MR acquisitions: *balanced Steady-State Free Precession* (bSSFP). The first chapter briefly introduces the most relevant basic concepts of MR physics that will serve as foundation for the development of the methods presented thereafter. In the second chapter, a new method using multiple bSSFP scans is presented that aim to achieve motion insensitive three-dimensional quantification of relaxation times and thereby improve a recently published technique based on unbalanced gradient echo acquisitions. The method is then evaluated both in phantoms and *in vivo* studies at 3 T and the results discussed. These include an interesting bias of the method that might provide useful insights into the underlying tissue micro-structure. One the major challenges with bSSFP imaging is the presence of dark regions inside the images, which are due to inhomogeneities in the main magnetic field. In the third chapter, a new approach to address those issues is proposed, termed *trueCISS*, which combines fast imaging using sparse sampling with compressed sensing reconstructions and multi-parametric fitting, which ultimately allows the synthesis of artefact-free images. Evaluation of the new method is done at 3 T for the human brain. Finally, an extension of the trueCISS technique is presented in chapter four, where the process used to model the data to the signal equation is replaced by a novel algorithm based on configuration theory, which is essentially a representation of the signal formation processes in the Fourier domain. The improved trueCISS imaging method is then successfully evaluated with measurements at ultra high field strengths such as 7 T and 9.4 T which demonstrate the advantages of the new approach.

Zusammenfassung

Im Laufe der Jahre ist die Magnetresonanztomographie (MRT) zu einem fundamentalen Bestandteil des diagnostischen Prozesses in Krankenhäusern weltweit geworden. Während die zugrundeliegende Physik mehr als 60 Jahre mit der Entwicklung der Kernspinresonanz zurückliegt, sind Methoden, die darauf abzielen, die Vielzahl von Parametern, die die Signalbildung bestimmen, genau zu messen, immer noch ein Thema der aktiven Forschung und Entwicklung. Das Hauptziel dieser Arbeit ist es, die Möglichkeiten der Entwicklung von Quantifizierungstechniken basierend auf einer bestimmten Art von MR-Akquisitionen zu untersuchen: *balanced Steady-State Free Precession* (bSSFP). Im ersten Kapitel werden die wichtigsten Grundbegriffe der MR-Physik kurz vorgestellt, die als Grundlage für die Entwicklung der nachfolgend vorgestellten Methoden dienen.

Im zweiten Kapitel wird eine neue Methode vorgestellt, bei der mehrere bSSFP-Scans verwendet werden, um eine bewegungsunempfindliche dreidimensionale Quantifizierung von Relaxationszeiten zu erreichen und dadurch eine kürzlich veröffentlichte Technik basierend auf unbalancierten Gradientenecho-Aufnahmen zu verbessern. Die Methode wird dann sowohl in Phantomen als auch in *in vivo* Studien bei 3 T ausgewertet und die Ergebnisse diskutiert. Dazu gehört eine interessante systematische Fehler Bias der Methode, die nützliche Einblicke in die zugrunde liegende Mikrostruktur des Gewebes liefern könnte.

Eine der grössten Herausforderungen bei der bSSFP-Bildgebung ist das Vorhandensein dunkler Bereiche in den Bildern, die auf Inhomogenitäten im Hauptmagnetfeld zurückzuführen sind. Im dritten Kapitel wird ein neuer Ansatz zur Behandlung dieser Probleme vorgeschlagen, der als *trueCISS* bezeichnet wird. Er kombiniert schnelle Bildgebung und sparse Abtastung mit Compressed Sensing Rekonstruktion und multiparametrischer Anpassung, was letztlich die Synthese von artefaktfreien Bildern erlaubt. Die Auswertung der neuen Methode erfolgt bei 3 T für das menschliche Gehirn. Abschliessend wird in Kapitel vier eine Erweiterung der trueCISS-Methode vorgestellt, bei der der Prozess zur Modellierung der Daten zur Signalgleichung durch einen

Zusammenfassung

neuartigen, auf Konfigurationstheorie basierenden Algorithmus ersetzt wird, was im Wesentlichen eine Darstellung der Signalbildungsprozesse im Fourierraum darstellt. Die verbesserte trueCISS-Bildgebungsmethode wird dann erfolgreich mit Messungen bei extrem hohen Feldstärken wie 7 T und 9.4 T evaluiert, die die Vorteile des neuen Ansatzes demonstrieren.

Résumé

Au cours des années, l'imagerie par résonance magnétique (IRM) est devenue une partie essentielle du processus de diagnostique dans les hôpitaux du monde entier. Alors que la physique sous-jacente date de plus de 60 ans avec le développement de la résonance magnétique nucléaire, les méthodes dont le but est de mesurer précisément la multitude de paramètres à l'origine de la formation du signal restent un sujet actuel de développements et de recherche. Le but principal de ce travail est d'explorer les possibilités de développer des méthodes quantitatives basées sur un type d'acquisition IRM particulier : *balanced Steady-State Free Precession* (bSSFP). Le premier chapitre introduit brièvement les concepts de bases de la physique de la résonance magnétique nucléaire qui serviront de fondations aux développements qui suivent.

Dans le second chapitre, une nouvelle méthode utilisant plusieurs scans bSSFP est introduite qui a pour but d'obtenir une quantification des temps de relaxation résistant aux mouvements et de ce fait améliorer une technique récemment publiée basée sur un écho de gradient non balancé. La méthode est ensuite évaluée à la fois sur des sondes composées d'eau et *in vivo* à 3 T et les résultats discutés. Ceux-ci incluent un biais intéressant qui pourrait fournir des informations à propos de la micro-structure des tissus.

Un des défis principaux de l'imagerie bSSFP est la présence de régions sombres dans les images qui sont dues à des inhomogénéités dans le champ magnétique principal. Dans le troisième chapitre, une nouvelle approche pour résoudre ces problèmes est proposée, dénommée *trueCISS*, qui combine imagerie ultra rapide et échantillonnage peu abondant avec des reconstructions de type compressed sensing et des méthodes d'ajustements de paramètres pour permettre la synthèse d'images sans artefacts. L'évaluation de la nouvelle méthode est performée à 3 T pour le cerveau humain. Finalement, une extension de la méthode *trueCISS* est présentée dans le quatrième chapitre où la théorie de modélisation des données à l'équation du signal est remplacée par un nouvel algorithme basée sur la théorie des configurations, qui est essentiellement une représentation du processus de formation du signal dans l'espace de Fourier. La nouvelle méthode *trueCISS* est ensuite évaluée avec succès par des

Résumé

mesures à ultra hauts champs tel que 7 T et 9.4 T et démontre ainsi les avantages de la nouvelle approche.

Publications arising from this thesis

Journal papers

- Nguyen, Damien and Oliver Bieri (Sept. 8, 2016). “Motion-insensitive rapid configuration relaxometry”. In: *Magn. Res. Med.* Pp. 518–526. DOI: 10.1002/mrm.26384.
- Hilbert, Tom, Damien Nguyen, Jean-Philippe Thiran, Gunnar Krueger, Tobias Kober, and Oliver Bieri (July 24, 2017). “True constructive interference in the steady state (trueCISS)”. In: *Magn. Res. Med.* Pp. 1901–1910. DOI: 10.1002/mrm.26836.
- Nguyen, Damien, Tom Hilbert, Carl Ganter, Philipp Ehses, Klaus Scheffler, Benjamin R. Knowles, Mark E. Ladd, Tobias Kober, and Oliver Bieri (Apr. 2018). “Configuration-Based bSSFP Parameter Estimation and its Application to trueCISS Imaging at Ultra-High Fields”. In: *Magn. Res. Med.* (submitted).

Conference proceedings

- Hilbert, Tom, Damien Nguyen, Tobias Kober, Jean-Philippe Thiran, Krueger Gunnar, and Oliver Bieri (May 2015). “TrueCISS: Genuine BSSFP Signal Reconstruction from Undersampled Multiple-Acquisition SSFP Using Model-Based Iterative Non-Linear Inversion”. In: *Proceedings 23rd Scientific Meeting, International Society for Magnetic Resonance in Medicine*, p. 83.
- Nguyen, Damien and Oliver Bieri (May 2015). “MIRACLE: Motion-Insensitive Rapid Configuration reLaxomEtry”. In: *Proceedings 23rd Scientific Meeting, International Society for Magnetic Resonance in Medicine*, p. 6286.
- Hilbert, Tom, Damien Nguyen, Jean-Philippe Thiran, Gunnar Krueger, Oliver Bieri, and Tobias Kober (May 2016). “Fast 3D Acquisition for Quantitative Mapping and Synthetic Contrasts Using MIRACLE and trueCISS”. In: *Proceedings 24th Scientific Meeting, International Society for Magnetic Resonance in Medicine*, p. 2817.
- Hilbert, Tom, Damien Nguyen, Jean-Philippe Thiran, Gunnar Krueger, Tobias Kober, and Oliver Bieri (May 2016). “trueFLASH: Model-Based Iterative T1 Mapping using

-
- Variable-Flip-Angle Fast Low-Angle Shot”. In: *Proceedings 24th Scientific Meeting, International Society for Magnetic Resonance in Medicine*, p. 2816.
- Nguyen, Damien, Tom Hilbert, Philipp Ehses, Klaus Scheffler, Jean-Philippe Thiran, Oliver Bieri, and Tobias Kober (May 2016). “On-resonant balanced Steady-State Free Precession imaging at 9.4T”. In: *Proceedings 24th Scientific Meeting, International Society for Magnetic Resonance in Medicine*, p. 747.
- Nguyen, Damien, Tom Hilbert, Jean-Philippe Thiran, Tobias Kober, and Oliver Bieri (May 2016). “Metal implant imaging using highly undersampled phase-cycled 3D bSSFP”. In: *Proceedings 24th Scientific Meeting, International Society for Magnetic Resonance in Medicine*, p. 2292.
- Nguyen, Damien, Rahel Heule, Carl Ganter, and Oliver Bieri (May 2017). “On the decay of SSFP configurations”. In: *Proceedings 25th Scientific Meeting, International Society for Magnetic Resonance in Medicine*, p. 992.
- Jud, Christoph, Damien Nguyen, Robin Sandkühler, Alina Giger, Oliver Bieri, and Philippe C. Cattin (Sept. 2018). “Motion Aware MR Imaging via Spatial Core Correspondence”. In: *Medical Image Computing and Computer Assisted Intervention – MICCAI 2018*. Springer International Publishing, pp. 198–205.
- Nguyen, Damien, Tobias Kober, and Oliver Bieri (June 2018). “On the sensitivity of T_1 mapping methods to myelin”. In: *Proceedings 26th Scientific Meeting, International Society for Magnetic Resonance in Medicine*, p. 5486.
- Giger, Alina, Christoph Jud, Damien Nguyen, Krieger Miriam, Tony Lomax, Oliver Bieri, Rares Salomir, and Philippe C. Cattin (Sept. 2019). “Inter-fractional Respiratory Motion Modelling from Abdominal Ultrasound”. In: *Medical Image Computing and Computer Assisted Intervention – MICCAI 2019*. Springer International Publishing. (submitted).
- Jud, Christoph, Damien Nguyen, Alina Giger, Robin Sandkühler, Krieger Miriam, Tony Lomax, Rares Salomir, Oliver Bieri, and Philippe C. Cattin (Sept. 2019). “Accelerated Motion-Aware MR Imaging via Motion Prediction from K-Space Center”. In: *Medical Image Computing and Computer Assisted Intervention – MICCAI 2019*. Springer International Publishing. (submitted).

Miscellaneous

- Bieri, Oliver, Tom Hilbert, Tobias Kober, Gunnar Krueger, and Damien Nguyen (Sept. 17, 2016). “Apparatus and Method for Improving Balanced Steady-State Free Precision in Magnetic Resonance Imaging”. U.S. pat. req. US 2016/0334487 A1.

Contents

Acknowledgements	i
Abstract (English/Français/Deutsch)	iii
1 Introduction	3
1.1 Why does quantification matter ?	5
1.2 A relaxing world	6
1.2.1 Longitudinal relaxation	8
1.2.2 Transverse relaxation	9
1.3 Imaging an image	12
1.4 A truly magnetic evolution	13
1.4.1 Bloch equations	14
1.4.2 Balancing the magnetisation	14
1.4.3 Configuration theory	19
1.5 Reconstructing reality	21
1.5.1 Compressed sensing	21
1.5.2 Dictionary-based model fitting	23
1.6 Aim of this thesis	24
1.7 Outline	25
2 Motion-Insensitive Rapid Configuration Relaxometry	31
2.1 Introduction	33
2.2 Methods	33
2.3 Results	38
2.4 Discussion	40
2.5 Conclusion	43
3 True Constructive Interference in the Steady State (trueCISS)	49
3.1 Introduction	51

Contents

3.2	Methods	52
3.3	Results	57
3.4	Discussion	61
3.5	Conclusion	62
4	Configuration-Based bSSFP Parameter Estimation and its Application to trueCISS Imaging at Ultra-High Fields	65
4.1	Introduction	67
4.2	Theory	67
4.3	Methods	69
4.4	Results	69
4.5	Discussion	71
4.6	Conclusion	72
5	Conclusion	75
5.1	Summary	77
5.2	Future work	78
	Curriculum Vitae	81

1 Introduction

1.1. Why does quantification matter ?

Magnetic resonance imaging (MRI) is an imaging modality commonly used by clinicians around the world to diagnose, stage, monitor and assess treatment responses in a broad range of pathologies in patients. Unlike many other medical imaging modalities, such as positron emission tomography (PET), where the source of the signal is an administered radioactive isotope, or computed tomography (CT), where X-rays are recorded after being shined through a subject or object, the signal at the origin of MR images is emitted by the tissues themselves with help from high magnetic fields. The absence of ionising radiation makes MRI a very safe and attractive technique for both clinical and research settings. In comparison to CT or PET imaging, MRI is able to acquire more detailed images of soft tissues and organs, such as the brain, the heart or more recently the lungs [1–3]. It is one of the most versatile imaging technique offering both two-dimensional (2D) and three-dimensional (3D) volumetric images, which can be even extended with additional dimensions such as the time or spectral domains. Due to its versatility and the absence of ionising radiation, MRI has rapidly become one of the most important diagnostic tools of today's health-care diagnostic system.

1.1 Why does quantification matter ?

Most of the signal in conventional MRI originates from hydrogen (^1H) nuclei or protons found in various molecules inside the body, but mostly in water and fat. Signal intensity and image contrast in MRI are predominantly governed by a set of physical parameters which vary in the image depending on the underlying tissue composition. However, contrary to CT where intensity variations in the images directly reflect changes in a physical property of the object, namely the attenuation coefficient for X-rays which is expressed in an absolute scale (Hounsfield units), the link between MR images and the fundamental physical parameters governing them is not as straightforward. As a matter of fact, most imaging performed during MRI examinations today produces so-called *weighted* images, which do not represent a direct measurement of a particular physical, chemical or biological quantity. The simplest physical model of the MR signal already requires at least three parameters, namely the proton density and two relaxation times usually called T_1 and T_2 , which interact and affect each other in non-trivial ways during an MR experiment. Furthermore, the impossibility of reliably calibrating both the hardware and software of MR scanners also prevents quantitative and purely objective comparison between images acquired at different sites with different manufacturers or even across different scanner models. This is particularly problematic for studies that aim to investigate multiple different populations or even have reliable and stable measurements for longitudinal studies that follow patients and volunteers over many years, since software and hardware upgrades can subtly modify image contrast and may introduce unwanted biases in the outcome of those studies.

Chapter 1. Introduction

From the beginning, these challenges have inspired scientists to develop new classes of MRI methods aimed at providing *quantitative* rather than *qualitative* measurements. Instead of simply looking at an image with pixel values that do not hold any physical meaning, the basic idea is to isolate and measure one or more basic physical properties of an object, ideally without the confounding influences of any other quantities. This typically involves the acquisition of multiple MR images of the same anatomical region and further processing of the collected data using prior knowledge about the underlying physical, chemical or biological processes. For each of the investigated parameters, a map is generated which shows what values the physical quantity takes at each point of the object in space. Under the assumption that all the essential hypotheses made when modelling the MR signal are satisfied, and that no important effects have been left out of the analysis, the maps thus generated provide an absolute measurement of a given physical quantity. Such measurements can thus enable scientists and clinicians to perform inter-subject and cross-sites comparisons of MR data, as well as allowing the assessment of tissue alterations over long periods of time. However, despite their undeniable advantages, quantitative MRI techniques are still not generally used in the clinical setting. The main challenges to a wider adoption of these methods include a significant increase in scan time due to the numerous images that need to be acquired, and, in most cases, residual sensitivity to scanning parameters, system imperfections or inter-parameter dependencies that ultimately impair the relevance of the quantitative measurements. Developments in quantitative MRI are therefore aimed toward fast data acquisition and post-processing methods that can simultaneously precisely and accurately map multiple tissue parameters.

1.2 A relaxing world

The field of nuclear magnetic resonance (NMR) makes use of the physical processes in which nuclei interact with an external magnetic field. These interactions include the absorption and emission of energy in the form of electromagnetic radiations at specific frequencies which depend on the physical properties of the magnetic field and atomic nucleus. The most commonly studied nucleus in NMR is hydrogen (^1H) due to its abundance in living matter on Earth, mostly in water and adipose tissues. Many other nuclei can also be studied, such as the carbon-13 isotope (^{13}C), nitrogen (^{15}N), fluorine (^{19}F), sodium (^{23}Na) and phosphorus (^{31}P). The study of nuclei other than hydrogen using NMR and MRI can allow different types of observations, such as looking at the composition of cell membranes, studying of bioenergetical processes and pH in the case of phosphorous, or the probing of specific metabolic pathways in the case of hyperpolarised ^{13}C MRI.

A necessary condition for the application of NMR to a particular nucleus or isotope is the presence of a non-zero nuclear spin, which is a fundamental quantum mechanical property of all known matter, and gives rise to an associated magnetic moment. A

common analogy for the spins is to consider them as behaving like tiny magnets which is intuitive but can be misleading as quantum effects cannot be neglected. While a full understanding of NMR processes generally requires the use of the complete quantum mechanics formalism, a classical treatment of NMR using the concept of net magnetisation will be sufficient for the scope of this work.

In the presence of an external magnetic field, which shall henceforth be called B_0 , spin- $\frac{1}{2}$ particles such as protons have only two possible energy states often called *parallel* ($\uparrow\uparrow$) and *anti-parallel* ($\uparrow\downarrow$) to the magnetic field, in analogy to the spin magnetic moment. In general, however, the actual quantum state of the spins is neither of those basis states but rather a weighted combination of both. While intuitively most spins should naturally prefer the lowest energy state ($\uparrow\uparrow$), in reality, both states have almost equivalent prevalence among the spin population. This is due to the fact that the thermal energy is much larger than the energy separation between the two states, therefore equalising the mixing of the two states for most spins. The equilibrium that emerges can be described by the Boltzmann distribution which stipulate that the population imbalance between the states is given by

$$\frac{N(\uparrow\uparrow)}{N(\uparrow\downarrow)} = e^{\frac{-\Delta E}{kT}} \quad (1.1)$$

where ΔE is the energy difference between the two states, T is the temperature and k is the Boltzmann constant. As shown by the expression above and considering spins at or near room temperature, only a fraction of all spins are expected to prefer the lower energy state: about one in five millions at 1.5 T [4]. However, due to the very large number of spins in any meaningful volume of matter, this small amount still leads to the creation of a measurable magnetic moment parallel to B_0 . This is captured by the concept of the *net magnetisation* vector \mathbf{M} which is simply the sum of all spin magnetic moments in a given region of space. At equilibrium, \mathbf{M} is therefore aligned with B_0 , which defines the z -axis, and its amplitude, usually called M_0 , coincidentally represents its maximum value for a given magnetic field strength. When studying the evolution of the magnetisation, it is informative to split \mathbf{M} into two components: one parallel to B_0 , which we shall denote by M_z , and another in the perpendicular xy -plane which is complex-valued and shall be denoted M_{xy} . These are usually referred to as the *longitudinal* and *transverse* magnetisation respectively.

In order to measure a signal from spins using NMR, a perturbation must be introduced into the system. This is typically done by sending electromagnetic waves in the form of radio-frequency (RF) radiations with frequencies close to the Larmor frequency of the nuclei being studied. Typical values for this frequency for hydrogen in the clinical setting is around 63.87 MHz at 1.5 T and about 127.74 MHz at 3 T. The direction of the magnetic field created by the RF pulse is usually taken perpendicular to B_0 and has the effect of slowly rotating the net magnetisation \mathbf{M} away from its equilibrium

position along the z -axis. Immediately thereafter, two relaxation processes start taking effect and drive the magnetisation back to the equilibrium with two characteristic time constants denoted as the longitudinal (T_1) and transverse (T_2) relaxation times respectively. The analysis and a few of the figures that follow are inspired by those found in [4–7] and rely on the concept of the rotating frame of reference, sometimes known as the Larmor frame of reference. In this frame of reference, the precession of the magnetisation induced by B_0 vanishes, thus simplifying the analysis of the time evolution of the magnetisation. We thus consider a coordinate system (x, y, z) with unit vectors $(\hat{x}, \hat{y}, \hat{z})$ oriented such that $\mathbf{B}_0 = B_0\hat{z}$ and which rotates around \hat{z} at the Larmor frequency of the nucleus under consideration. If not otherwise specified, we also assume that RF pulses are instantaneous and perfectly tip all of the available magnetisation by a given angle. Further references used while writing this chapter include [8].

1.2.1 Longitudinal relaxation

After an RF excitation that rotates the magnetisation \mathbf{M} away from its equilibrium, the magnitude of the longitudinal component of the magnetisation (M_z) slowly recovers and grows back to its equilibrium value M_0 with a characteristic time constant T_1 , also called the spin-lattice relaxation time. The physical process behind this relaxation involves the dissipation of the energy from the excited spin population into their environment, which is linked to the size and motion of the molecule or nuclei they are a part of. For example, lipid molecules have movements with frequencies close to the Larmor frequency, which highly encourages energy exchanges with the environment and thus leads to very short T_1 relaxation times. On the contrary, free water molecules have much faster movements which discourage energy exchanges and thus give rise to long T_1 relaxation times.

Assuming that the spins start in the equilibrium state and an RF pulse is applied, M_z is described by the following equation of motion:

$$\frac{dM_z(t)}{dt} = \frac{M_0 - M_z(t)}{T_1} \quad (1.2)$$

where T_1 is introduced as a proportionality constant and corresponds to the characteristic time constant of the relaxation. The solution to this equation, assuming that the RF excitation occurred at $t = 0$, is then given by

$$M_z(t) = M_z(0) \exp\left(-\frac{t}{T_1}\right) + M_0 \left[1 - \exp\left(-\frac{t}{T_1}\right)\right] \quad (1.3)$$

An example of an exponential recovery curve described by Equation (1.3) is illustrated in Figure 1.1 where the effects of a 90° RF pulse on the longitudinal magnetisation are shown. Typical values for the longitudinal relaxation time for protons in the human

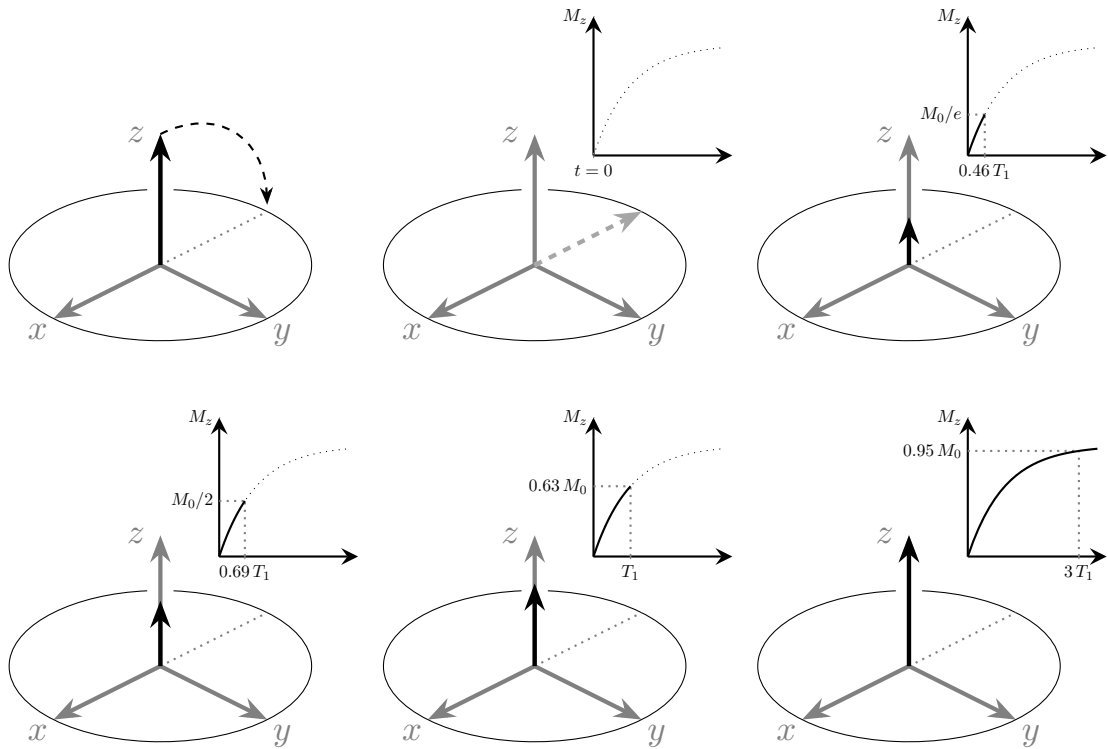


Figure 1.1 – Longitudinal relaxation. Immediately after being tipped by 90° into the transverse plane by an RF pulse, no longitudinal magnetisation remains (*i.e.* $M_z = 0$). M_z then slowly recovers and grows back until it reaches M_0 once again. At a time $t = 0.69 T_1$ after M_0 is tipped into the transverse plane, the longitudinal magnetisation M_z recovers to half its original value. At a time $t = T_1$, M_z has regrown to 63 % of its initial value and after waiting $3 T_1$, it has regained 95 % of its equilibrium value.

body ranges from hundreds to several thousands of milliseconds at common clinical field strengths (1.5 T, 3 T and up to 7 T). Approximately $\ln(2) T_1 = 0.69 T_1$ after the application of an 90° RF pulse that tips the equilibrium magnetisation completely into the transverse plane, M_z recovers half of its original value, and after $3 T_1$ and $5 T_1$, M_z recovers roughly 95 % and 99 % of its equilibrium value respectively as shown in Figure 1.1.

1.2.2 Transverse relaxation

At equilibrium, no transverse magnetisation can exist due to the spins natural tendency to align with B_0 . However, immediately after an RF excitation of any kind, part of the initial $M = M_0 \hat{z}$ gets transferred to the transverse plane, effectively creating transverse magnetisation. Contrary to the longitudinal magnetisation, the magnitude of M_{xy} then rapidly decays until no transverse magnetisation remains, a process which occurs with a characteristic time constant T_2 .

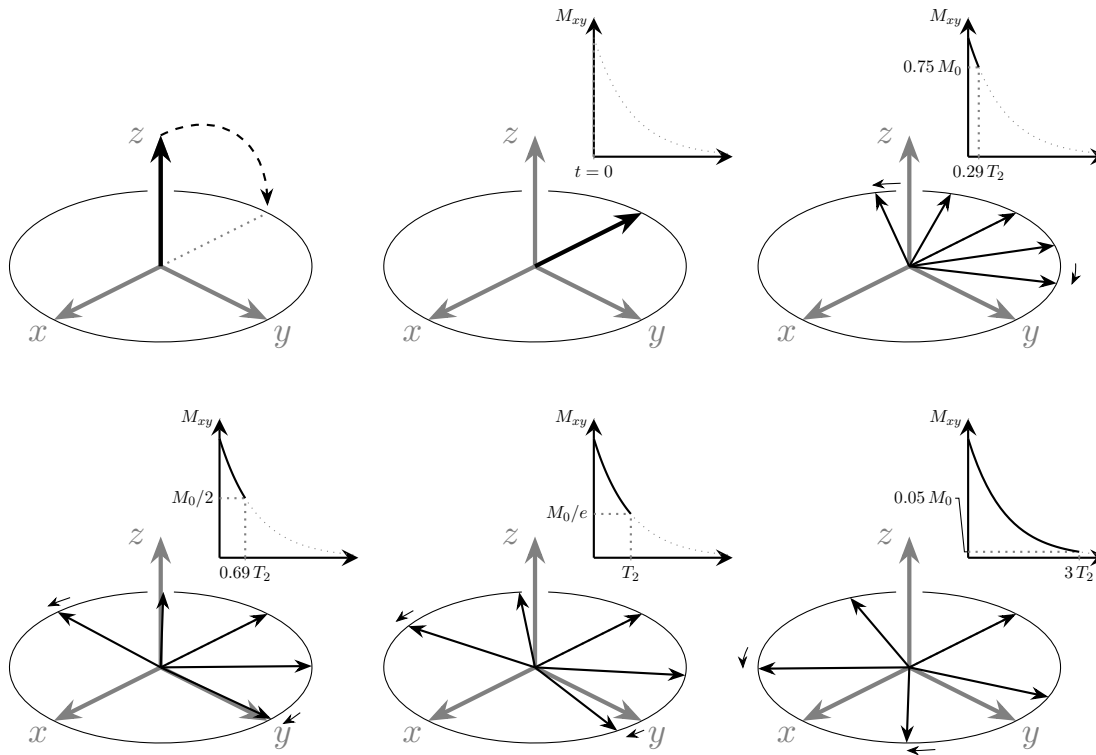


Figure 1.2 – Transverse relaxation. The phase coherence of a collection of spins in the transverse plane, immediately after the application of a 90° RF pulse, rapidly disappears over time, resulting in the loss of transverse magnetisation. At a time $t = 0.69 T_2$ after M_0 is tipped into the transverse plane, the transverse magnetisation M_{xy} is reduced by a factor of 2. At a time $t = T_2$ and $t = 3T_2$, M_{xy} has dropped to 37% and 5% of its initial value respectively.

Any processes that contribute to longitudinal relaxation also affect the decay of the transverse magnetisation. As excited spins exchange energy with the environment and return to the equilibrium state, their contribution to M_{xy} vanishes and therefore M_{xy} decreases in magnitude. These are sometimes referred to as T_1 in T_2 effects in the literature. In addition, interactions between individual spins also play a role in the decay of the transverse magnetisation, which is therefore faster than the recovery of the longitudinal magnetisation, effectively imposing $T_2 \leq T_1$. Considering a group of spins close to one another and immediately after the application of an RF excitation, the frequency at which they precess around B_0 will be identical for all of them and exactly equal to the Larmor frequency. The state where all spin precess synchronously is called *phase coherence* and would last eternally in the case of non-interacting spins. However, the local magnetic field experienced by the spins is a combination of the external field B_0 and the fields generated by their neighbours' spin magnetic moments. As constituents of atoms within molecules, spins are moving rapidly and randomly, which effectively makes the local magnetic field fluctuate over time and therefore induce

differences in the precession speed of the individual spins. This leads the individual spins to “fan out” over time as shown in Figure 1.2, a process also referred to as *dephasing*. The transverse magnetisation being the vector sum of all the individual transverse components, its magnitude then naturally decays as phase coherence is lost. A second type of processes that also contributes to the lost of phase coherence is one where two individual spins swap their spin states, often known as spin *flip-flop*. Since the last two described processes are random and time-dependent by nature, T_2 relaxation due to either spin-lattice or spin-spin interactions is therefore irreversible.

In the absence of any B_0 inhomogeneities, the equation of motion for the transverse magnetisation is given by

$$\frac{dM_{xy}(t)}{dt} = -\frac{M_{xy}(t)}{T_2} \quad (1.4)$$

where T_2 is a proportionality constant and corresponds to the characteristic time constant of the relaxation. The solution to this equation, assuming that the RF excitation occurred at $t = 0$, is then given by

$$M_{xy}(t) = M_{xy}(0) \exp\left(-\frac{t}{T_2}\right) \quad (1.5)$$

Typical values for the transverse relaxation time T_2 for protons in the human body ranges from a few milliseconds to hundreds of milliseconds at the most common field strengths (1.5 T and 3 T).

In addition to spin-spin interactions, phase coherence can be destroyed when encountering local variations of the main magnetic field B_0 , which can be caused either by the actual hardware or even by the object or person being imaged. This typically happens at interfaces between two mediums with different magnetic susceptibilities, such as air and water for example. The dephasing introduced by this kind of process is usually faster than those due to spin-spin interactions at high field strengths and occurs with a characteristic time constant T_2' . The overall transverse relaxation time which includes the relaxation from both kind of processes is called T_2^* and, under common assumptions about the decay line shape¹, is given by:

$$\frac{1}{T_2^*} = \frac{1}{T_2} + \frac{1}{T_2'} \quad (1.6)$$

Since the B_0 inhomogeneities at the source of the T_2' decay do not change with time, the dephasing induced by T_2' can be eliminated by the application of an appropriately designed RF pulse which has the effect of reversing the time evolution of the spins to some extent, eventually leading to a rephasing of the spin packets.

¹Namely that the line shape is Lorentzian

1.3 Imaging an image

The process of generating an image in MRI is intimately linked to the local strength of the magnetic field, which in turns influences the frequency at which spins are precessing. Neglecting any field inhomogeneities and spin interactions, all the spins within a volume of matter inside an MRI scanner precess at the same rate. In order to generate an image, however, the frequency of precession needs to be momentarily made dependent on the position. This is normally achieved using so-called *gradient* coils that are also oriented along the z -axis and introduce a linear variations of B_0 in space. Such kinds of magnetic field can be fully characterised using an amplitude $\mathbf{G} = (G_x, G_y, G_z)$, which might vary over time, leading to the following equation:

$$B_0(\mathbf{r}) = B_0 + \mathbf{G} \cdot \mathbf{r} = B_0 + (G_x x + G_y y + G_z z) \quad (1.7)$$

Gradients are usually referred to based on their function or direction, such as the *readout* or *frequency encoding* gradient, or the *phase* and *slice encoding* gradients. A more detailed description of the function of each gradient direction, which also explains the reason behind their names, can be found in [5, 9, 10]. The readout gradient is conventionally taken along the x -axis while phase and slice encoding gradients usually lie along the y and z axes respectively. Gradient fields are typically turned on and off many times during the acquisition of an image, which creates the distinct clanking and buzzing noises people often hear during MRI scans.

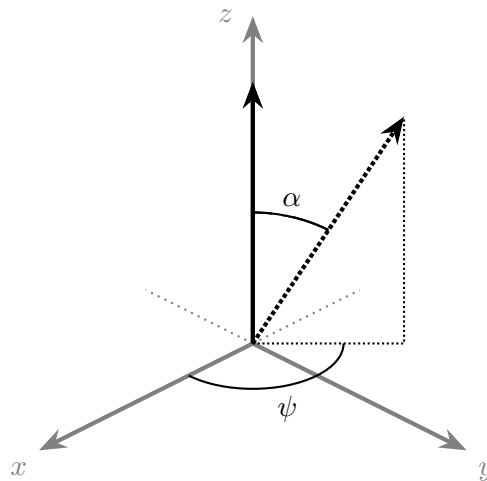


Figure 1.3 – Depiction of a magnetisation rotated by an RF pulse with flip angle α and phase ψ (assuming that reference for the 0° phase is taken along the x -axis).

An MRI sequence is a collection of RF and gradients pulses of different shapes and forms which leads to the acquisition of an image. In some cases, the post-processing steps required to obtain the final images are also included in this definition. Generally, MRI sequences depend on a variety of parameters that influence their contrast,

duration and ultimately their image quality properties. Each sequence typically has a number of these parameters, which can be either specific to that particular sequence or be shared among a family of similar sequences. There are, however, a few parameters that can be found in virtually all MRI sequences and are therefore important to mention. For the vast majority of sequences, the MRI scanner does not acquire a whole image all at once, but rather step by step². A sequence therefore consists of multiple repetitions of a basic block that contains a pattern of RF excitation pulses and gradient waveforms. While the pattern generally does not change from repetition to repetition, minor changes do occur in order to acquire different parts of the data required to reconstruct an image. The duration of these building blocks is called the *repetition time* (TR) and can be as low as a few milliseconds or as high as a few seconds depending on the applications and the sequence. It naturally has a big impact on the overall duration of a sequence, but most importantly also influences image contrast. Within a block, the time between the RF pulse and the acquisition of the signal it generated is called the *echo time* (TE), as the signal measured in an MR experiment is similar to the echo of an event that occurred previously. Another important parameter is the *flip angle*, often denoted as α , which is the angle by which the net magnetisation is rotated by the RF pulse. Another parameter relevant to RF pulses is their phase, denoted ψ in the following, that controls the direction in which the magnetisation is rotated by an RF excitation (see Figure 1.3). During an MRI sequence, the phase of an RF pulse may change from one pulse to the next. In most cases, the change in RF phase follows a specific pattern and the amount by which the RF phase is incremented between the application of two consecutive RF pulses is called the RF phase increment and will be denoted by φ in the rest of this thesis.

1.4 A truly magnetic evolution

In the classical description of NMR introduced in the previous chapter, the net magnetisation is actually the source of the signal detected in MR experiments. Properly characterising the evolution of the net magnetisation over time is essential in order to control the measurements that are performed on the scanners and correctly recognise potential artefacts in the images as such and not misinterpreted them as abnormalities that could indicate the presence of a pathology or disease. Comprehension of the underlying physical mechanisms is of particular importance when developing new MRI quantification methods in order account for the phenomena that will be the most relevant and thereby ensure good accuracy and precision for the estimates that ensue.

The following section introduces one of the most well-known framework used to study the evolution of the magnetisation known as the *Bloch equations*. Those equations will

²Actually, an MRI scanner never directly acquires an image but rather samples points in k -space which then need to be Fourier transformed back into real space in order to obtain an actual image.

Chapter 1. Introduction

then be used to describe a particular type of sequence, which lies at the heart of this thesis. An alternative description for the magnetisation will then be introduced by making use of the formalism of configuration theory [11–15], which is a more abstract and indirect representation of the magnetisation in the Fourier domain as opposed to real space. A more thorough and detailed description of the theory can be found in [5]. A closely related and more pictorial representation of the Fourier states can be found in the Extended Phase Graph (EPG) formalism [16].

1.4.1 Bloch equations

The equations of motion of a magnetic moment $\boldsymbol{\mu}$ due to an external magnetic field \mathbf{B} is given by

$$\frac{d\boldsymbol{\mu}}{dt} = \gamma(\boldsymbol{\mu} \times \mathbf{B}) \quad (1.8)$$

where γ is a constant called the gyromagnetic ratio. This expression can be immediately generalised for the net magnetisation \mathbf{M}

$$\frac{d\mathbf{M}}{dt} = \gamma(\mathbf{M} \times \mathbf{B}) \quad (1.9)$$

since it can also be understood as the local magnetic moment per unit of volume: $\mathbf{M} \triangleq \frac{1}{V} \sum_i \boldsymbol{\mu}_i$ where i indexes all the spins contained in volume V . Equation (1.9) is generally referred to as the *Bloch equations*, which do not yet account for the relaxation processes presented in the previous section. Apart from the main external magnetic field B_0 and the gradient fields characterised by their amplitude in each direction $\mathbf{G} = (G_x, G_y, G_z)$, the magnetic component of the RF field is commonly denoted by B_1 . Recalling that B_0 and the gradient fields ($\mathbf{G} \cdot \mathbf{r}$) lie along the z -axis and \mathbf{r} is a position vector, the matrix form of the general Bloch equations in the rotating frame of reference, taking into account both T_1 and T_2 relaxation processes is expressed by

$$\frac{d\mathbf{M}}{dt} = \begin{bmatrix} -1/T_2 & \gamma(\mathbf{G} \cdot \mathbf{r}) & -\gamma B_{1y} \\ -\gamma(\mathbf{G} \cdot \mathbf{r}) & -1/T_2 & \gamma B_{1x} \\ \gamma B_{1y} & -\gamma B_{1x} & -1/T_1 \end{bmatrix} \begin{bmatrix} M_x \\ M_y \\ M_z \end{bmatrix} + \begin{bmatrix} 0 \\ 0 \\ M_0/T_1 \end{bmatrix} \quad (1.10)$$

where the z -component of the RF field B_1 was neglected since it is much smaller than B_0 in practice ($B_1 \approx 10^{-5} B_0$ [5]). Equation (1.10) lays the basic foundation onto which most MRI theories are based upon for the design of both RF pulses and imaging sequences.

1.4.2 Balancing the magnetisation

The balanced Steady-State Free Precession (bSSFP) sequence was first published by Carr [17] in 1958 for NMR spectroscopy. It belongs to the family of *gradient echo*

sequences where the signal is generated by applying a single RF excitation pulse followed by the applications of multiple gradients with different polarities that ultimately lead to the rephasing of the spin packets and the generation of an MR signal. The classical implementation of the bSSFP sequence for imaging in 3D is shown in Figure 1.4. While phase and slice encoding gradients vary between each application of an RF pulse as shown by the dashed lines, the readout gradient and RF pulse remain unchanged. The main feature of the bSSFP sequence is that the sum of positive and negative gradient lobes (grey shaded areas in Figure 1.4) on each gradient axis, also referred to as the gradients' zeroth moment, is equal to zero. Such gradients are called what is commonly called *balanced* thus explaining part of the name of the sequence.

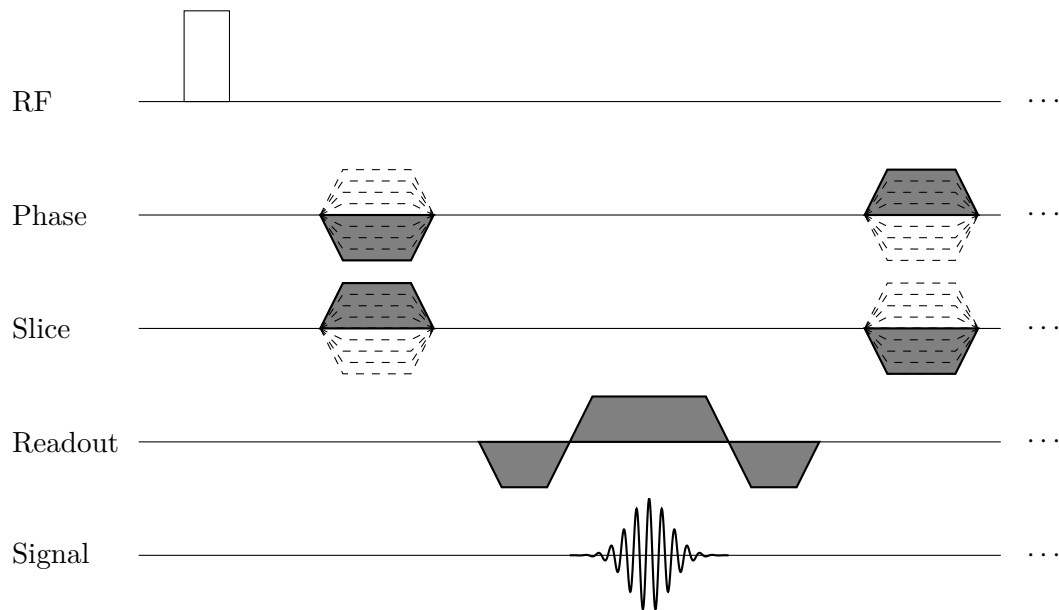


Figure 1.4 – Example of a 3D MRI sequence diagram showing all gradient and RF pulses applied during a single repetition (TR). Here represented is a classical implementation of a bSSFP sequence. The gradients lobes (shaded grey areas) in the two phase encoding directions (Phase & Slice) change from one application of an RF pulse to the next (dashed lines). All positive and negative gradients lobes along each gradient axis cancel out so that the average gradient moment in one repetition is effectively null giving this sequence excellent signal-to-noise and motion insensitivity properties.

The fact that the net dephasing due to the gradients at the end of the repetition time is effectively null implies that any effects that might be induced by the gradient fields vanish so that the magnetisation at the end of the repetition time essentially behaves as if no gradients had been applied in the interval since the application of the RF pulse. More rigorously, only the zeroth moment of the gradients is compensated in the example in Figure 1.4. It is however possible to cancel out higher gradient moments at the cost of longer repetition times [18]. Nevertheless, the nulling of the gradients' zeroth moment makes the bSSFP steady-state magnetisation totally coherent, which renders it very robust against motion during the acquisition, but also provides the one

of the highest signal-to-noise ratio (SNR) per unit of time of all known sequences [19] due to coherent superposition of many echoes as will be discussed in the next section. However, this also has the undesired effect of making magnetic field inhomogeneities a predominant factor in the signal formation as they are unaffected by gradient reversal. These typically end up manifesting themselves in bSSFP images as dark regions with little to no signal, which are commonly called *banding artefacts* due to their shapes as is exemplified in Figure 1.5. Typically, methods to eliminate these artefacts were mostly based on simple arithmetic combination of images in which the artefact are spatially shifted. However, more recent methods, such as the ones presented in the latter chapters of this work, focus on modelling of the signal in order to extract important physical quantities like the relaxation times. Artefact-free images can then be synthetically generated using the estimated parameters maps in combination with a signal model.

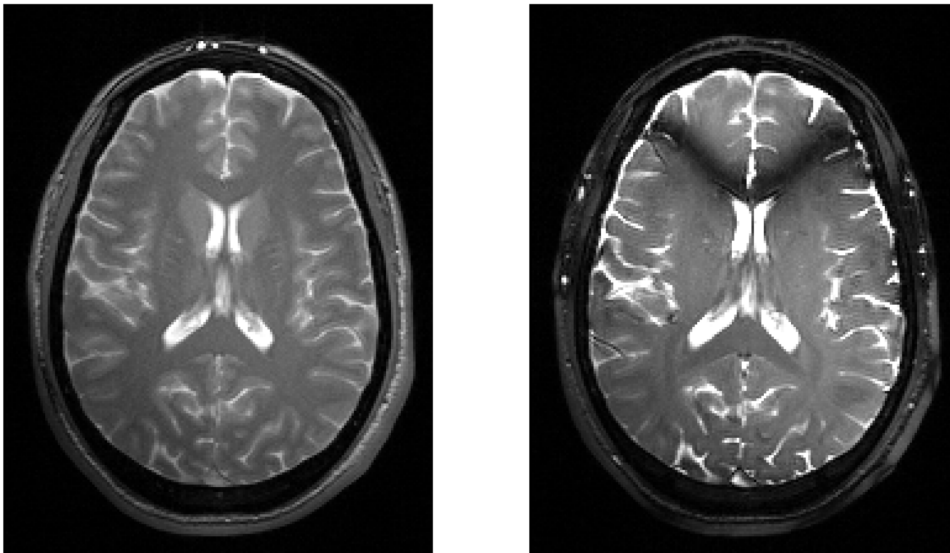


Figure 1.5 – Examples of bSSFP images of the human brain of a healthy volunteer ($\alpha = 15^\circ$, TR/TE 5.76/2.88 ms). While the image on the left looks mostly devoid of artefacts, the one on the right clearly show the effect of banding artefacts. The only parameter that was changed from one acquisition to the other is the value of the RF phase increment φ , which in this case may be chosen so as to avoid the presence of artefacts in this particular slice.

BSSFP sequences are typically performed using very short repetition times and using constant RF phase increments as opposed to other gradient echo sequences. Under these conditions, a coherent build up of magnetisation towards a steady-state value is expected, meaning that after a number of repetitions, a point is reached where the total net magnetisation after one RF pulse is identical to the one after the next RF pulse. This is illustrated in Figure 1.6 with an example using a train of 45° RF pulses and assuming that the magnetisation state before an RF pulse is given by $|M_z| = |M_{xy}|$. By using a suitable repetition time, this situation leads to the creation

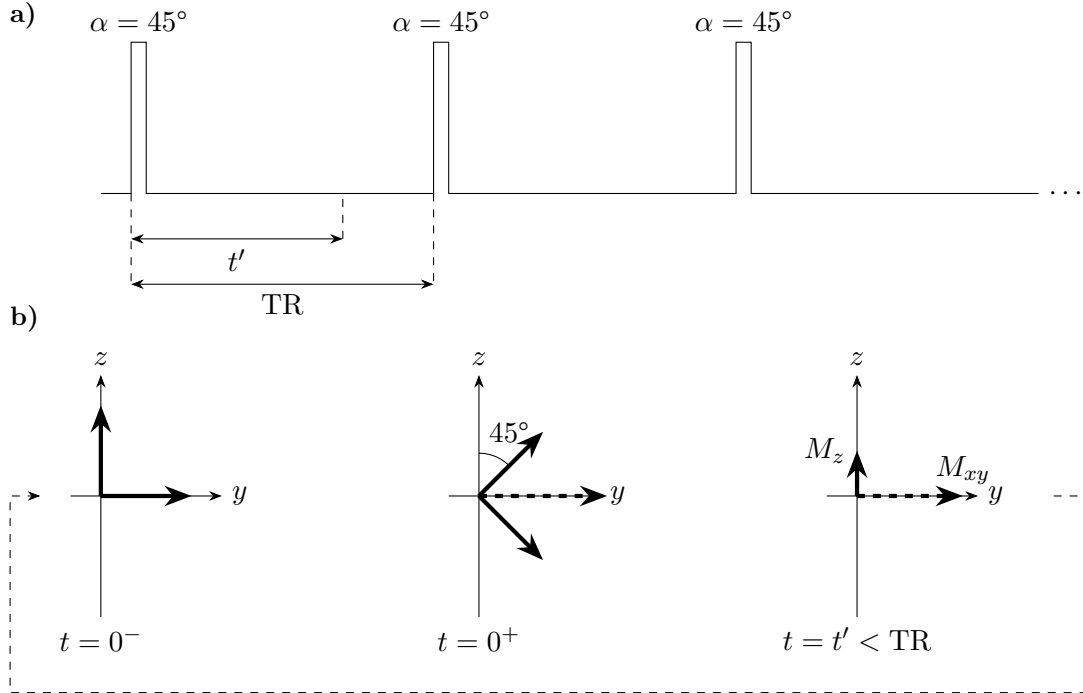


Figure 1.6 – Demonstration of a bSSFP steady-state magnetisation (neglecting field inhomogeneities). (a) Train of RF pulses with short repetition time leading to a steady-state (b) Evolution of the magnetisation at specific time points. Just prior to an RF pulse ($t = 0^-$), longitudinal and transverse magnetisations have equal magnitude. Immediately after the RF pulse ($t = 0^+$), effectively all the magnetisation is in the transverse plane (dashed arrow). At time $t = t' < TR$, T_1 recovery and T_2 decay normally occur for M_z and M_{xy} respectively. If the repetition time is chosen adequately, at $t = TR$ the magnetisation state will be identical to the one just prior to the previous RF pulse, leading to a steady-state.

of a steady-state. An exact expression for the steady-state magnetisation generally depends on the repetition time, flip angle and relaxation times, as well as on the local field inhomogeneities as discussed previously. Under the assumptions that $TR \ll T_2 \leq T_1$, ignoring any finite effects from RF pulses, neglecting any diffusive processes and considering an equidistant train of RF pulses with constant flip angles α and constant RF phase increment, the transverse magnetisation immediately after the RF pulse (denoted by the '+' superscript) takes the form [20]

$$M_{xy}^+(\vartheta) = -\frac{i}{D} (1 - E_1) \sin \alpha \left(1 + E_2 e^{-i\vartheta} \right) \quad (1.11)$$

where ϑ is the phase offset due to field inhomogeneities, often also called off-resonance,

and with the additional definitions

$$\begin{aligned}
 D &\triangleq a(1 + E_2 \cos \vartheta) + b(E_2 + \cos \vartheta)E_2 \\
 a &\triangleq 1 - E_1 \cos \alpha \\
 b &\triangleq \cos \alpha - E_1 \\
 E_i &\triangleq \exp(-\text{TR}/T_i)
 \end{aligned}$$

An example of the dependence of Eq. (1.11) on ϑ is shown in Figure 1.7. This graph is sometimes called the *frequency response* of the bSSFP sequence as ϑ can be linked to the precession frequency of the spins. The cause for banding artefacts can clearly be seen in regions close to $\vartheta = 0^\circ$ and $\vartheta = 360^\circ$ where significant signal reduction occurs regardless of flip angle and relaxation times ratio. Also note that since ϑ only appears in trigonometric or imaginary exponential terms, the expression for M_{xy} from Eq. (1.11) is periodic in ϑ .

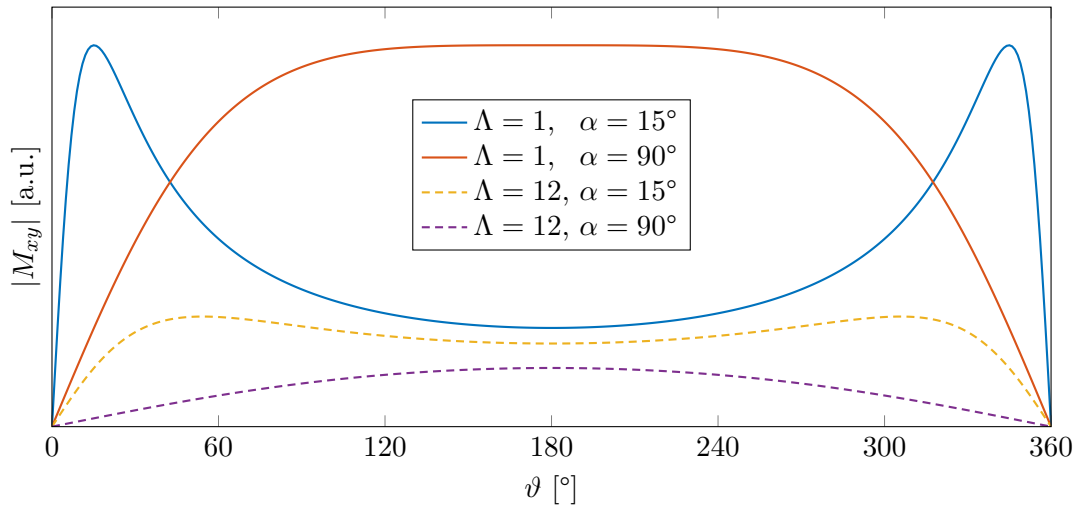


Figure 1.7 – Dependence of the magnitude of the bSSFP signal equation (Eq. (1.11)) on the phase linked to off-resonances ϑ for a few combinations of α , T_1 and T_2 .

Contrary to other known sequences such as the single echo spin echo or spoiled gradient echo sequences, the signal generated by a bSSFP acquisition depends on a complex combination of relaxation times, phase accruals from off-resonances and other sequence parameters. Therefore, estimating any one of the basic physical quantities entering in the equation has to be performed carefully in order to prevent the introduction of undesired biases.

1.4.3 Configuration theory

The description and analysis of the signal generated by an MRI sequence so far has been performed using a representation of the magnetisation vectors in real space. While this description is rather straightforward and intuitive, it is not the only possible representation of the signal in an MR experiment. A second description will now be introduced based on the concept of configurations modes that live in Fourier space. This description originated from the desire to get better understanding of the echo formation processes in multiple echo spin-echo sequences with arbitrary flip angles using the extended phase graph formalism [16]. This lead to a new formalism where the echo amplitudes (*i.e.* strength of measured signal) could be calculated in a much more straightforward and efficient way than simply relying on the Bloch equations. The theory also provides a framework that allows a much deeper and simple understanding of the contrast behaviour of different gradient echo sequences. While it is generally valid for sequences with equidistant RF pulses and constant zeroth order gradient moment, only the special case of bSSFP will be considered here.

As seen previously in Figure 1.7, the steady-state magnetisation of the bSSFP sequence is periodic in the phase linked to off-resonance ϑ . It can therefore be represented as a Fourier series:

$$M_{xy}^+ = \sum_{-\infty}^{\infty} e^{in(\vartheta-\pi)} M^{(n)} \quad (1.12)$$

where $M^{(n)}$ is the n -th configuration order. Surprisingly, while most sequences are designed to measure the signal from one up to a few of these configurations, the bSSFP sequence has the particularity that the signal measured is composed of a sum over all configuration orders. This is mainly due to the balanced nature of the gradients and the constant RF phase increment that ensure that all configurations always add up coherently to produce the MR signal that is measured during an experiment.

Even more remarkable is that it is actually possible to estimate the individual configurations $M^{(n)}$ from a sampling of the bSSFP frequency response profile. In a seminal work, Zur *et al.* [21] have shown how the N -point discrete Fourier transform of the frequency response characterised by m_j as the j -th sampling point

$$z^{(n)} \triangleq \frac{1}{N} \sum_{j=0}^{N-1} \left(m_j e^{-i\vartheta_j t / \text{TR}} \right) e^{-i2\pi n j / N} \quad (1.13)$$

relates to the configuration orders $M^{(n)}$. For large enough N , this approximately yields

$$z^{(n)} \approx e^{-\frac{t}{T_2}} e^{in\vartheta} M^{(n)} + n^{(n)} \quad (1.14)$$

where $n^{(n)}$ represent the noise. While in practice the phase shifts ϑ_j can be obtained by successively modifying the strength of the main magnetic field while acquiring a set of bSSFP images, a more practical and common way of achieving the same result is by acquiring multiple bSSFP images, sometimes called *phase-cycles* in this context, with different values of the RF phase increment. This is typically done with a set of equidistant RF phase increment φ_j defined by $\varphi_j \triangleq -\frac{2\pi}{N}j \wedge j = 0, 1, \dots, N - 1$.

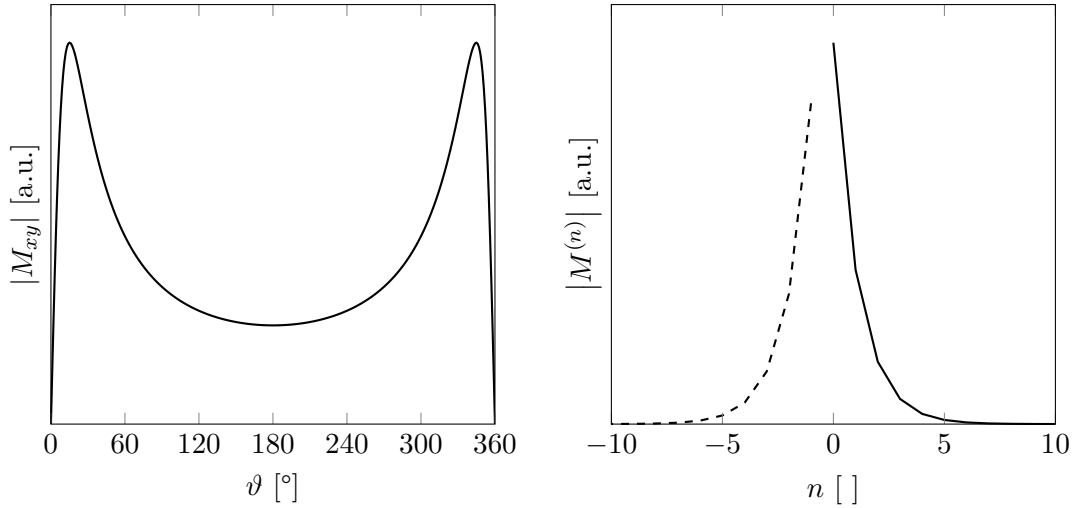


Figure 1.8 – Example of bSSFP frequency response profile (FRP) with its corresponding amplitudes of positive (—) and negative (---) configurations as estimated using a Fourier transform of the FRP (signal parameters: $\alpha = 15^\circ$, $\text{TR}/\text{TE}/T_1/T_2 = 5/2.5/880/70$ ms). Continuous lines connecting positive and negative modes are shown here for improved visualisation.

Figure 1.8 shows an example of bSSFP frequency response profile as well as the resulting positive and negative configurations as estimated using the Fourier transform method. As expected from the theory, higher order configurations (*i.e.* $N \gg 0$) exhibit very low amplitudes and limited contributions to the overall bSSFP signal. In order for the estimation to be accurate, the number of phase-cycles N , must be large enough so that no aliasing artefacts occur in the Fourier transform³.

An important assumption made during that analysis is that the signal used to estimate the configurations can be adequately described by Eq. (1.11). The violation of this assumption would introduce a bias in the configuration estimates, which typically occurs in the human brain where the tissue micro-structure leads to an asymmetric bSSFP frequency response profile [22, 23].

³In general for human tissues, 12 to 16 phase-cycles should be enough to properly estimate configurations up to the 4th order [21].

1.5 Reconstructing reality

Recent advancements in computing power and the development of advanced image reconstruction techniques have enabled new types of MR acquisitions such as MR compressed sensing [24], where only a fraction of the data required for the reconstruction of an image is measured, or MR fingerprinting [25], which is a complete paradigm shift in terms on how to use RF pulses and gradient fields, not focusing on directly acquiring image-related data but instead searching for data patterns in experimental data and comparing those to dictionaries of simulated data. In the following, we will shortly introduce a few techniques on which the latter works of this thesis are partly based on.

1.5.1 Compressed sensing

Historically, the acquisition of an MR image involved the acquisition of a large number of data points and the MR image was then reconstructed by simply applying the inverse Fourier transform to the acquired data. With the advent of parallel imaging techniques, such as Generalised Autocalibrating Partially Parallel Acquisitions (GRAPPA) [26] and SENSitivity Encoding (SENSE) [27], more and more data points could be left out of MRI acquisitions, which leads to shorter acquisition times, while still being able to produce nearly artefact-free images. More recently, a technique that involves skipping a larger portion of the data points has been introduced under the name *compressed sensing* [24]. The main observation leading to its development is that any MR image contains a lot of redundant pieces of information, which is to say that MR images can be *compressed* without losing too much information. Taking the reverse of this argument, given compressed data, a reconstruction of the full data should therefore be possible without compromising too much on the quality of the result. Therefore, reconstruction of a full MR image based on just a few data points is possible, provided that a way to extract the redundant information exists.

In more technical words, in order to apply a compressed sensing reconstruction, an object or subject being imaged must have a *sparse representation* in a mathematical domain to which data can be transformed to and from. An image is considered as sparse in any given space when its information content is contained within only a few pixels, while the contributions of the remaining majority of pixels can be essentially neglected since close to or equal to zero. When considering an image such as the one shown in Figure 1.9a which has many regions of constant signal intensity, a suitable sparsifying transformation can be a simple finite difference operation as shown in Figure 1.9b. In practice, commonly used transformations include the discrete cosine and discrete wavelet transforms as already widely used for JPEG compression. An additional requirement is that data points are acquired in a random or pseudo-random manner so that the artefacts thus generated are spread as much as possible over the

whole image.

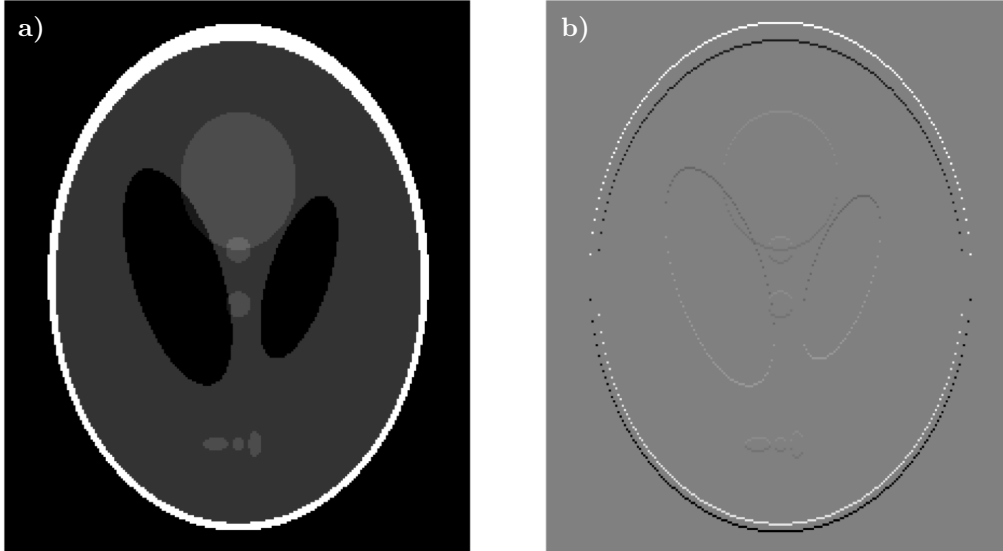


Figure 1.9 – Example of the sparse representation of an image. (a) original image (b) same data after application of a finite difference transformation (pixels with zero values are grey). Compare the 27 468 pixels with non-zero values in (a) to the only 531 pixels with non-zero values in (b)

Provided that the two aforementioned requirements are satisfied, reconstructing an image from sparsely acquired data amounts to solving the following minimisation problem

$$\min_X \underbrace{\|AX - Y\|_2^2}_{\text{Data fidelity}} + \lambda \underbrace{\|\Phi(X)\|_1}_{\text{Sparsity}} \quad (1.15)$$

where X is the unknown fully sampled image, Y is the sparsely acquired data, A the system matrix which describes the data acquisition process, $\Phi(X)$ is the sparsifying transform and λ a regularisation parameter. The role of the *data fidelity* term is to ensure that the reconstructed image data and measured data points remain consistent with one another, while the *sparsity term* enforces the data sparsity constraint.

Consequently, Equation (1.15) results in a minimisation algorithm that attempts to satisfy both data consistency and sparsity criteria, and therefore produces an image very similar to one where all the data points would have been acquired, but that required only a fraction of the acquisition time. In practice, however, perfect image reconstructions using compressed sensing are never attainable, due to the presence of noise or even artefact in the sparsely acquired data.

1.5.2 Dictionary-based model fitting

While dictionary fitting algorithms have been mostly used for MR fingerprinting techniques in recent years, they can also be used for fitting physical models to experimental data. Particularly in cases where the model function is not differentiable in a given variable or in situations where other conventional optimisation techniques fail due to badly conditioned optimisation problems, this kind of fitting approach may provide a useful alternative.

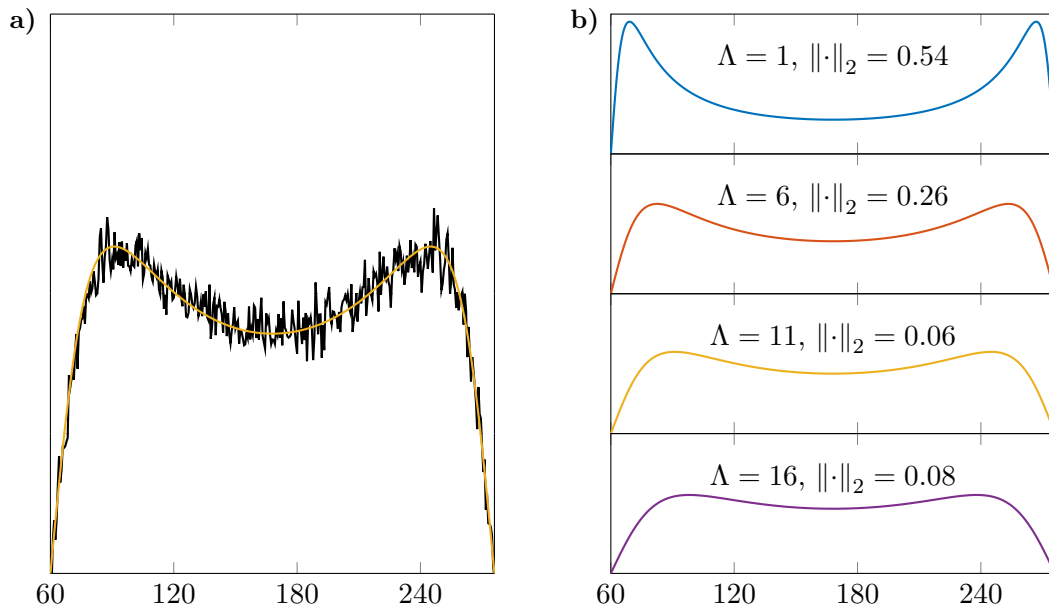


Figure 1.10 – Example of dictionary fitting. **(a)** An experimental data set; in this case a bSSFP frequency response generated using Eq. (1.16) with $\alpha = 15^\circ$, $\Lambda = 12$ and 25 dB of added Gaussian white noise **(b)** dictionary of signals simulated using the same equation with various values for Λ (1, 6, 11 and 16). After comparison of the data using the l_2 -norm in **(a)** with all the entries in **(b)**, the closest match is found with the $\Lambda = 11$ entry of the dictionary.

The basic premise of fitting a model to experimental data using a dictionary fitting technique involves generating a *dictionary* of realisations of the model using a discrete set of parameter values. Prior to comparison, both the experimental data and each dictionary entry are independently normalised. The experimental data is then compared to each of those realisations using a metric, such as the l_2 -norm of the difference between simulated and experimental data: $\|X_{\text{exp}} - X_{\text{dict}}\|_2$. The set of model parameters corresponding to the dictionary entry that most closely matches the experimental data (*i.e.* the one with the lowest value of the metric) is then taken as the solution to the minimisation problem. An example of fitting for a simplified approximation of the amplitude of the bSSFP frequency response given by the

expression below is shown in Figure 1.10

$$M_{xy}(\Lambda; \alpha, \vartheta) \approx \frac{2 \cos\left(\frac{\vartheta}{2}\right) \sin \alpha}{1 + \cos \alpha + 2 \cos \vartheta + [4\Lambda - 2 \cos \vartheta] \sin^2\left(\frac{\alpha}{2}\right)} \quad (1.16)$$

where ϑ is the off-resonance phase, α the flip angle and $\Lambda \triangleq T_1/T_2$. Assuming that the flip angle and the off-resonance phase are known, an attempt is made to estimate the value of Λ in the experimental data shown in Figure 1.10a (parameters: $\alpha = 15^\circ$, $\Lambda = 12$). In this example, fitting is performed using a dictionary of simulated bSSFP frequency responses (cf. Eq. (1.16)) depicted in Figure 1.10b with various values for Λ (1, 6, 11 and 16). The result of the fitting procedure is the value of Λ for which the entry within the dictionary is found closest to the experimental data, as assessed using the l_2 -norm of the difference between experimental and simulated data, which is $\Lambda = 11$.

This example also demonstrates a fundamental limitation of the approach, which is that only a finite amount of discrete values for each fitted model parameters can be examined at a time. In cases where the set of values considered is too scarce, regions with strong variations of one parameter might exhibit *staircase*-like features instead of smooth transitions in the parameter maps. While increasing the number of considered values can increase the precision, this also increases the time and complexity of the computations required to obtain the solution.

1.6 Aim of this thesis

On top of the conventional MR imaging procedures, the study and measurement of physical parameters at the origin of the MR signal remain a topic of active research and developments nowadays. As discussed earlier, this stems from the possibilities that these kind of approaches promise to open, such as multi-sites cross-comparisons and more consistent monitoring of disease evolution. However, these methods have yet to be widely adopted by clinicians around the world, in part due to the longer acquisition times required by the current gold standard methods in order to provide accurate quantification of physical tissue properties. To address some of the limitations, and with the recent progress in hardware technology, fast imaging methods, such as bSSFP, hope to provide both high quality images with high signal-to-noise ratios as well as clinically acceptable scan times (Section 1.4.2). These type of sequences are thus prime candidate for the quantification of tissue parameters in the clinical routine and more particularly the relaxation times. However, as seen previously in the case of bSSFP, the image contrast for these type of sequences is often a complex mix of all relevant physical parameters, including both T_1 and T_2 relaxation times.

A recently introduced relaxometry [28] method achieved fast, accurate and precise T_1

and T_2 relaxometry based on a spoiled and unbalanced SSFP acquisition scheme. However, this method is not applicable in 3D inside the human brain due to its inherent motion sensitivity. In the second chapter of this thesis, an attempt is made to address these limitations by using bSSFP and allow the quantification of both relaxation times with minimal influences from main magnetic field (B_0) and transmit field (B_1). Like its predecessor method, the new approach only considers the case where the signal of each voxel originates from single T_1 and T_2 components.

The third chapter of this thesis is concerned with mitigating the presence of banding artefacts in bSSFP images. Using advanced reconstruction techniques and sparse sampling in order to achieve high resolution imaging with minimal scan time, the banding artefacts are effectively “removed from the images” by using quantification based the bSSFP signal equation followed with a synthesis of the on-resonant bSSFP image using the previously estimated parameter maps. The fourth chapter presents an evolution of the latter method based on configuration theory in order to achieve better and more stable banding artefact suppression over a wider range of magnetic field strengths.

Overall, the goal of this thesis is to explore the potential of new quantitative methods based on bSSFP and make a small contribution to the quantitative MRI field, which is destined to be an important part of the future of MRI. The novel methods are investigated in exploratory studies using simulations, water phantoms and last but not least with measurements on healthy volunteers. The results of each method are then compared to the commonly admitted reference techniques.

1.7 Outline

The next chapters of this work explore possible applications of bSSFP for quantitative MRI as well as banding artefacts reduction. First, an application of configuration theory for T_1 and T_2 mapping in Chapter 2. Then in Chapter 3, a closer look at how signal modelling can help generate artefact-free images and finally in Chapter 4 an evolution of the previously introduced method that also includes configuration theory as a way to further improve the robustness and stability of the overall method. In some more details, this thesis is concerned with:

Chapter 2. T_1 and T_2 quantification using the triple echo steady-state (TESS) relaxometry technique [28] suffers from increased motion sensitivity due to the unbalanced steady-state sequence acquisition. In the human brain, this is particularly restricting, as three-dimensional scans cannot be performed due to the natural movements of the cerebrospinal fluid. We therefore propose to replace the direct measurement of the lowest three configurations by an estimation using the Fourier transform of the bSSFP frequency response. The estimation of T_1 and T_2 can then

Chapter 1. Introduction

proceed as previously described in [28]. The accuracy of the new method, termed Motion Insensitive RApid Configuration ReLaxomEtry (MIRACLE), is evaluated inside a manganese-doped water phantom and the human brain at 3 T. Surprisingly, *in vivo* experiments reveal a systematic underestimation of T_1 values, particularly within the white matter, which could be linked to an asymmetric frequency content within the voxels and therefore related to the underlying tissue micro-structure.

Chapter 3. A new method termed *True Constructive Interference in the Steady-State* (trueCISS) is introduced where a highly undersampled acquisition, based on pseudo-random sampling of k -space using a Poisson-disc distribution with central reference region, is combined with a compressed sensing reconstruction and a dictionary fitting to the bSSFP signal equation. This then allows the generation of on-resonant images with genuine bSSFP contrast with virtually no artefacts while the actual scan time remains comparable to conventional banding artefact suppression techniques. The efficiency and stability of the method are assessed using a manganese-doped water phantom as well as human brain acquisitions at 3 T.

Chapter 4. The previously introduced *trueCISS* method is further improved by replacing the less stable and robust dictionary fitting by a direct estimation of both relaxation times ratio and phase linked to off-resonances using the four lowest orders positive and negative configurations. Similarly to the case of MIRACLE, the configurations are estimated from the Fourier transform of the bSSFP frequency response profile. The improved trueCISS method is evaluated inside the human brain at ultra high field strengths such as 7 T and 9.4 T. Overall, the new approach delivers higher quality and smoother parameter maps with less artefacts compared to the original dictionary fitting method. Additionally, parameter mapping methods are well suited to circumvent the more stringent specific absorption rate limitations at ultra-high field strengths by allowing acquisitions with lower flip angles with short repetition times.

References

- [1] Grzegorz Bauman *et al.* “Pulmonary relaxometry with inversion recovery ultra-fast steady-state free precession at 1.5T”. In: *Magn. Res. Med.* 77.1 (Oct. 19, 2016), pp. 74–82. DOI: 10.1002/mrm.26490 (cit. on p. 5).
- [2] Orso Pusterla *et al.* “Rapid 3D in vivo 1H human lung respiratory imaging at 1.5 T using ultra-fast balanced steady-state free precession”. In: *Magn. Res. Med.* 78.3 (Oct. 23, 2016), pp. 1059–1069. DOI: 10.1002/mrm.26503 (cit. on p. 5).
- [3] Orso Pusterla *et al.* “Signal enhancement ratio imaging of the lung parenchyma with ultra-fast steady-state free precession MRI at 1.5T”. In: *J. Magn. Res. Img.* 0.0 (Jan. 3, 2018), pp. 0–0. DOI: 10.1002/jmri.25928 (cit. on p. 5).
- [4] Robert W. Brown *et al.* *Magnetic Resonance Imaging. Physical Principles and Sequence Design*. 2nd Edition. John Wiley & Sons, Inc., 2014. DOI: 10.1002/9781118633953 (cit. on pp. 7, 8).
- [5] M.T. Vlaardingerbroek *et al.* *Magnetic Resonance Imaging. Theory and Practice*. 3rd edition. Springer-Verlag Berlin Heidelberg, 2003. DOI: 10.1007/978-3-662-05252-5 (cit. on pp. 8, 12, 14).
- [6] Dominik Weishaupt *et al.* *How Does MRI Work? An Introduction to the Physics and Function of Magnetic Resonance Imaging*. 2nd Edition. Springer-Verlag Berlin Heidelberg, 2006. DOI: 10.1007/978-3-540-37845-7 (cit. on p. 8).
- [7] Plein Sven *et al.* *Cardiovascular MR Manual*. Ed. by Plein Sven *et al.* 2nd Edition. Springer International Publishing, 2011. DOI: 10.1007/978-3-319-20940-1 (cit. on p. 8).
- [8] Paul S. Tofts *et al.* *Quantitative MRI of the Brain. Measuring Changes Caused by Disease*. Ed. by Paul Tofts. John Wiley & Sons, Ltd, 2004. Chap. 1–6, pp. 1–201. DOI: 10.1002/0470869526 (cit. on p. 8).
- [9] Matt A. Bernstein *et al.* *Introduction to Gradients*. Elsevier Academic Press, 2004. Chap. 8, pp. 243–273. DOI: 10.1016/B978-012092861-3/50010-8 (cit. on p. 12).
- [10] Matt A. Bernstein *et al.* *Handbook of MRI Pulse Sequences*. Elsevier Academic Press, 2004 (cit. on p. 12).
- [11] D. E. Woessner. “Effects of Diffusion in Nuclear Magnetic Resonance Spin-Echo Experiments”. In: *J. Chem. Phys.* 34.6 (June 1961), pp. 2057–2061. DOI: 10.1063/1.1731821 (cit. on p. 14).
- [12] R. Kaiser *et al.* “Diffusion and field-gradient effects in NMR Fourier spectroscopy”. In: *J. Chem. Phys.* 60.8 (Apr. 1974), pp. 2966–2979. DOI: 10.1063/1.1681477 (cit. on p. 14).

Chapter 1. Introduction

- [13] Jürgen Hennig. “Echoes—how to generate, recognize, use or avoid them in MR-imaging sequences. Part I: Fundamental and not so fundamental properties of spin echoes”. In: *Concepts Magn. Res.* 3.3 (July 1991), pp. 125–143. DOI: 10.1002/cmr.1820030302 (cit. on p. 14).
- [14] Jürgen Hennig. “Echoes—how to generate, recognize, use or avoid them in MR-imaging sequences. Part II: Echoes in Imaging Sequences”. In: *Concepts Magn. Res.* 3.3 (July 1991), pp. 179–192. DOI: 10.1002/cmr.1820030302 (cit. on p. 14).
- [15] Carl Ganter. “Steady state of gradient echo sequences with radiofrequency phase cycling: Analytical solution, contrast enhancement with partial spoiling”. In: *Magn. Res. Med.* 55.1 (Jan. 2006), pp. 98–107. DOI: 10.1002/mrm.20736 (cit. on p. 14).
- [16] Matthias Weigel. “Extended phase graphs: Dephasing, RF pulses, and echoes - pure and simple”. In: *J. Magn. Res. Img.* 41.2 (Jan. 2015), pp. 266–295. DOI: 10.1002/jmri.24619 (cit. on pp. 14, 19).
- [17] H. Y. Carr. “Steady-State Free Precession in Nuclear Magnetic Resonance”. In: *Phys. Rev.* 112 (5 Dec. 1, 1958), pp. 1693–1701. DOI: 10.1103/PhysRev.112.1693 (cit. on p. 14).
- [18] O. Bieri *et al.* “Flow compensation in balanced SSFP sequences”. In: *Magn. Res. Med.* 54.4 (Sept. 2, 2005), pp. 901–907. DOI: 10.1002/mrm.20619 (cit. on p. 15).
- [19] Klaus Scheffler *et al.* “Principles and applications of balanced SSFP techniques”. In: *Eur. Radiol.* 13.11 (Nov. 1, 2003), pp. 2409–2418. DOI: 10.1007/s00330-003-1957-x (cit. on p. 16).
- [20] Carl Ganter. “Static susceptibility effects in balanced SSFP sequences”. In: *Magn. Res. Med.* 56.3 (June 2006), pp. 687–691. DOI: 10.1002/mrm.20986 (cit. on p. 17).
- [21] Y. Zur *et al.* “Motion-insensitive, steady-state free precession imaging”. In: *Magn. Res. Med.* 16.3 (June 29, 1990), pp. 444–459. DOI: 10.1002/mrm.1910160311 (cit. on pp. 19, 20).
- [22] K L Miller. “Asymmetries of the balanced SSFP profile. Part I: theory and observation”. In: *Magn. Res. Med.* 63.2 (Jan. 23, 2010), pp. 385–395. DOI: 10.1002/mrm.22212 (cit. on p. 20).
- [23] K L Miller *et al.* “Asymmetries of the balanced SSFP profile. Part II: white matter”. In: *Magn. Res. Med.* 63.2 (Jan. 23, 2010), pp. 396–406. DOI: 10.1002/mrm.22249 (cit. on p. 20).
- [24] Michael Lustig *et al.* “Sparse MRI: The application of compressed sensing for rapid MR imaging”. In: *Magn. Res. Med.* 58.6 (Oct. 29, 2007), pp. 1182–1195. DOI: 10.1002/mrm.21391 (cit. on p. 21).
- [25] Dan Ma *et al.* “Magnetic resonance fingerprinting”. In: *Nature* 495 (Mar. 13, 2013), pp. 187–192. DOI: 10.1038/nature11971 (cit. on p. 21).

- [26] Mark A. Griswold *et al.* “Generalized autocalibrating partially parallel acquisitions (GRAPPA)”. In: *Magn. Res. Med.* 47.6 (June 7, 2002), pp. 1202–1210. DOI: 10.1002/mrm.10171 (cit. on p. 21).
- [27] Klaas P. Pruessmann *et al.* “SENSE: Sensitivity encoding for fast MRI”. In: *Magn. Res. Med.* 42.5 (Oct. 28, 1999), pp. 952–962. DOI: 10.1002/(SICI)1522-2594(199911)42:5<952::AID-MRM16>3.0.CO;2-S (cit. on p. 21).
- [28] Rahel Heule *et al.* “Triple echo steady-state (TESS) relaxometry”. In: *Magn. Res. Med.* 71.1 (Apr. 2, 2013), pp. 230–237. DOI: 10.1002/mrm.24659 (cit. on pp. 24–26).

2 Motion-Insensitive Rapid Configuration Relaxometry

Damien Nguyen^{1,2} and Oliver Bieri^{1,2}

¹Division of Radiological Physics, Department of Radiology, University Hospital Basel, University of Basel, Basel, Switzerland

²Department of Biomedical Engineering, University of Basel, Basel, Switzerland

2.1 Introduction

Quantification is thought to represent an important step toward significant improvements of the diagnostic potential of MRI, such as for the early detection of subtle or diffuse pathological changes with high specificity and sensitivity, for an unbiased assessment of treatment or drug effects, as well as for clinical trials in drug research across different sites and machines. Quantitative imaging, however, is rather time consuming and typically becomes an issue in the clinical environment, where the overall success and applicability of quantitative MRI strongly depends on the overall acquisition speed. In this context, SSFP-based imaging techniques [1] have shown compelling results thanks to their short scan times and high signal-to-noise ratios, e.g., for relaxation time mapping [2–8], for measuring molecular proton diffusion [9–13], for the assessment of magnetization transfer effects [14–16], or for the characterization of flow or motion [17–19].

Generally, relaxation occupies a central role within the context of NMR: it not only defines contrast in conventional MRI but also reflects the interaction of water on a molecular level. Historically, longitudinal relaxation (T_1) has been estimated by sampling the inversion-recovery curve of the longitudinal magnetization using spin-echo sequences, while the transverse relaxation (T_2) time has been estimated from the decay curve of the transverse magnetization using single-echo or, more frequently, multiecho spin-echo (SE) methods. Quantification based on the functional dependencies of the steady state, however, is much faster. One common attribute of SSFP methods is their mixed T_2/T_1 imaging contrast [20]; being a natural consequence of a pulse repetition time (TR) that is much shorter than T_2 . Consequently, accurate quantification of relaxation times using SSFP-based imaging techniques is usually hampered by a T_2 -related bias in T_1 estimates for radio-frequency (RF) spoiled SSFP [21, 22], or by a T_1 -related bias in T_2 , as observed with balanced SSFP (bSSFP) [23], partially spoiled SSFP [8], and double echo steady SSFP [7]. Moreover, all previously mentioned methods are sensitive to transmit field (B_1) inhomogeneities, whereas some of them show, in addition, some sensitivity to off-resonances [24] or

motion [7, 8].

Recently, Heule *et al.* [25] proposed to tackle the mutual interference of T_1 and T_2 of coherent SSFP methods by using a triple echo steady state (TESS) imaging approach. To this end, TESS acquires the three lowest SSFP configuration modes within a single acquisition (or TR) yielding two independent ratios for simultaneous rapid quantification of both T_1 and T_2 using a golden section search. Quite remarkably, TESS achieves an almost completely B_1 -unbiased estimation of T_2 , and showed good prospects for rapid three-dimensional (3D) T_2 mapping of articular cartilage imaging in the clinical setting [26]. Generally, TESS is also insensitive to B_0 inhomogeneities but the nonbalanced gradient scheme introduces some motion sensitivity that can be softened with a single-slice version of TESS providing high quality T_2 maps in the human brain even at ultra-high fields [27]. More recently, a simultaneous multislice TESS sequence [28] was proposed to decrease scan time without loss of image quality.

In this work, we aim to replace the unbalanced gradient scheme of TESS by a balanced one leading to “motion-insensitive rapid configuration relaxometry”, termed MIRACLE [29], that indirectly retrieves the basic SSFP modes from a series of bSSFP scans. The accuracy of MIRACLE-based relaxometry is evaluated from simulations and phantom experiments. The feasibility of high-resolution volumetric T_1 - and T_2 -mapping is demonstrated in vivo for the human brain and for articular cartilage at 3 T.

2.2 Methods

MIRACLE

In the following analysis, we consider an equidistant train of RF pulses with constant flip angles and constant RF phase increment in combination with balanced gradient moments. Finite RF pulse and diffusion effects are considered to be negligible. Immediately after the RF pulse (counterclockwise rotation around x-axis), the complex steady state magnetization $M_+(t = 0)$ is given by (e.g., following Ganter [30])

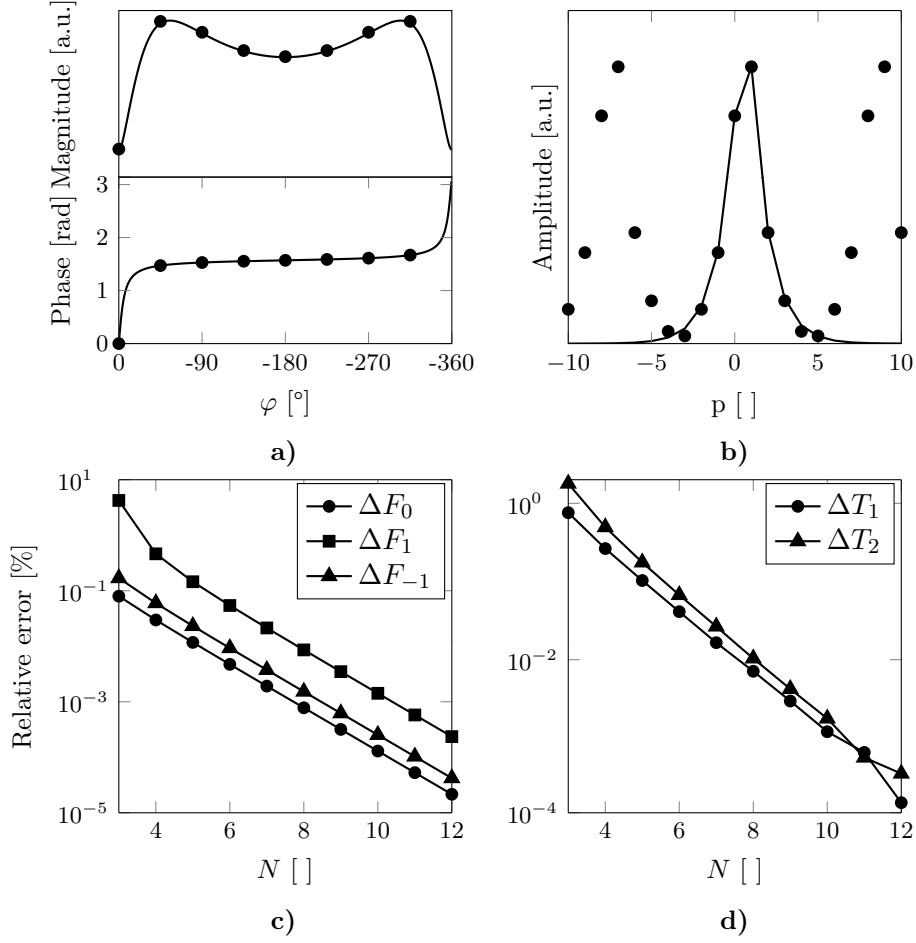


Figure 2.1 – **a** Simulation of the bSSFP steady state signal, as a function of the RF phase increment φ (simulation parameters: $T_1/T_2/TR = 860/70/5.76$ ms, $\alpha = 15^\circ$, proposed optimal for TESS imaging [25]). **b** Derived modes F_p from N -point Fourier transform using Eq. (2.9) (dots: $N = 8$ RF phases φ_j , see Eq. (2.5); solid line: continuous RF φ ; a continuous line is shown in **b** that connects the derived mode amplitudes for improved visualization). Relative mode **c** and relaxation estimation error **d** as a function of the number N of bSSFP scans performed using the same parameter set as above.

$$\begin{aligned}
 M_+(t=0) &\triangleq M_x(t=0) + iM_y(t=0) \\
 &= \frac{-i}{D} (1 - E_1) \sin \alpha \left(1 - E_2 e^{-i\vartheta} \right)
 \end{aligned} \tag{2.1}$$

$$\begin{aligned}
 D &\triangleq (1 - E_1 \cos \alpha)(1 - E_2 \cos \vartheta) \\
 &\quad - (E_1 - \cos \alpha)(E_2 - \cos \vartheta) E_2
 \end{aligned} \tag{2.2}$$

where $E_i = \exp(-TR/T_i)$ and $\vartheta = \Phi - \varphi$ denotes the phase difference between the off-resonance related phase Φ accumulated during each repetition time (TR) interval (and is assumed to

be constant in time), and the RF pulse phase increment φ . At a time t after the RF pulse, the magnetization is given by

$$M_+(t) = M_+(t=0) e^{-t/T_2} e^{i\phi(t)} \tag{2.3}$$

where $\phi(t) \triangleq t/TR \cdot \Phi$. Generally, the steady state as given in Eqs. (2.1) and (2.2) is periodic in φ and can be expressed a sum over all configurations orders F_n [30, 31]

$$M_+(\varphi, t) = e^{-t/T_2} e^{i\Phi t/TR} \sum_{n=-\infty}^{+\infty} F_n e^{in(\Phi - \varphi)} \tag{2.4}$$

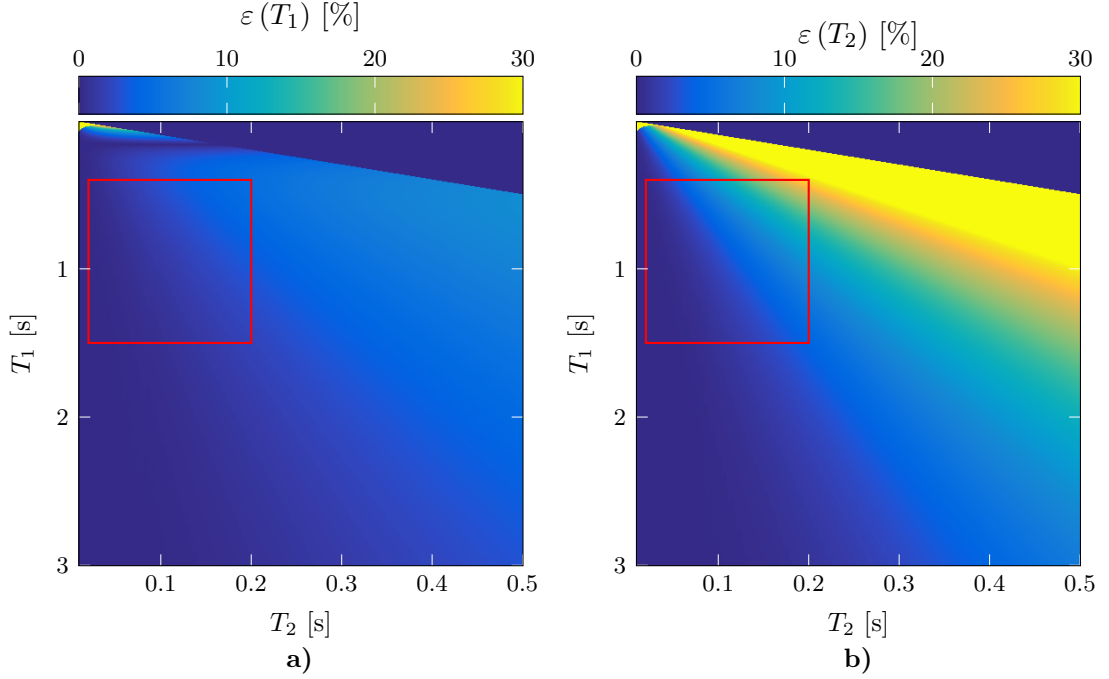


Figure 2.2 – MIRACLE estimation error $\varepsilon(T_i) = |T_{i\text{MIRACLE}} - T_i|$ as a function of the simulated T_1 **a** and T_2 **b** for a fixed $N = 8$. The delimited region (red) shows typical parameter ranges for human tissues (for simulation parameters: see Fig. 2.1).

As shown previously in a seminal work by Zur *et al.* [31], it is possible to retrieve the basic SSFP configurations or modes F_n (see Eq. [4]) from a discrete Fourier transformation of the complex bSSFP frequency response. To this end, we proceed as follows:

1. We perform N scans with an RF phase increment of

$$\varphi_j \triangleq -\frac{2\pi}{N}j, j = 0, 1, \dots, N-1 \quad (2.5)$$

where j enumerates the scan. As a result, the magnetization in Eq. (2.4) is modified to take the formation

$$\begin{aligned} M_+(\varphi, t) &= \sum_{n=-\infty}^{+\infty} e^{-t/T_2} e^{i\Phi t/\text{TR}} F_n e^{in(\Phi-\varphi)} \\ &\triangleq \sum_{n=-\infty}^{+\infty} M_n(\Phi, t) e^{i(2\pi/N)nj} \quad (2.6) \end{aligned}$$

2. We calculate the N -point Fourier transform

of the $M_+(\varphi, t)$ magnetisations

$$\begin{aligned} G(p, t) &= \frac{1}{N} \sum_{j=0}^{N-1} M_+(\varphi_j, t) e^{-i(\frac{2\pi}{N})jp} \\ &= \frac{1}{N} \sum_{j=0}^{N-1} \sum_{n=-\infty}^{+\infty} M_n(\Phi, t) e^{i(\frac{2\pi}{N})j(n-p)} \quad (2.7) \end{aligned}$$

and because

$$\sum_{j=0}^{N-1} e^{i(2\pi/N)j(n-p)} = \begin{cases} N, & \text{if } \frac{n-p}{N} \text{ is an integer} \\ 0, & \text{otherwise} \end{cases} \quad (2.8)$$

this yields

$$\begin{aligned} G(p, t) &= e^{-t/T_2} e^{i\phi(t)} \left(F_p e^{ip\Phi} + F_{p\pm N} e^{i(p\pm N)\Phi} \right. \\ &\quad \left. + F_{p\pm 2N} e^{i(p\pm 2N)\Phi} + \dots \right) \quad (2.9) \end{aligned}$$

As a result of the finite number of scans (N), aliasing occurs (see Eq. (2.9)). Generally, however, the mode amplitudes decrease rapidly with increasing mode order $|p|$ and thus for large

enough N ,

$$G(p, t) \approx e^{-t/T_2} e^{i\phi(t)} F_p e^{ip\Phi} \quad (2.10)$$

and, therefore,

$$|G(p, t)| \approx e^{-t/T_2} |F_p| \quad (2.11)$$

Following the approach of Heule *et al.* [25], estimation of the relaxation times T_1 and T_2 was then performed based on a golden-section search algorithm [32] using the two signal ratios

$$\frac{|G(1, t)|}{|G(0, t)|} \approx \frac{|F_1|}{|F_0|} \quad (2.12)$$

$$\frac{|G(-1, t)|}{|G(0, t)| - |G(1, t)|} \approx \frac{|F_{-1}|}{|F_0| - |F_1|} \quad (2.13)$$

in an iterative approach relying on the fact that both ratios show different dependencies on T_1 and T_2 as was shown in Heule et al Heule *et al.* [25]. From Eq. (2.10) and in the limit where the amplitudes of higher-order F_n modes are negligible (i.e., for large enough N), only the phase of the SSFP modes depends on the local off-resonance Φ . As a result, the signal ratios used for estimation of T_1 (cf. Eq. (2.12)) and T_2 (cf. Eq. (2.13)) are off-resonance insensitive. A global initial estimate of $T_1 = 1000$ ms was used for all simulations and experiments and a tolerance of 0.1 ms was assumed as convergence criteria for the iterative search. Similarly to TESS relaxometry, we expect T_1 estimates to have some remaining B_1 -bias, while T_2 is anticipated to be largely free of any B_1 bias.

Simulations and Imaging

All numerical simulations, data analysis and visualizations were done using MATLAB 8.5 (The MathWorks Inc., Natick, MA). Measurements and calibrations were performed on a clinical 3 Tesla (T) whole body system (Siemens MAGNETOM Prisma, Erlangen, Germany) with actively shielded magnetic field gradient coils. Acquisitions were performed using the standard 20-channel head coil and a 15-channel Tx/Rx knee coil. Gibb's ringing was removed from base data as recently proposed by Kellner *et al.* [33].

Simulations of the bSSFP signal were performed

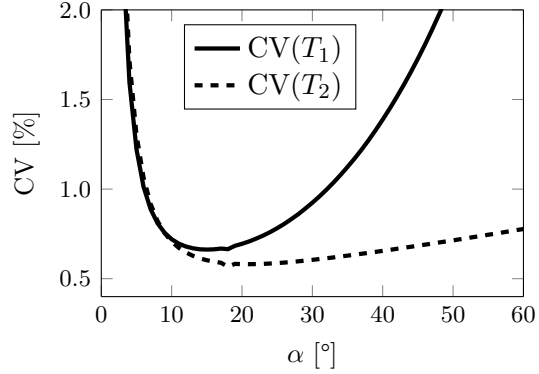


Figure 2.3 – Coefficient of variation (CV) for T_1 and T_2 as a function of the flip angle α , estimated by a Monte-Carlo simulation for a $N = 8$ MIRACLE acquisition with 1% noise added to the bSSFP signal (for simulation parameters: see Fig. 2.1).

for a T_1/T_2 – ratio 12 using sets of 4 to 12 scans with a TR/echo time (TE) of 5.76/2.88 ms and RF phase increments φ_j , as given by Eq. (2.5). Evaluation of the accuracy of the proposed method for a range of T_1 and T_2 with an eight-point sampling scheme was performed using the same set of parameters. The influence of the flip angle on the estimation of the relaxation parameters was evaluated by performing a Monte-Carlo simulation with 100,000 independent runs for a $N = 8$ phase cycling scheme with flip angles between 1° and 60° and the addition of 1% Gaussian white noise to simulate experimental conditions. For each flip angle, the coefficient of variation (CV) for both relaxation parameters was calculated (defined as the ratio of the standard deviation and the mean over all runs; $CV(T_i) \triangleq \Delta T_i / \bar{T}_i, i = 1, 2$).

Phantom experiments were performed on a manganese-doped spherical phantom composed of 0.125 mM $MnCl_2$ dissolved in water (with nominal T_1/T_2 values of 860/70 ms [25] and approximately 14 cm in diameter using an eight-point 3D MIRACLE scheme with the following protocol parameters: TR/TE = 5.10/2.55 ms, $\alpha = 15^\circ$, a resolution of $1 \times 1 \times 2$ mm³ (image matrix: $208 \times 162 \times 80$), a bandwidth of 401 Hz px⁻¹, elliptical scanning and RF phase increments φ_j as given by Eq. (2.5). With this setup, an overall scan time of approximately 7 min was obtained. The 3D TESS relaxometry was realized using the same parameters, except for TR/TE =

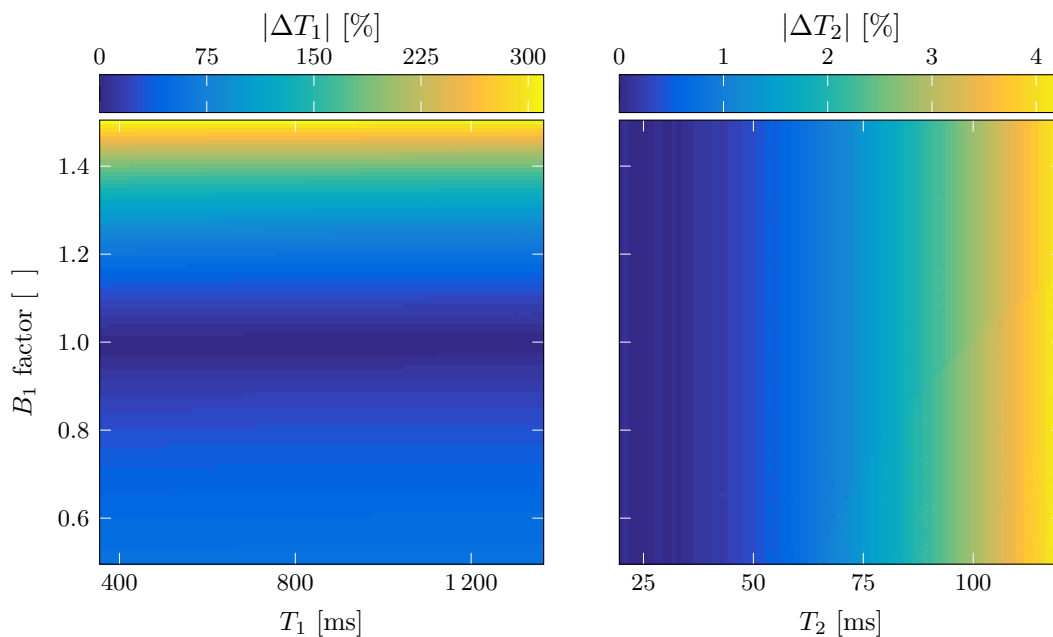


Figure 2.4 – Relative deviation between the estimated and simulated T_1 and T_2 as a function of the B_1 homogeneity. Note the different scaling for T_2 , which is virtually unaffected by B_1 (for simulation parameters: see Fig. 2.1).

6.19/3.17 ms, 2 averages and a bandwidth of 800 Hz px^{-1} for a total scan time of 8 min. Reference T_1 relaxometry was realized using a single-slice inversion-recovery turbo spin-echo (IR-TSE) sequence with $\text{TR}/\text{TE} = 5000/13 \text{ ms}$, and inversion times (TI) of 50 ms, 100 ms, 200 ms, 400 ms, 800 ms, 1600 ms and 3200 ms. Estimation of T_1 was obtained from a nonlinear fit of the recovery curve [34]. Further scanning parameters include turbo factor (TF) 7, $\alpha = 180^\circ$, an in-plane resolution of 1 mm^2 (image matrix: 208×168), slice thickness 2 mm, a bandwidth of 130 Hz px^{-1} , GRAPPA 2 with 34 reference lines for a scan time of 1:17 min (8:59 min total). Furthermore, reference T_2 relaxometry was performed using single echo spin-echo (SE) sequence with a TR of 1500 ms, and a TE of 10 ms, 20 ms, 40 ms, 80 ms, 150 ms and 250 ms, $\alpha = 180^\circ$, an in-plane resolution of 1 mm^2 (image matrix: 208×168), slice thickness 2 mm, a bandwidth of 201 Hz px^{-1} , GRAPPA 2 with 34 reference lines resulting in 1:30 min/acquisition (9:0 min total). T_2 mapping was performed using a maximum likelihood estimator approach, as described by Golub *et al.* [35].

Exemplary in vivo human brain imaging using a

3D slab of 36 axial slices located inside the brain was performed using a 12-points bSSFP cycling scheme with a $\text{TR}/\text{TE} = 5.10/2.55 \text{ ms}$, $\alpha = 15^\circ$, a resolution of $1 \times 1 \times 2 \text{ mm}^3$ (image matrix: $192 \times 150 \times 36$), a bandwidth of 400 Hz px^{-1} , elliptical scanning and RF phase increments φ_j following Eq. (2.5), resulting in a total scan time of approximately 5:30 min. Reference T_1 data were acquired using a 2D single-slice IR-TSE with identical sequence parameters as for the phantom scans, but with a resolution of 1 mm^2 (image matrix: 192×150) leading to a scan time of 1:12 min (8:24 min total). Additionally, reference T_2 data was obtained from a single echo 2D SE scan with 1 mm^2 in-plane resolution (image matrix: 192×150) but otherwise identical to the phantom case, resulting in 1:57 min/acquisition (11:42 min total). High resolution images of the right knee were realized in axial orientations using a similar protocol with a $\text{TR}/\text{TE} = 6.46/3.23 \text{ ms}$, a resolution of $0.6 \times 0.6 \times 3 \text{ mm}^3$ (image matrix: $368 \times 220 \times 20$), and a bandwidth of 300 Hz px^{-1} and elliptical scanning yielding a scan time of around 5:40 min.

For each series of scans, additional patient-specific B_1 maps were acquired using the method

Chapter 2. Motion-Insensitive Rapid Configuration Relaxometry

proposed by Ganter *et al.* [36]. Registration of B_1 data onto the on-resonant image of each MIRACLE dataset was accomplished before B_1 correction using routines from the FSL libraries [37, 38] for brain images or by using the elastix registration program [39, 40] in other cases.

2.3 Results

A noise-free simulation of the complex bSSFP frequency response (cf. Eqs. (2.1) and (2.2)) is presented in Figure 2.1a for a tissue mimicking a T_1/T_2 -ratio of approximately 12 for a $N = 8$ point phase cycling scheme and in the limit of a continuous RF phase increment. The corresponding Fourier transforms (cf. Eq. (2.9)) are shown in Figure 2.1b. Aliasing in the case of a finite N becomes evident and generally leads to a systematic deviation between the true mode amplitudes and the ones using N-point Fourier transform; especially for higher configuration orders (p) (see Fig. 2.1b). As expected, increasing the number N of RF phases φ_j improves the overall accuracy of the mode amplitude estimates (see Fig. 2.1c), and do not exceed 1.2% for the lowest order modes ($p = -1, 0, 1$) for $N \geq 8$. The resulting T_1 and T_2 estimation error follows a similar trend (see Fig. 2.1d), and is in the absence of noise below 0.01% for a T_1/T_2 12 in combination with phase cycling acquisition schemes using $N \geq 8$.

Analysis of the estimation error $\varepsilon(T_i) = |T_{i\text{MIRACLE}} - T_i|$, as a function of T_1 and T_2 , is presented in Figure 2.2 for a fixed $N = 8$ MIRACLE acquisition scheme. The overall error is in general much larger for T_2 than for T_1 , indicating the need to acquire more than 8 phase-cycles for T_2 values exceeding roughly 100 ms.

Generally, the decay of the modes (F_p with increasing mode order $|p|$), e.g., as observed in Fig. 2.1b, not only depends on the relaxation, but also on the flip angle α (cf. Eqs. (2,12) in Ganter [41]). As a result, different flip angle settings might be required for MIRACLE as compared to TESS. In line with the flip angle optimization results for TESS, however, Monte-Carlo simulations also revealed for MIRACLE a clear

optimum for flip angles around 15° (see Fig. 2.3).

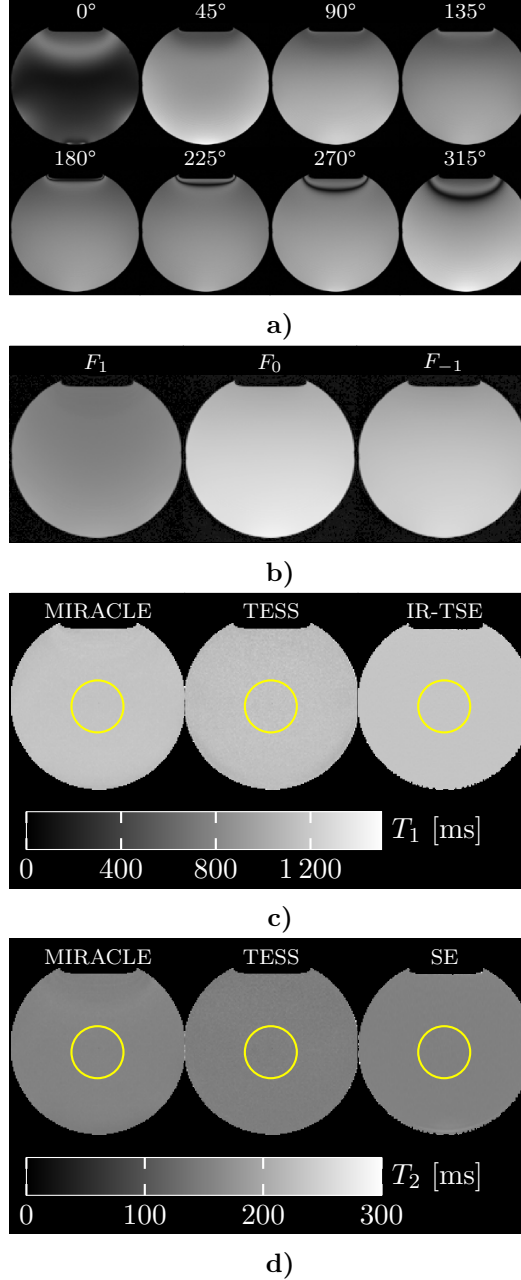


Figure 2.5 – Illustration of MIRACLE relaxometry calculations using an $N = 8$ phase cycling scheme for a manganese-doped probe. **a** Source bSSFP magnitude images. **b** Derived three lowest SSFP mode images F_1 , F_0 , F_{-1} . **c** Estimated T_1 and T_2 maps (initial guess of $T_1 = 1$ s, precision enforced: 0.1 ms). **d** Relaxation parameters were assessed for a region of interest, as indicated in the relaxation maps by the circles. (imaging parameters: $N = 8$ of $1 \times 1 \times 2 \text{ mm}^3$ and TR/TE 5.00/2.50 ms).

Consequently, this flip angle was used for all subsequent acquisitions. Moreover, in complete analogy to TESS imaging, the estimation of T_2 is found to be largely insensitive to B_1 , whereas the T_1 estimates retain the usual B_1 dependency. The bias in both T_1 and T_2 , as introduced by flip angle miscalibrations is shown in Figure 2.4. For a fixed T_1 , the error in T_1 scales approximately linearly with relative B_1 values ranging from 0.5 to 1.5, whereas the bias in T_2 from B_1 (for fixed T_1 values) is less than 0.1 ms over the whole investigated B_1 -range.

Tissue	Method	T_1 [ms]	T_2 [ms]
Phantom	MIRACLE	835 ± 16	70 ± 2
	TESS (3D)	823 ± 38	65 ± 9
	Reference	850 ± 9	67 ± 1
Brain WM	MIRACLE	532 ± 56	44 ± 5
	Reference	840 ± 28	51 ± 2
Brain GM	MIRACLE	1061 ± 169	63 ± 12
	Reference	1352 ± 69	57 ± 3
Cartilage	MIRACLE	1194 ± 436	42 ± 9
Muscle	MIRACLE	846 ± 130	33 ± 10
Fat	MIRACLE	307 ± 23	102 ± 13

Table 2.1 – Estimated Relaxation Parameters from 3D MIRACLE, 3D TESS, and 2D Single Slice Reference Measurements (IR-TSE and SE) in phantom and *in vivo*

Motion-insensitive SSFP mode imaging and subsequent relaxometry is now exemplarily illustrated in Figure 2.5 at 3T for a manganese-doped spherical probe. Figure 2.5a depicts the original $N = 8$ phase-cycled bSSFP images, Figure 2.5b shows the resulting mode images for F_0 , F_1 and F_{-1} , and Figures 2.5c and 2.5d present the estimated T_1 and T_2 maps from 3D MIRACLE, 3D TESS, IR-TSE, and SE measurements. Both MIRACLE- T_2 and TESS- T_2 exhibit no spatial variations across the whole imaging volume. MIRACLE- T_1 and TESS- T_1 estimates have already been corrected for B_1 inhomogeneities by using the separately acquired B_1 map, which results in flat T_1 profiles over the whole field-of-view. Overall, very good agreement is found between all three methods for both T_1 and T_2 . Evaluation of relaxation parameters within the indicated region-of-interest (ROI) are collected in Table 2.1 for all three methods.

High resolution *in vivo* 3D brain T_1 and T_2 mapping with MIRACLE and reference measurements is demonstrated in Figure 2.6 at 3T in axial slice orientation. In contrast to 3D

TESS, no pulsation artifacts are noticeable in the derived base mode images (Figure 2.6a and Supporting Figure 2.10, which is available online, for 3D TESS brain images) and, as a result, successful T_1 and T_2 mapping is demonstrated in 3D (Figs. 2.6b and 2.6c) using motion-insensitive SSFP [31]. For comparison, reference IR-TSE and SE results are also presented for the same slice. Evaluation of relaxation parameters inside highlighted ROIs can be found inside Table 2.1.

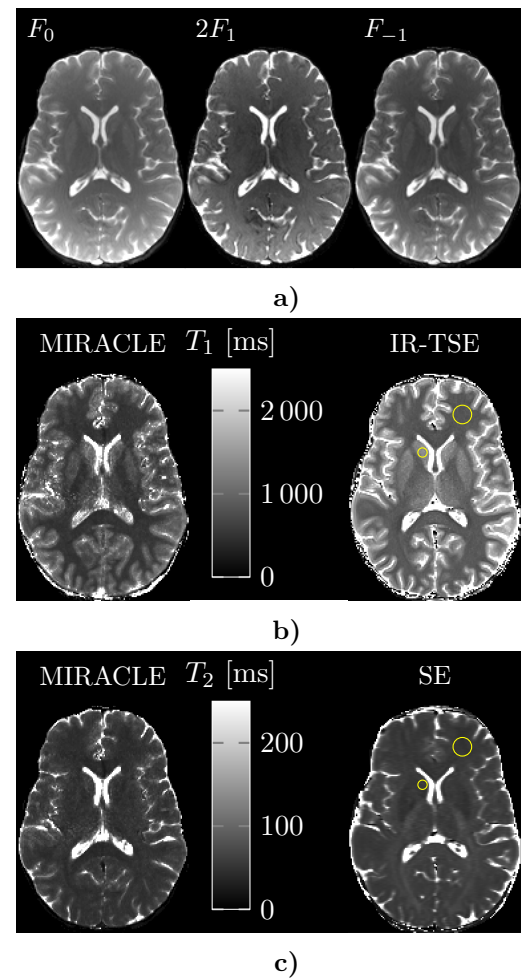


Figure 2.6 – Illustrative volumetric MIRACLE brain imaging of a healthy volunteer. **a** Axial sample images from the derived three lowest SSFP mode volumes F_0 , F_1 , F_{-1} (note the different scaling for F_1). **b** Corresponding T_1 (ms) map. **c** Corresponding T_2 (ms) map. (Imaging parameters: $N = 12$, resolution: $1 \times 1 \times 2 \text{ mm}^3$, $TR/TE=5.76/2.88 \text{ ms}$)

Finally, 3D MIRACLE imaging is demonstrated in the knee joint (Fig. 2.7) at 3T in axial slice

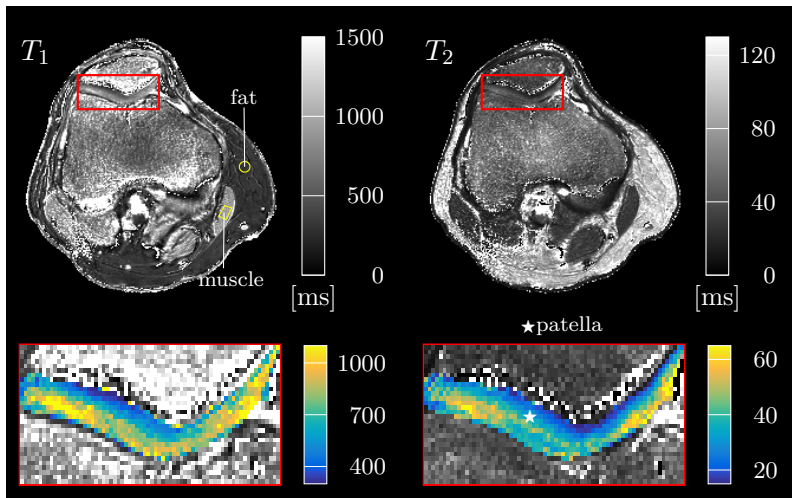


Figure 2.7 – Illustrative T_1 and T_2 maps (in [ms]), as derived from a 3D axial MIRACLE knee scan of a healthy volunteer. Note the typical decrease in both T_1 and T_2 for patellar cartilage from superficial to deep layers. (Imaging parameters: $N = 12$, resolution: $0.6 \times 0.6 \times 3 \text{ mm}^3$ TR/TE = 6.46/3.23 ms)

orientation. See Table 2.1 for the evaluation of T_1 and T_2 within marked ROIs. Zonal variation in patellar cartilage T_1 and T_2 is clearly visible with a decrease in both T_1 and T_2 values from superficial to deep layers, as typically expected and observed for healthy cartilage (see insets, Fig. 2.7).

2.4 Discussion

Indirect estimation of the lowest order SSFP modes for rapid T_1 and T_2 mapping from a set of phase-cycled bSSFP scans using a Fourier transformation yields similar properties as TESS relaxometry. Furthermore, due to the balanced gradients used in the present case, MIRACLE relaxometry is expected to be less sensitive to diffusive effects than TESS, particularly in fluids [27]. Still, it is important to remember that the accuracy of the presented method relies on the ability to correctly retrieve the SSFP mode amplitudes F_{-1} , F_0 and F_1 from the bSSFP profile. This not only depends on the number N of RF phase increments used, but also on how fast the configurations decay with increasing order $|p|$ (e.g., see Fig. 2.1b). For $TR \ll T_1$, the decay of the mode amplitudes becomes a function of the flip angle α and the relaxation time ratio T_1/T_2 [41]. As a result, aliasing becomes more and more an issue with decreasing T_1/T_2 , e.g., as observed

in Figure 2.4, where the error in T_2 increases with increasing T_2 (for a constant T_1). Consequently, accurate relaxometry of fluids might not be granted, even for $N = 12$. Nonetheless, the phantom data show that MIRACLE is in very good agreement with both 3D TESS and reference IR-TSE and SE methods for tissue-like T_1/T_2 ratios. In addition to the aforementioned effects, patient movements between phase-cycles may affect the success of MIRACLE relaxometry, although adequate fixation and image registration could be used to mitigate such effects.

Typical T_1 -values reported in the literature for white and gray brain matter are approximately 950 to 1000 ms [42] and 1300 to 1500 ms [43, 44], respectively, which are similar to what was obtained during our reference measurements. Interestingly, and in contrast to the simulations as well as phantom and cartilage experiments, *in vivo* brain imaging with MIRACLE demonstrates a systematic underestimation of T_1 even after B_1 correction. This bias is likely linked to the asymmetric shape of the bSSFP frequency response, as exemplified in Figure 2.8 for brain tissue, but more prominently for white as compared to gray matter. Those asymmetries have already been discussed in some details by Miller [45] and Miller *et al.* [46] and are believed to be due to an inhomogeneous intra-voxel frequency content. This is not unexpected as

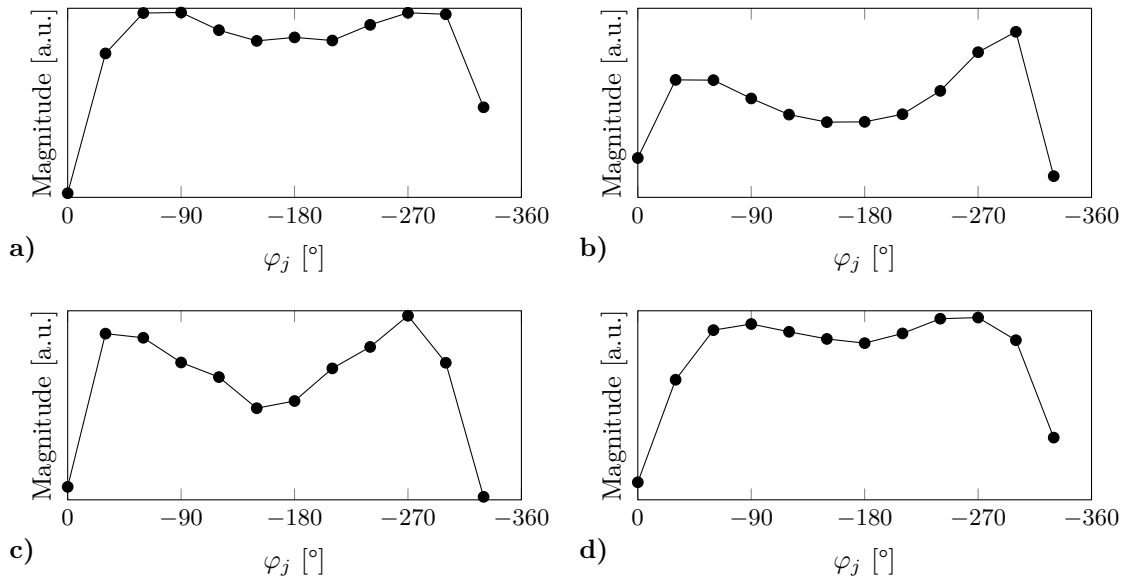


Figure 2.8 – Exemplary bSSFP frequency response for gray **a** and white **b** brain matter (for the definition of ROIs, see Figure 2.6), as well as, for patellar cartilage **c** and muscle tissues **d** (for the definition of ROIs, see Figure 2.7). Note the increased asymmetry in the case of white versus gray brain matter.

brain tissues contain microstructural boundaries, compartments or chemical shifts that might not be properly characterized by a single pair of relaxation parameters and thus by a single-compartment signal behavior as assumed by Equations (2.1) and (2.2). To further investigate these effects, noise-free simulations of the bSSFP signal in the case of a two-components model assuming Lorentzian line shapes were performed. As was initially proposed by Miller *et al.* [46], we assume identical T_1 and T_2 (830/80 ms) for both components, a fixed line width of $\Gamma_1 = 0.1$ Hz for the first component, and a volume fraction of 0.15 for the second component. Corresponding MIRACLE- T_1 and $-T_2$ values as a function of the second component's width (Γ_2) and frequency shift (Δf) are shown in Figure 2.9a. Because this results in an overestimation rather than an underestimation of T_1 , this model fails to describe the observed MIRACLE brain data.

Generally, the constraint of having the same relaxation properties for both components might be too restrictive. Deoni *et al.* [47] suggested a two-component system with a volume fraction of roughly 0.28 for white matter, where the dominating component has a rather low T_1/T_2 -ratio of 900/120 ms, in contrast to a rather high T_1/T_2 -ratio of 380/10 ms for the smaller

component, reflecting myelin. Note that contrary to the aforementioned study, we do not consider exchanges between species in the present case. We now repeat the analysis done previously and show the corresponding MIRACLE results in Figure 2.9b. Within this framework, we observe a shift to apparent low T_1 values in combination with typical T_2 values that are in good agreement with the MIRACLE- T_1 and $-T_2$ values from our experiments. Consequently, the low T_1 values observed in vivo are likely to originate from the presence of a myelin-like second component with different frequency distribution, in line with the observation that the resulting bias in T_1 is much less pronounced for gray matter, where lower myelin contents are expected. The aforementioned suspected sensitivity of MIRACLE to tissue heterogeneity and frequency asymmetry is further corroborated by the results observed for articular cartilage. Here, the observed T_1 and T_2 values are in very good agreement to previously published values [25, 48], which is expected because cartilage is known to be much less heterogeneous [49].

In summary, T_1 and T_2 mapping with MIRACLE offers analogous properties as TESS while successfully mitigating its motion-sensitivity. In contrast to the literature, however, apparent low T_1 values are observed for brain white matter;

Chapter 2. Motion-Insensitive Rapid Configuration Relaxometry

reflecting the asymmetry in the bSSFP signal profile. As a result, a configuration-based relaxometry, as suggested with MIRACLE, becomes sensitive to changes in the underlying frequency spectrum and content, and might, therefore, offer improved sensitivity to diffuse pathophysiological changes in the brain. Future work will aim to explore this new frequency-sensitive relaxometry method.

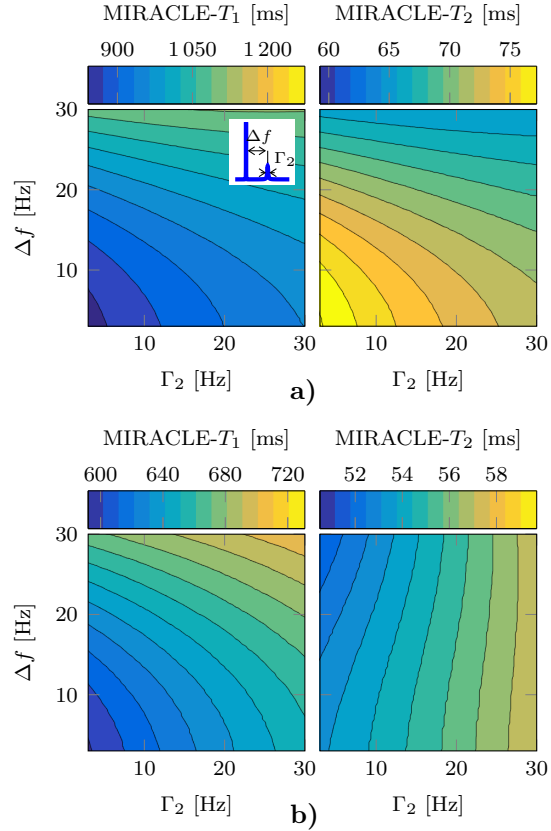


Figure 2.9 – Estimated MIRACLE T_1 and T_2 from a simulated two-component system with identical T_1/T_2 values of 830/80 ms and a volume fraction of 0.15 **a**, and T_1/T_2 values of 900/120 ms and 380/10 ms **b**, respectively, as well as a volume fraction of 0.28. The inset in **a** depicts the parameter space investigated: the first component is assumed to be on-resonant with a width $\Gamma = 0.1$ Hz, whereas the values for the width Γ_2 and frequency shift Δf of the second component are varied as shown above. Typical values reported by Miller *et al.* [46] for white matter are $\Delta f = 17$ to 23 Hz and $\Gamma_2 = 19$ to 22 Hz (depending on the orientation).

2.5 Conclusion

A rapid motion-insensitive configuration-based steady state relaxometry method was presented. Compared with most SSFP methods, it offers accurate and robust T_2 quantification of human tissues, even in the presence of substantial B_0 and B_1 field inhomogeneities, as demonstrated in the scope of this work. In contrast to contemporary single component relaxometry methods, however, our results and preliminary modelling indicate that MIRACLE becomes sensitive to the T_1 and T_2 intra-voxel frequency dispersion.

Acknowledgment

We thank Rahel Heule for proofreading the manuscript.

Supporting Information

Additional Supporting Information may be found in the online version of this article.
DOI: 10.1002/mrm.26384.

References

- [1] H Y Carr. “Steady-State Free Precession in Nuclear Magnetic Resonance”. In: *Phys Rev* 112.5 (1958), pp. 1693–1701. DOI: 10.1103/PhysRev.112.1693 (cit. on p. 33).
- [2] D. C. Look *et al.* “Time saving in measurement of NMR and EPR relaxation times”. In: *Rev. Sci. Instrum.* 41.2 (1970), pp. 250–251. DOI: 10.1063/1.1684482 (cit. on p. 33).
- [3] John Homer *et al.* “Driven-equilibrium single-pulse observation of T1 relaxation. A reevaluation of a rapid “new” method for determining NMR spin-lattice relaxation times”. In: *J. Magn. Reson.* 63.2 (1985), pp. 287–297. DOI: 10.1016/0022-2364(85)90318-X (cit. on p. 33).
- [4] Klaus Scheffler *et al.* “T1 quantification with inversion recovery TrueFISP”. In: *Magn. Reson. Med.* 45.4 (2001), pp. 720–723. DOI: 10.1002/mrm.1097 (cit. on p. 33).
- [5] Sean C L Deoni *et al.* “Rapid combined T1 and T2 mapping using gradient recalled acquisition in the steady state.” In: *Magn. Reson. Med.* 49.3 (2003), pp. 515–26. DOI: 10.1002/mrm.10407 (cit. on p. 33).
- [6] Peter Schmitt *et al.* “Inversion recovery TrueFISP: quantification of T(1), T(2), and spin density.” In: *Magn. Reson. Med.* 51.4 (2004), pp. 661–7. DOI: 10.1002/mrm.20058 (cit. on p. 33).
- [7] Goetz H. Welsch *et al.* “Rapid estimation of cartilage T2 based on double echo at steady state (DESS) with 3 Tesla”. In: *Magn. Reson. Med.* 62.2 (2009), pp. 544–549. DOI: 10.1002/mrm.22036 (cit. on p. 33).
- [8] Oliver Bieri *et al.* “Quantitative mapping of T2 using partial spoiling”. In: *Magn. Reson. Med.* 66 (2011), pp. 410–418. DOI: 10.1002/mrm.22807 (cit. on p. 33).
- [9] K L Miller *et al.* “Steady-state diffusion-weighted imaging of in vivo knee cartilage”. In: *Magn Reson Med* 51.2 (2004), pp. 394–398. DOI: 10.1002/mrm.10696 (cit. on p. 33).
- [10] S C Deoni *et al.* “Quantitative diffusion imaging with steady-state free precession”. In: *Magn Reson Med* 51.2 (2004), pp. 428–433. DOI: 10.1002/mrm.10708 (cit. on p. 33).
- [11] O. Bieri *et al.* “Fast diffusion-weighted steady state free precession imaging of in vivo knee cartilage”. In: *Magn. Reson. Med.* 67 (2012), pp. 691–700. DOI: 10.1002/mrm.23061 (cit. on p. 33).
- [12] Oliver Bieri *et al.* “Quantitative in vivo diffusion imaging of cartilage using double echo steady-state free precession.” In: *Magn. Reson. Med.* 68.3 (2012), pp. 720–9. DOI: 10.1002/mrm.23275 (cit. on p. 33).
- [13] Ernesto Staroswiecki *et al.* “Simultaneous estimation of T₂ and apparent diffusion coefficient in human articular cartilage in vivo with a modified three-dimensional double echo steady state (DESS) sequence at 3 T”. In: *Magn. Reson. Med.* 67.4 (2012),

Chapter 2. Motion-Insensitive Rapid Configuration Relaxometry

- pp. 1086–1096. DOI: 10.1002/mrm.23090 (cit. on p. 33).
- [14] O Bieri *et al.* “Steady state free precession magnetization transfer imaging”. In: *Magn Reson Med* 60.5 (2008), pp. 1261–1266. DOI: 10.1002/mrm.21781 (cit. on p. 33).
- [15] M. Gloor *et al.* “Quantitative magnetization transfer imaging using balanced SSFP”. In: *Magn. Reson. Med.* 60.3 (2008), pp. 691–700. DOI: 10.1002/mrm.21705 (cit. on p. 33).
- [16] Monika Gloor *et al.* “Nonbalanced SSFP-based quantitative magnetization transfer imaging”. In: *Magn. Reson. Med.* 64 (2010), pp. 149–156. DOI: 10.1002/mrm.22331 (cit. on p. 33).
- [17] M. Markl *et al.* “Flow Effects in Balanced Steady State Free Precession Imaging”. In: *Magn. Reson. Med.* 50.5 (2003), pp. 892–903. DOI: 10.1002/mrm.10631 (cit. on p. 33).
- [18] Francesco Santini *et al.* “Time-resolved three-dimensional (3D) phase-contrast (PC) balanced steady-state free precession (bSSFP)”. In: *Magn. Reson. Med.* 62.4 (2009), pp. 966–974. DOI: 10.1002/mrm.22087 (cit. on p. 33).
- [19] Aurélien F. Stalder *et al.* “Quantitative 2D and 3D phase contrast MRI: Optimized analysis of blood flow and vessel wall parameters”. In: *Magn. Reson. Med.* 60.5 (2008), pp. 1218–1231. DOI: 10.1002/mrm.21778 (cit. on p. 33).
- [20] Wolfgang Hänicke *et al.* “An analytical solution for the SSFP signal in MRI”. In: *Magn. Reson. Med.* 49 (2003), pp. 771–775. DOI: 10.1002/mrm.10410 (cit. on p. 33).
- [21] Vasily L. Yarnykh. “Optimal radiofrequency and gradient spoiling for improved accuracy of T1 and B1 measurements using fast steady-state techniques”. In: *Magn. Reson. Med.* 63.6 (2010), pp. 1610–1626. DOI: 10.1002/mrm.22394 (cit. on p. 33).
- [22] Rahel Heule *et al.* “Variable flip angle T1 mapping in the human brain with reduced T2 sensitivity using fast radiofrequency-spoiled gradient echo imaging”. In: *Magn. Reson. Med.* 75.4 (2016), pp. 1413–1422. DOI: 10.1002/mrm.25668 (cit. on p. 33).
- [23] Sean C L Deoni *et al.* “High-resolution T1 and T2 mapping of the brain in a clinically acceptable time with DESPOT1 and DESPOT2”. In: *Magn. Reson. Med.* 53.1 (2005), pp. 237–241. DOI: 10.1002/mrm.20314 (cit. on p. 33).
- [24] Sean C L Deoni *et al.* “Rapid T2 estimation with phase-cycled variable nutation steady-state free precession”. In: *Magn. Reson. Med.* 52.2 (2004), pp. 435–439. DOI: 10.1002/mrm.20159 (cit. on p. 33).
- [25] R Heule *et al.* “Triple echo steady-state (TESS) relaxometry”. In: *Magn Reson Med* 71.1 (2014), pp. 230–237. DOI: 10.1002/mrm.24659 (cit. on pp. 33, 34, 36, 41).
- [26] Vladimir Juras *et al.* “A comparison of multi-echo spin-echo and triple-echo steady-state T2 mapping for in vivo evaluation of articular cartilage.” In: *Eur. Radiol.* (Sept. 2015). DOI: 10.1007/s00330-015-3979-6 (cit. on p. 33).
- [27] R Heule *et al.* “Triple-echo steady-state T2 relaxometry of the human brain at high to ultra-high fields”. In: *NMR Biomed* 27.9 (2014), pp. 1037–1045. DOI: 10.1002/nbm.3152 (cit. on pp. 33, 40).
- [28] Orso Pusterla *et al.* “T2-Snapshots imaging with simultaneous multislice TESS acquisition”. In: *Proc. 23rd Sci. Meet. Int. Soc. Magn. Reson. Med.* 2015, p. 1 (cit. on p. 33).
- [29] Damien Nguyen *et al.* “MIRACLE: Motion-Insensitive RAPid Configuration reLaxomEtry”. In: *Proc. 23rd Sci. Meet. Int. Soc. Magn. Reson. Med.* 2015, p. 1. URL: <http://cds.ismrm.org/protected/15MPresentations/abstracts/3238.pdf> (cit. on p. 33).
- [30] Carl Ganter. “Steady state of gradient echo sequences with radiofrequency phase cycling: Analytical solution, contrast enhancement with partial spoiling”. In: *Magn. Reson. Med.* 55.1 (2006), pp. 98–107. DOI: 10.1002/mrm.20736 (cit. on pp. 33, 34).

- [31] Y Zur *et al.* “Motion-insensitive, steady-state free precession imaging”. In: *Magn Reson Med* 16.3 (1990), pp. 444–459. DOI: 10.1002/mrm.1910160311 (cit. on pp. 34, 35, 39).
- [32] William H Press *et al.* *Numerical Recipes 3rd Edition: The Art of Scientific Computing*. 3rd ed. Cambridge University Press, 2007 (cit. on p. 36).
- [33] Elias Kellner *et al.* “Gibbs-ringing artifact removal based on local subvoxel-shifts”. In: *Magnetic Resonance in Medicine* 76.5 (2016), pp. 1574–1581. DOI: 10.1002/mrm.26054 (cit. on p. 36).
- [34] Josef Pfeuffer *et al.* “Anatomical and functional MR imaging in the macaque monkey using a vertical large-bore 7 Tesla setup”. In: *Magn. Reson. Imaging* 22.10 (2004), pp. 1343–1359. DOI: 10.1016/j.mri.2004.10.004 (cit. on p. 37).
- [35] F. Golub *et al.* “Estimation of spin-echo relaxation time”. In: *J. Magn. Reson.* 237 (2013), pp. 17–22. DOI: 10.1016/j.jmr.2013.09.006 (cit. on p. 37).
- [36] C Ganter *et al.* “B1+-mapping with the transient phase of unbalanced steady-state free precession”. In: *Magn Reson Med* 70.6 (2013), pp. 1515–1523. DOI: 10.1002/mrm.24598 (cit. on p. 38).
- [37] M Jenkinson *et al.* “A global optimisation method for robust affine registration of brain images”. In: *Med Image Anal* 5.2 (2001), pp. 143–156. DOI: 10.1016/S1361-8415(01)00036-6 (cit. on p. 38).
- [38] M Jenkinson *et al.* “FSL”. In: *Neuroimage* 62.2 (2012), pp. 782–790. DOI: 10.1016/j.neuroimage.2011.09.015 (cit. on p. 38).
- [39] Stefan Klein *et al.* “Elastix: A toolbox for intensity-based medical image registration”. In: *IEEE Trans. Med. Imaging* 29.1 (2010), pp. 196–205. DOI: 10.1109/TMI.2009.2035616 (cit. on p. 38).
- [40] Denis P Shamonin *et al.* “Fast parallel image registration on CPU and GPU for diagnostic classification of Alzheimer’s disease.” In: *Front. Neuroinform.* 7 (2013), p. 50. DOI: 10.3389/fninf.2013.00050 (cit. on p. 38).
- [41] Carl Ganter. “Static susceptibility effects in balanced SSFP sequences”. In: *Magn. Reson. Med.* 56.3 (2006), pp. 687–691. DOI: 10.1002/mrm.20986 (cit. on pp. 38, 40).
- [42] Nikola Stikov *et al.* “On the accuracy of T1 mapping: Searching for common ground”. In: *Magn. Reson. Med.* 522 (2014), pp. 514–522. DOI: 10.1002/mrm.25135 (cit. on p. 40).
- [43] T Ethofer *et al.* “Comparison of longitudinal metabolite relaxation times in different regions of the human brain at 1.5 and 3 Tesla”. In: *Magn Reson Med* 50.6 (2003), pp. 1296–1301. DOI: 10.1002/mrm.10640 (cit. on p. 40).
- [44] C. Preibisch *et al.* “Influence of RF spoiling on the stability and accuracy of T1 mapping based on spoiled FLASH with varying flip angles”. In: *Magn. Reson. Med.* 61.1 (2009), pp. 125–135. DOI: 10.1002/mrm.21776 (cit. on p. 40).
- [45] K L Miller. “Asymmetries of the balanced SSFP profile. Part I: theory and observation”. In: *Magn Reson Med* 63.2 (2010), pp. 385–395. DOI: 10.1002/mrm.22212 (cit. on p. 40).
- [46] K L Miller *et al.* “Asymmetries of the balanced SSFP profile. Part II: white matter”. In: *Magn Reson Med* 63.2 (2010), pp. 396–406. DOI: 10.1002/mrm.22249 (cit. on pp. 40–42).
- [47] Sean C L Deoni *et al.* “Gleaning Multicomponent T1 and T2 Information from Steady-State Imaging Data”. In: *Magn. Reson. Med.* 60.6 (2008), pp. 1372–1387. DOI: 10.1002/mrm.21704 (cit. on p. 41).
- [48] Eva Bengtsson Moström *et al.* “Pre- and postcontrast T1 and T2 mapping of patellar cartilage in young adults with recurrent patellar dislocation.” In: *Magn Reson Med* 74.5 (2015), pp. 1363–1369. DOI: 10.1002/mrm.25511 (cit. on p. 41).

Chapter 2. Motion-Insensitive Rapid Configuration Relaxometry

- [49] Fang Liu *et al.* “Rapid multicomponent T2 analysis of the articular cartilage of the human knee joint at 3.0T.” In: *J. Magn. Reson. Imaging* 39.5 (2014), pp. 1191–1197. DOI: 10.1002/jmri.24290 (cit. on p. 41).

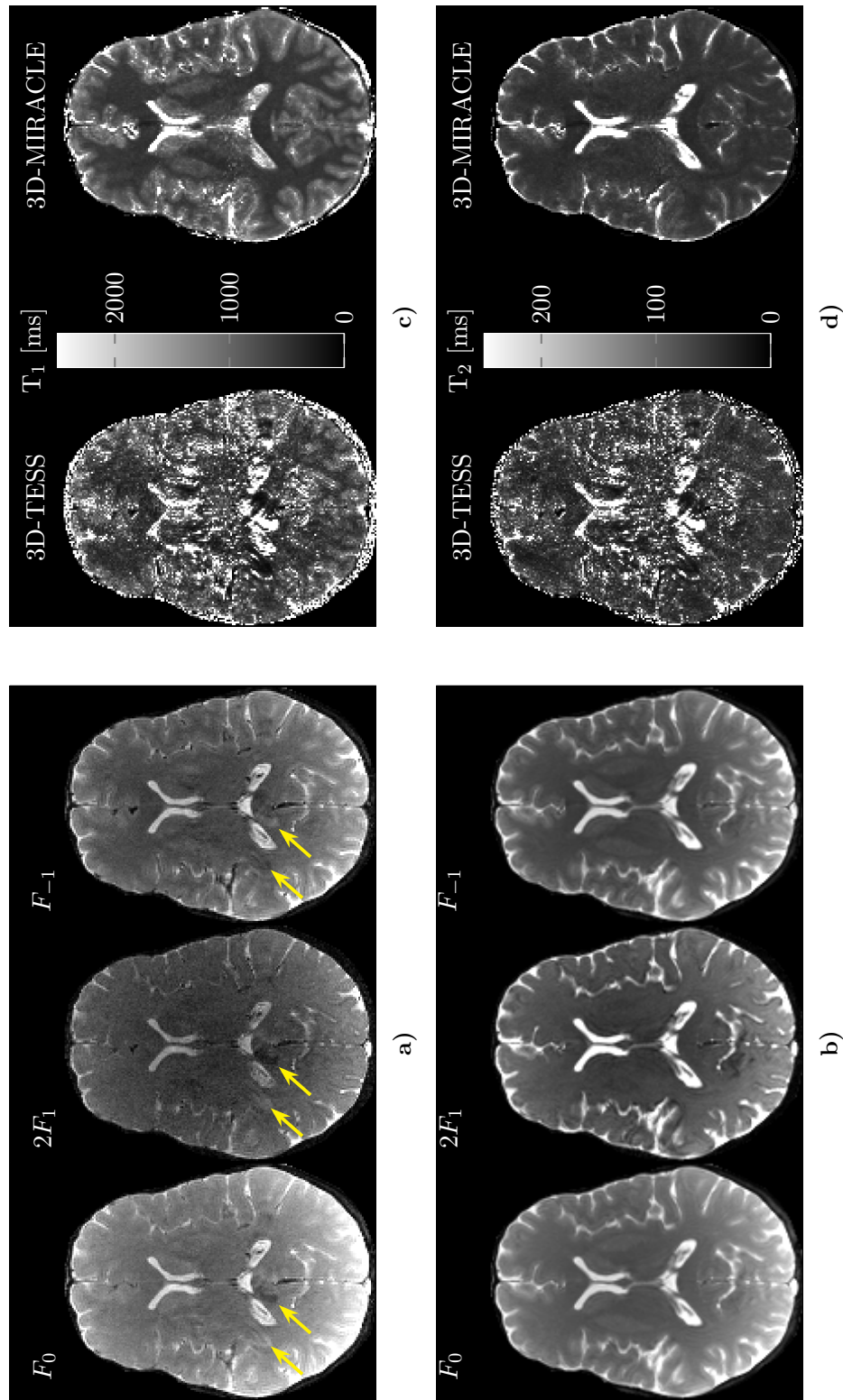


Figure 2.10 – Illustrative volumetric 3D-TESS and 3D-MIRACLE brain imaging of a healthy volunteer. **a** Axial sample images of the three lowest SSFP mode volumes F_1 , F_0 and F_{-1} acquired by TESS (note the different scaling for F_1). Arrows indicate the most pronounced pulsation artifacts. **b** Similar images derived from a MIRACLE acquisition. **c** Corresponding T_1 maps (ms) from TESS and MIRACLE. **d** Corresponding T_2 maps (ms) from TESS and MIRACLE (MIRACLE imaging parameters identical as Figure 2.6; TESS imaging parameters: resolution $1 \times 1 \times 2 \text{ mm}^3$, FA 15° , TR/TE = $5.93/3.03 \text{ ms}$, 2 avg.).

3 True Constructive Interference in the Steady State (trueCISS)

Tom Hilbert^{1,2,3,†}, Damien Nguyen^{4,5,†}, Jean-Philippe Thiran^{2,3}, Gunnar Krueger^{2,3,6},
Tobias Kober^{1,2,3} and Oliver Bieri^{4,5}

¹Advanced Clinical Imaging Technology (HC CEMEA SUI DI PI), Siemens Healthcare AG, Lausanne, Switzerland

²LTS5, École Polytechnique Fédérale de Lausanne, Lausanne, Switzerland

³Department of Radiology, University Hospital (CHUV), Lausanne, Switzerland

⁴Division of Radiological Physics, Department of Radiology, University Hospital Basel, University of Basel, Basel, Switzerland

⁵Department of Biomedical Engineering, University of Basel, Basel, Switzerland

⁶Siemens Medical Solutions USA, Boston, MA, USA

† equally contributing authors

3.1 Introduction

In the last decades, the use of steady-state free precession (SSFP) sequences has rapidly increased. Among the different variants first introduced by Carr [1] in 1958 for NMR spectroscopy, balanced SSFP (bSSFP) in particular offers the highest signal-to-noise ratio (SNR) per unit of time among all MRI sequences [2]. However, bSSFP imaging is prone to field inhomogeneities [1, 3] that may lead to signal voids; these appear as dark bands in the image and thus frequently are referred to as *banding* artefacts.

Commonly, banding is addressed by a series of multiple bSSFP acquisitions with different radiofrequency (RF) phase-cycling schemes, in combination with a suitable reconstruction method, such as maximum-intensity projection (MIP) [3], complex sum (CS) [4], sum-of-squares (SOS) and magnitude sum (MS) [5], or some other [6]. The most common approach, termed *constructive interference in the steady state* (CISS), acquires only two phase-cycles and combines them with a maximum-intensity projection, offering a good tradeoff between acquisition time and banding artifact reduction. A major drawback of these image-based combinations is that the derived pixel intensity no longer reflects the genuine, i.e. on-resonant, bSSFP signal magnitude typically presumed for quantification techniques based on bSSFP sequences. For low flip angle bSSFP acquisitions, these methods tend to modify the intrinsic bSSFP signal (see Figs. 3.1c and 3.1d), which can impede the radiological assessment because clinicians usually are more familiar with the on-resonant, that is, genuine, bSSFP contrast.

An introductory example of this behavior is presented in Fig. 3.1, showing the signal behavior and contrast difference (to the on-resonant signal) for various multiple-acquisition techniques based on the bSSFP magnetization derived with the Freeman-Hill formula [7] ($T_1/T_2 = 870/70$ ms, repetition time (TR) = 5 ms and off-resonances between 0° and 360°) for a flip angle of 15° (Figs. 3.1a and 3.1c) and for a flip angle of 50° (Figs. 3.1b and 3.1d). Generally, the combined signal and thus the contrast, as generated with the various reconstruction methods, deviates from the genuine bSSFP signal properties and strongly

depends on the flip angle as well as on the tissue properties. Typically, the prominent T_1/T_2 image contrast, as commonly associated with bSSFP, only can be achieved over the complete frequency spectrum in the limit of a 90° flip angle [7]. Furthermore, most of the multiple-acquisition combination techniques assume that the steady-state signal resembles a plateau within the passband region, that is, for off-resonances within $\pm 1/(3\text{TR})$ for phase-cycled bSSFP, which only is true in the high flip angle regime. This may pose considerable problems due to specific absorption rate (SAR) limitations; especially at higher field strengths.

Consequently, it is much more advantageous to use parameter estimation techniques to derive bSSFP artifact-free images from a signal model coupled with an optimization algorithm [8–11]. To the best of our knowledge, the most recent work was reported by Björk *et al.* [9] where the Freeman-Hill formula [7] was fitted onto four phase-cycled bSSFP images using a linearised signal model in combination with linear least-square fitting followed by a Gauss-Newton nonlinear search (LORE-GN).

Generally, parameter estimation techniques require multiple phase-cycled acquisitions to provide a well-conditioned framework for the fitting procedure. Obviously, this leads to longer acquisition times compared to a conventional CISS acquisition requiring only two phase cycles. In this regard, the acceleration of exhaustive data scans using compressed sensing techniques has become more and more practicable, overall providing high acceleration factors [12] – especially for applications that have additional dimensions, such as the time-domain in cardio-vascular imaging [13]. Briefly, it is assumed that if the information encoded in an image is compressible, then the acquisition can be accelerated by sampling the data in a compressed manner. The acquisition of multiple phase cycles within the CISS sequence reflects such an additional dimension with redundant information, allowing high acceleration factors as already demonstrated by Cukur [14] and Ilicak *et al.* [15].

In this article, we propose to use a compressed sensing reconstruction in combination with a dictionary-based parameter estimation technique

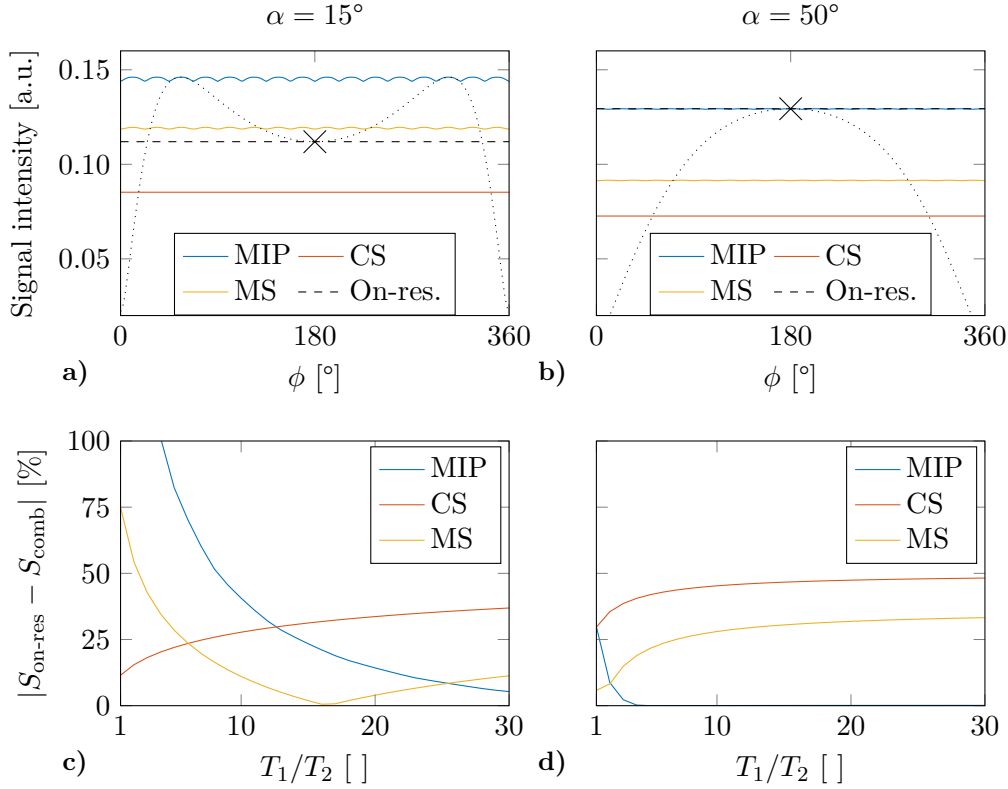


Figure 3.1 – MIP, CS, and MS reconstruction of 16 phase-cycled complex bSSFP profiles for $T_1/T_2 = 870/70$ ms, repetition time = 5 ms, for a flip angle of 15° (a) and for a flip angle of 50° (b). For completeness, a single bSSFP frequency response profile also is shown, indicating the on-resonant signal amplitude (X). Relative deviation between the on-resonant bSSFP signal amplitude and the average combined signal intensity for the various methods for a low flip angle 15° (c) and a high flip angle (d). Note how the contrast between tissues is more dependent on their relaxation time properties in the low flip angle regime. bSSFP, balanced steady-state free precession; CS, complex sum; MIP, maximum intensity projection; MS, magnitude sum; T_1 longitudinal relaxation time; T_2 transverse relaxation time; TR, repetition time; on-res, on-resonant; comb, combined.

to retrieve the genuine bSSFP signal (i.e., independent from a multiple-acquisition combination technique and used flip angle) from a set of highly undersampled bSSFP scans with different phase-cycling schemes. The estimated parameters are then used to reconstruct artifact-free images with a pixel intensity that reflects the true, on-resonant, bSSFP signal amplitude. Due to the high undersampling, this results in scan times comparable to conventional CISS imaging. In addition, because all relevant parameters (i.e. M_0 and T_1/T_2) are known, synthetic bSSFP contrast images can be derived from these data, which are not directly measurable in practice.

3.2 Methods

Acquisition

A conventional bSSFP sequence was modified to acquire within a single scan a set of N acquisitions with constant, but distinct, RF phase increments (φ_j). Throughout this work, we only consider the simplest scheme of equidistantly distributed RF phase increments:

$$\varphi_j \triangleq \frac{2\pi}{N}(j-1) \quad \forall j \in \mathbb{N}^* \wedge j < N \quad (3.1)$$

A schematic representation of the acquisition scheme can be found in Fig. 3.2a.

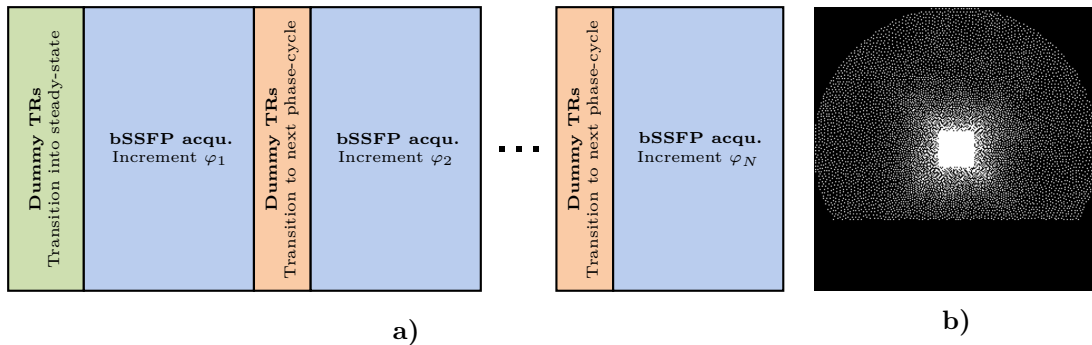


Figure 3.2 – Diagram of a true constructive interference in the steady state acquisition in which each blue block represents an undersampled 3D bSSFP acquisition with different RF phase-cycling scheme (RF phase increment). Initially, some dummy TRs (green block) are played out to allow transition into steady state. In between the bSSFP acquisitions, a fixed number of dummy TRs (red blocks) are played out with linearly increasing RF phase increments (from φ_j to φ_{j+1}) to mitigate transient effects (a). Exemplary k-space sampling pattern for a scan with a phase encoding matrix size of 320×320 . White pixels indicate sampled k-space locations, whereas black pixels show ignored k-space points (b). bSSFP, balanced steady-state free precession; RF, radiofrequency; TR, repetition time.

To shorten the overall scan time, a highly undersampled pseudo-random phase encoding scheme, based on a variable-density Poisson disk distribution [16–18], was implemented to generate an incoherent sampling pattern for each phase-cycle. Additionally, elliptical scanning, that is, skipping of k-space samples at the edges of k-space [19], and partial Fourier, that is, omitting parts of k-space by allowing the compressed sensing algorithm to intrinsically exploit its complex-conjugate symmetry (see chapter 13.7 in [20]) are applied to further reduce scan time. A fully sampled reference region in the center of k-space is acquired for every phase-cycled scan to estimate the coil sensitivities used during reconstruction [21]. An exemplary sampling pattern for a single acquisition is shown in Fig. 3.2b.

Initially, a number (typically 200-300, about 2 s) of dummy TRs, that is, without data acquisition, are played out for the transition from equilibrium

magnetization to the steady-state (see also sequence diagram in Fig. 3.2a). Similarly, a constant number of dummy TRs (typically 40) with linearly increasing RF phase increments (from φ_j to φ_{j+1}) are played out in between individual acquisitions of the different phase cycles to smooth and enhance the signal transition between the steady states.

Reconstruction

We consider a train of RF pulses with a constant flip angle, α , and a constant RF phase increment, φ , in combination with balanced gradient moments. As commonly done, finite RF pulse effects as well as magnetization transfer (MT) and diffusion effects are neglected. In the limit of a TR much smaller than the transverse (T_2) and longitudinal (T_1) relaxation times, the complex bSSFP signal is approximatively given by (see also [22])

$$M(\alpha, \varphi_j, \phi, \Lambda) \approx M_0 \frac{2 \left| \cos\left(\frac{\phi - \varphi_j}{2}\right) \sin \alpha \right|}{1 + \cos \alpha + 2 \cos(\phi - \varphi_j) + (4\Lambda - 2 \cos(\phi - \varphi_j) \sin^2\left(\frac{\alpha}{2}\right))} e^{-i\phi/2} \quad (3.2)$$

Chapter 3. True Constructive Interference in the Steady State (trueCISS)

In Eq. (3.2), M_0 denotes the equilibrium magnetization; $\Lambda \triangleq T_1/T_2$ refers to the relaxation time ratio; φ_j refers to the RF pulse phase increment (see also Eq. (3.1)); and ϕ to the local phase offset due to field inhomogeneities.

TrueCISS images are reconstructed as outlined below. In short,

1. A compressed sensing reconstruction is used to recover all missing samples from the incoherent undersampled acquisition scheme. This results in a series of fully sampled bSSFP images featuring different RF phase increments φ_j ;
2. From the signal model (see also Eq. (3.2)), the three parameters (M_0 , Λ and ϕ) are estimated using a dictionary-based fitting algorithm;
3. An on-resonant bSSFP signal image, termed *trueCISS*, is derived from the parameter maps.

The compressed sensing reconstruction of the undersampled bSSFP data combines a Fourier transformation (FT) across the φ -dimension and a wavelet transformation (Ψ) in the spatial domain [12, 23, 24] as sparse regularisation. The first of the sparsifying transform relies on the inherent periodic nature of the bSSFP signal along the phase-cycle dimension. Because of that property, the bSSFP profile can be expressed as a Fourier series [25] with rapidly decaying Fourier coefficient amplitudes, thus providing a sparse representation. This result can also be derived rigorously using the Fourier representation of the SSFP signal, also known as SSFP configuration theory [26]. The following cost function was used for the optimization problem:

$$L(Y_c, \lambda) = \frac{1}{2} \sum_c \|PFT\{C_c X\} - Y_c\|^2 + \lambda |\Psi_{xy}\{FT_\varphi\{X\}\}| \quad (3.3)$$

where the first term ensures consistency between measured and estimated data, and the second term enforces sparsity. In Eq. (3.3), X refers to the estimated fully-sampled bSSFP image series, C_c to the complex coil sensitivities, Y_c to the

measured undersampled k-space data, P to the sampling pattern represented as a binary mask and λ is a regularisation parameter. The cost function is minimized using the split algorithm proposed in [27] which provides better conditioning of the optimization problem and thus results in faster convergence as compared to conventional techniques. Calculation of the complex coil sensitivities was performed in two steps: the first order SSFP echo image was estimated using a Fourier analysis of the fully sampled k-space centers [28], then the coil sensitivities were computed using an eigenvalue-based estimation [21] on the previously obtained image.

After the compressed-sensing reconstruction, a dictionary-based algorithm is used to yield voxel-wise estimates for M_0 , Λ , and ϕ from Eq. (3.2), because Eq. (3.2) has multiple local minima and is not differentiable at $\varphi - \phi = \{\frac{1}{2}\phi, \frac{3}{2}\pi\}$. In contrast to conventional optimization algorithms, such as gradient descent methods, dictionary-based fitting only requires knowledge of the forward signal model. To that end, a dictionary of signals with $\Lambda = \{1, 1.1, 1.2, \dots, 30\}$ and $\phi = \{0^\circ, 5^\circ, 10^\circ, \dots, 355^\circ\}$ is generated from Eq. (3.2) for $M_0 = 1$ and the actual imaging parameters that were used to acquire the data (i.e. φ_j and α). This allows the comparison of the acquired signal in each voxel to the simulated signals in the dictionary using the squared norm (L_2 -norm) of the difference as a distance metric. The dictionary entry with the smallest distance to the measured data is considered the best least-squares approximation of the acquired signal. Its corresponding Λ and ϕ values are then attributed to the voxel. Because M_0 is fixed during the training of the dictionary, the simulated and acquired signals need to be normalized to account for variations in M_0 before the comparison. To that end, scaling factors are calculated with $s_{sim} = \|M_{acq}\|^{-1}$ for the simulated signal in the dictionary and $s_{acq} = \|M_{acq}\|^{-1}$ for the actual acquired signal, in which M_{sim} and M_{acq} denote the discrete signals, respectively. The equilibrium magnetization is then estimated using these scaling factors with $M_0 = s_{sim}/s_{acq}$.

Finally, genuine on-resonant bSSFP images, termed *true constructive interference in the steady*

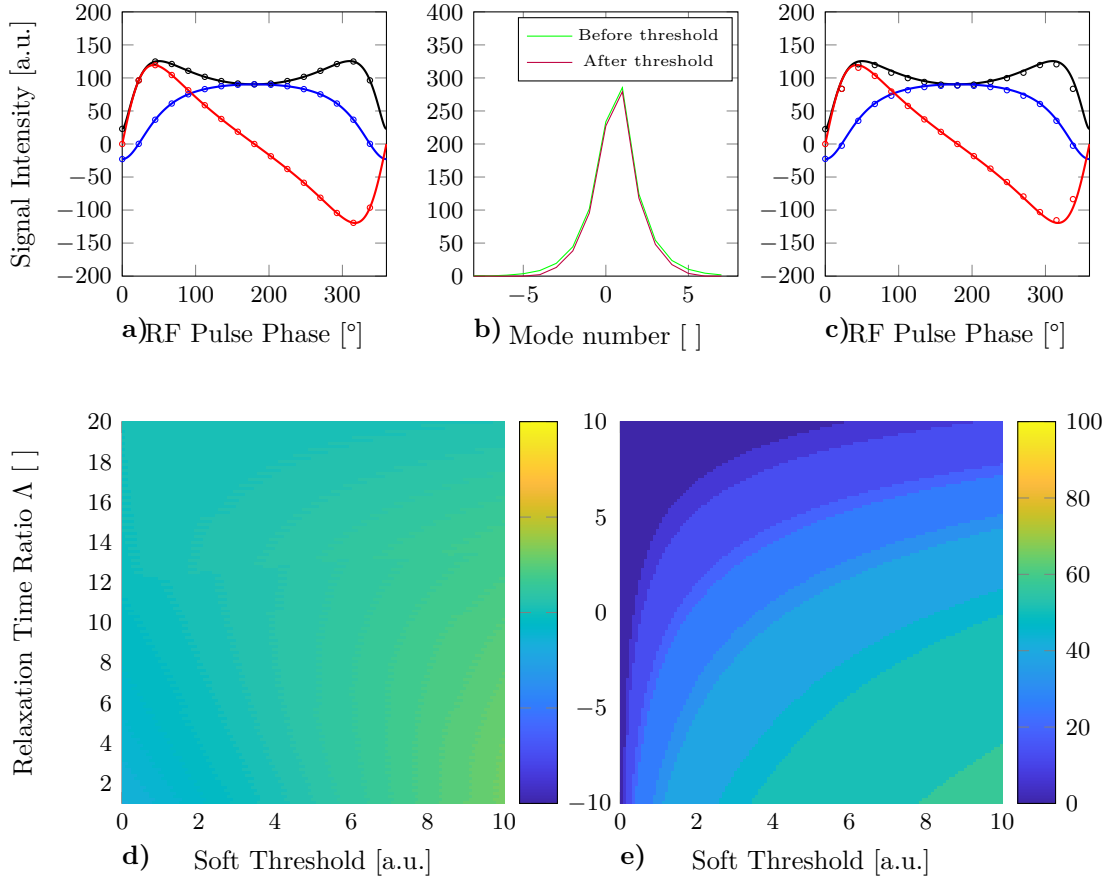


Figure 3.3 – Simulated complex bSSFP profile with $\Lambda = 10.4$ (a, continuous lines) and with black indicating the magnitude, blue indicating the real values, red indicating the imaginary values, and circles indicating the sampled phase cycles. Its discretized signal was Fourier-transformed into configuration space (b, green). The configuration space has six zero coefficients (37.5%) after applying a low softthreshold of 6 (b, purple). The inverse Fourier transform of the signal after applying the threshold diverges from the original (c, circles), causing an overestimation in the dictionary fitting ($\Lambda^* = 11.6$). (d) Bias of Λ and (e) amount of zero coefficients for all combinations of Λ and soft thresholds. bSSFP, balanced steady-state free precession; RF, radiofrequency.

state (trueCISS), are reconstructed from Eq. (3.2) in the limit of $\varphi - \phi \rightarrow 0$, in combination with the estimated M_0 and Λ parameter maps. Moreover, synthetic image contrasts, such as images featuring a different flip angle than the measured one, can be derived. It is also possible to adjust the flip angle independently for each voxel in order to locally maximize the bSSFP signal, termed *maxCISS*, using [20]:

$$M_{\max}|_{\theta=\theta_{\text{opt}}} \approx \frac{1}{2} M_0 \Lambda^{-1/2} \quad (3.4)$$

where $\theta_{\text{opt}} \approx \cos^{-1} \left(\frac{\Lambda-1}{\Lambda+1} \right)$.

Simulations and Imaging

All numerical simulations, data analysis and visualizations were performed using MATLAB 8.5 (MathWorks, Natick MA). Measurements and calibrations were performed on a clinical 3 T whole-body system (Magnetom Prisma, Siemens, Erlangen, Germany) with actively shielded magnetic field gradient coils using a commercially available 20-channel head coil. Prior to scanning, informed written consent was obtained from each volunteer taking part in this study.

Similar to every other compressed sensing regularization, the zeroing of coefficients in the sparse domain can introduce undesirable

Chapter 3. True Constructive Interference in the Steady State (trueCISS)

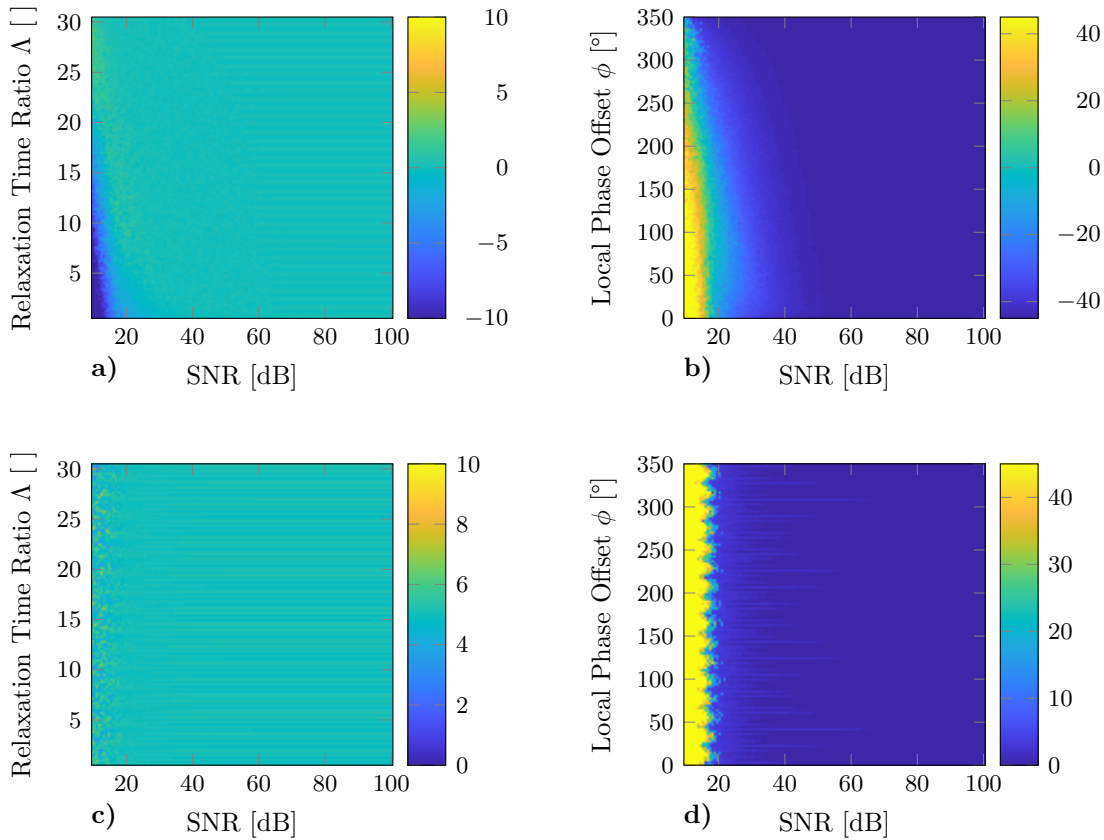


Figure 3.4 – (a) Mean error of Λ depending on the SNR with $\phi = 180^\circ$ and (c) the standard deviation of the Λ error. (b) Mean error of ϕ depending on the SNR with $\Lambda = 10$ and (d) the standard deviation of the ϕ error. SNR, signal-to-noise ratio.

reconstruction artifacts that subsequently could bias the estimation of Λ . To study the impact of the regularization, a set of complex bSSFP profiles were simulated, with L ranging from 1 to 20; $\phi = 180^\circ$; and $M_0 = 1$. To deliberately introduce regularization artifacts, all the profiles were Fourier-transformed into configuration space, and a range of soft thresholds (1-8) were applied to achieve zero coefficients, that is, sparsity. Subsequently, the signal was inverse Fourier-transformed back to a bSSFP profile and compared to the simulated ground truth. Subsequently, the previously described dictionary fitting was performed on the obtained profiles to evaluate the impact of the introduced regularization artifacts on the estimation of Λ .

Dictionary-based fitting algorithms became more popular in recent years and proved to be powerful tools, for example, in MR fingerprinting

applications [29]. Applying it to a bSSFP sequence only requires a simple adaption of the method. However, the sequence design and signal properties are different and the dictionary fitting may behave in another manner, requiring a thorough analysis to avoid systematic biases and ensure accuracy. To that end, an additional experiment was performed, simulating bSSFP profiles with different relaxation time ratios Λ (1-30) for a fixed flip angle (15°) and a fixed local phase offset ($\phi = 180^\circ$) in the presence of white Gaussian noise at different SNR levels (5-100). The dictionary fitting was used to estimate the relaxation time ratio, and its deviation from the known truth was calculated. This was repeated 128 times to calculate two fitting quality measures: the mean error and the standard deviation (SD) of the error. A similar experiment was then performed using a range of local phase offsets (8° - 360°) and a fixed relaxation time ratio

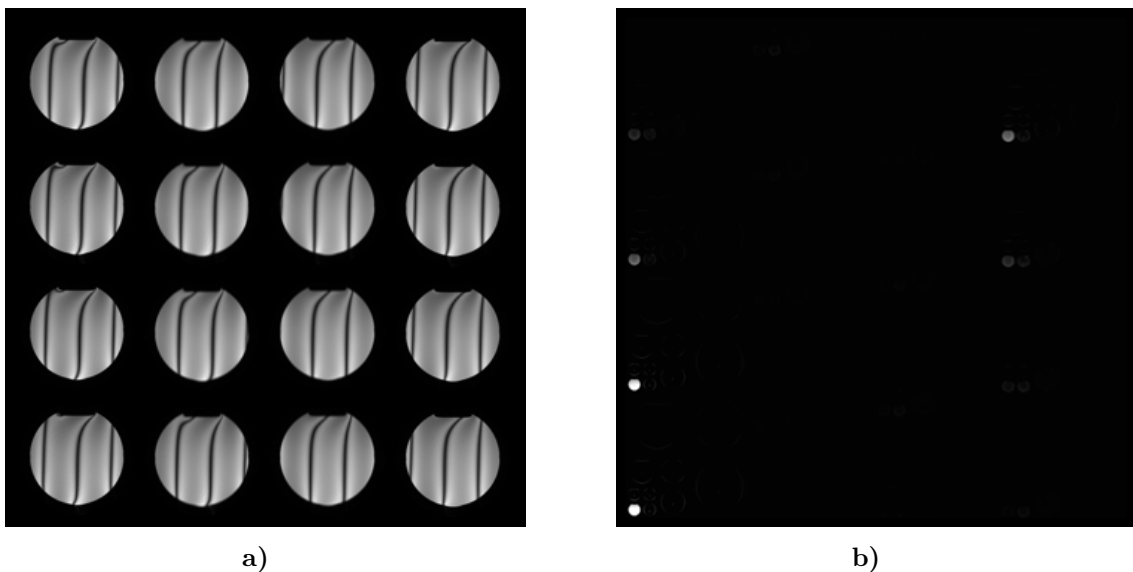


Figure 3.5 – (a) Illustrative images from a set of $N = 16$ bSSFP scans with different RF phase increments (cf. Eq. (3.1)), and (b) corresponding sparse representation by subsequently applying a Fourier transformation along the phase cycles and a spatial wavelet-transformation.

($\Lambda = 10$).

Phantom imaging was performed on a manganese-doped spherical phantom composed of 0.125 mM MnCl_2 dissolved in water (with T_1/T_2 -ratio of 870/70 ms ~ 12 , similar to human tissues, as measured by gold standard T_1 and T_2 relaxometry methods) and about 14 cm in diameter. TrueCISS imaging was performed with 16 phase cycles using an eightfold undersampled k-space in combination with a TR/echo time (TE) of 4.48/2.24 ms, a flip angle α of 15° , a resolution of $1 \times 1 \times 1 \text{ mm}^3$ ($192 \times 192 \times 192$ matrix size), a bandwidth of 501 Hz/px, and RF phase increments φ_j according to Eq. (3.1), yielding an overall scan time of 5:56 min. During the acquisition, a linear frequency offset gradient was applied over the whole field of view to induce multiple banding artifacts within the image. A reference CISS image was acquired with the same resolution, bandwidth and flip angle using an unmodified product sequence with a TR/TE of 7.13/3.31 ms; yielding a comparable total acquisition time of 5:31 min.

One *in vivo* 3D human whole-brain trueCISS dataset was acquired using the same prototype sequence with 16-phase cycles and eightfold undersampling in combination with a TR/TE of

6.36/3.18 ms, $\alpha = 15^\circ$, $1 \times 1 \times 1 \text{ mm}^3$ resolution ($256 \times 256 \times 176$ matrix size), bandwidth 250 Hz/px and RF phase increments φ_j following Eq. (3.1), resulting in a total scan time of about 10:15 min. For comparison, a 3D CISS image dataset was also acquired with the same resolution, but having a TR/TE of 7.87/3.59 ms, $\alpha = 50^\circ$, bandwidth 337 Hz/px, completed within 9:4 min. Contrary to the phantom experiment, different sequence parameters were used for the CISS acquisition because parameters as used for trueCISS would have led to significant banding residuals and would not be used in clinical routine.

3.3 Results

To demonstrate the effects of regularization artifacts, the 16 phase-cycling samples of an exemplary simulated complex bSSFP profile ($\Lambda = 10.4$) are shown in Fig. 3.3a. Its shape in the configuration space is shown in Fig. 3.3b (green). After a moderate soft threshold ($=6$) was applied (Fig. 3.3b, purple), 37.5% of the coefficients in the configuration space are zero, indicating that the Fourier transform achieves a sufficient sparsity. The regularization artifacts induced by the soft

Chapter 3. True Constructive Interference in the Steady State (trueCISS)

threshold only have a small impact on the shape of the bSSFP profile (Fig. 3.3c, circles) and lead to a slight overestimation ($\Lambda^* = 11.6$). The obtained sparsity and introduced error in Λ for the simulated range of Λ and soft thresholds are shown in Figs. 3.3d and 3.3e. To summarise these results, with higher Λ , more zero coefficients can be achieved after Fourier transformation and soft-thresholding due to its higher sparsity. However, the dictionary fitting overestimates Λ , with stronger regularization artifacts, especially when Λ is high.

The mean and SD of the error in the dictionary fitting are shown in Fig. 3.4. The simulations with a high SNR (> 30) show a very low bias and a good accuracy of the parameter estimation. A small step-wise error is visible due to the restriction of the dictionary fitting to a discrete set of solutions. The estimation of lower Λ appears to be more accurate than for higher values, which could be due to the more distinctive shape of a low Λ at low flip angle (15°), allowing for good estimates even for a bad SNR (~ 10). On the other hand, the accuracy of the ϕ error is rather independent from the actual ϕ value and remains high without bias until it drops drastically (e.g. at SNR = 15 with $\Lambda = 10$).

Illustrative axial images from the 16 highly undersampled phase-cycled bSSFP manganese-doped spherical phantom datasets (with RF phase increments following Eq. (3.1)) are shown in Fig. 3.5a after the proposed compressed sensing reconstruction. Note that a linear frequency gradient was applied from left to right to artificially induce banding artifacts. The required sparsity after the proposed wavelet and Fourier transformation becomes evident by the low number of non-zeros coefficients present in the transformed image (Fig. 3.5b).

Corresponding trueCISS parameter maps are given in Figs. 3.6a–3.6c in axial orientation. Generally, because transmit field inhomogeneities (B_1) are not accounted for, the Λ map reflects the expected B_1 -related smooth variation from the center towards the rim of the phantom. Residual small-scale variations, however, which appear to be rather related to the superimposed B_0 field

inhomogeneity, can be perceived on both Λ and M_0 parameter maps, but become less intense in the final trueCISS image (Fig. 3.6d) and have a magnitude smaller than truncation artifacts as can be seen in the intensity profile. For reference, a 15° CISS image is shown in Fig. 3.6e using an unmodified product sequence. Banding-related residual signal modulations become accentuated in the conventional CISS image, because of the low flip angle scan.

Exemplary parameter maps estimated from the high-resolution *in vivo* 3D whole-brain trueCISS acquisition are given in Fig. 3.7 in sagittal orientation. As can be expected and reflected by the field map (Fig. 3.7c), severe field inhomogeneities towards the neck, cavities, and outer parts of the brain tissue emanate due to the rather long TR used for the bSSFP acquisition at 3 T. Overall, the parametric maps of M_0 and Λ exhibit the expected contrast between white and grey matter resulting from differences in proton densities and relaxation times. As for the phantom, some residual B_1 -bias can be perceived in Λ ; however it appears less pronounced.

TrueCISS image reconstructions with flip angles of 15° (native) and 50° (synthetic), as well as a maxCISS image reconstruction (see also Eq. (3.4)) are shown in Fig. 3.8. For comparison, a standard 50° flip angle CISS image is also shown (Fig. 3.8d). Compared to the standard CISS sequence, all trueCISS images achieve a greater suppression of banding artefacts, most noticeable in regions suffering from strong field inhomogeneities, such as the region superior to the nasal cavity. The trueCISS image with a native flip angle of 15° (Fig. 3.8a) provides a good contrast between white and grey matter, whereas the maxCISS with the optimal flip angle in each voxel (Fig. 3.8b) provides the highest signal intensities throughout and a better contrast in deep grey matter structures. The synthetic trueCISS image derived for a flip angle of 50° (Fig. 3.8c) provides a similar contrast as the conventional CISS sequence (Fig. 3.8d), but suffers from slight blurring as can be seen in the thalamus region. Furthermore, in comparison to the conventional CISS, small vessels are not visible.

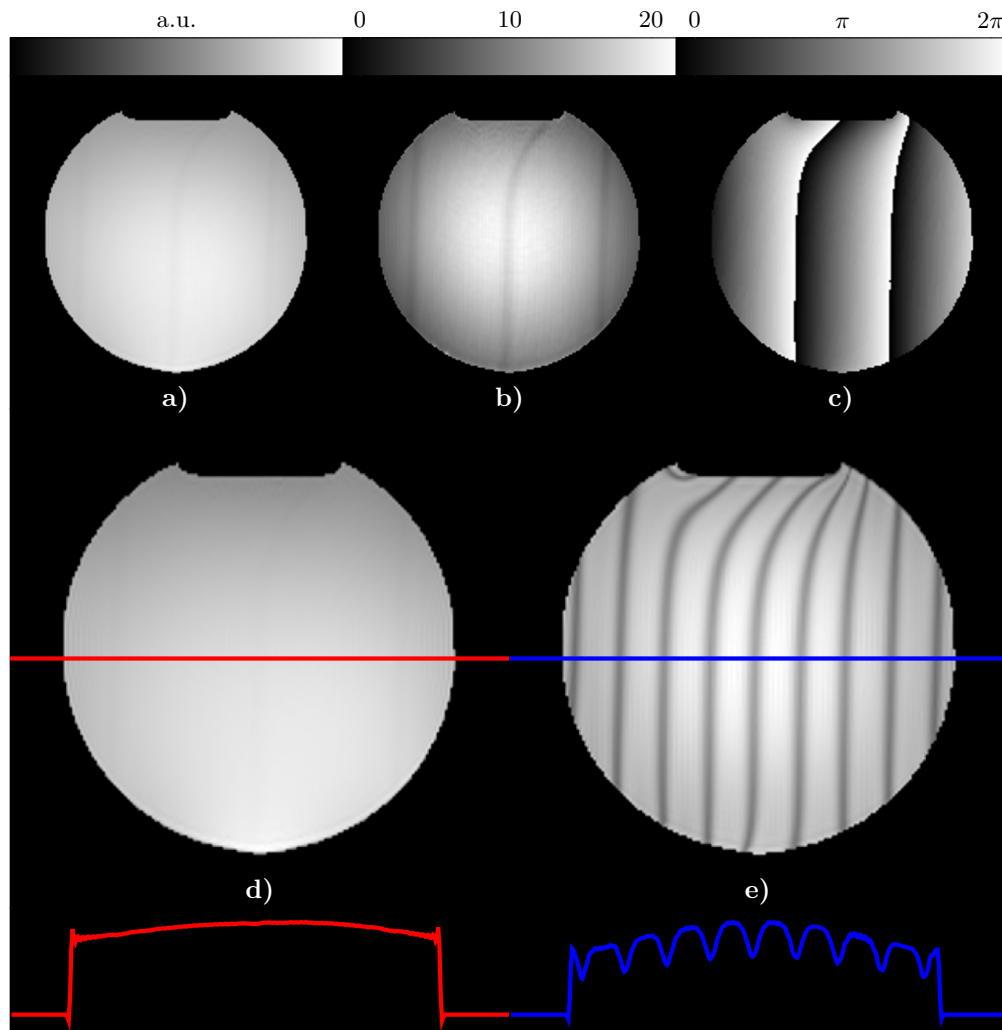


Figure 3.6 – Parametric maps obtained from a dictionary based fitting of phase-cycled bSSFP datasets and correspond to the initial magnetization M_0 (a), the relaxation time ratio Λ (b) and the local phase offset $\Delta\phi$ (c). Phantom images reconstructed based on the proposed TrueCISS method, with an intensity profile in red, (d) and from a conventional CISS acquisition, with an intensity profile in cyan (e). Both acquisitions were performed with a flip-angle of 15° and a linear frequency offset gradient (top to bottom) to generate banding artifacts.

Chapter 3. True Constructive Interference in the Steady State (trueCISS)

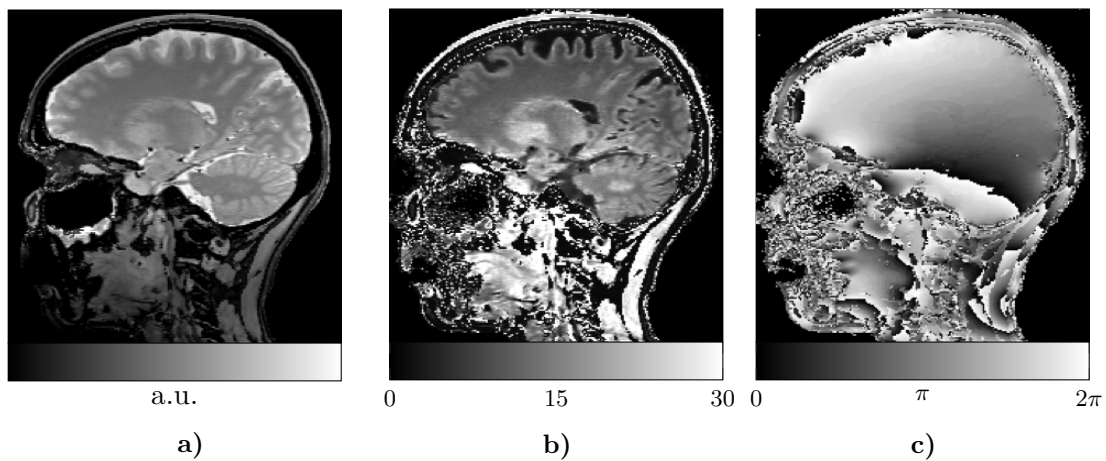


Figure 3.7 – Parametric maps obtained by the dictionary based fitting and that correspond to the initial magnetization M_0 (a), relaxation time ratio Λ (b) and local phase offset $\Delta\phi$ (c).

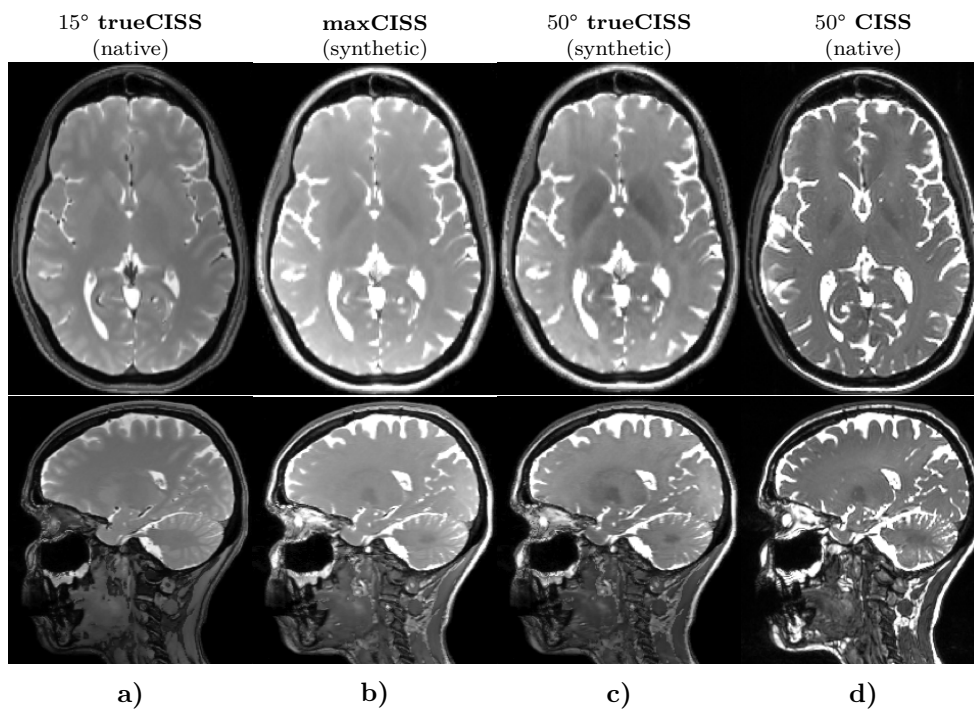


Figure 3.8 – Axial and sagittal slices of trueCISS images with the native flip-angle of 15° (a), maxCISS with the optimal flip-angle (b) and a flip-angle of 50° (c) compared to the conventional CISS image (d). Note that the subject slightly moved between the trueCISS and CISS acquisition. The arrow points to residual banding artifacts that can be seen on the CISS image. CISS, constructive interference in the steady state; maxCISS, synthetic contrast with optimal flip angle per voxel.

3.4 Discussion

The results demonstrate that banding-free images can be reconstructed from a set of highly undersampled phase-cycled bSSFP acquisitions using compressed sensing in combination with a dictionary-based estimation of the intrinsic bSSFP signal-dominating parameters. This combination allows for better image quality, with overall scan times comparable to conventional 3D CISS imaging.

TrueCISS imaging provides the true, that is, on-resonant, bSSFP signal amplitude, thus facilitating the use of quantitative imaging methods that rely on accurate bSSFP signal estimation. Moreover, high flip angle trueCISS images can be synthesized from low flip angle bSSFP data to enhance its prominent fluid-tissue contrast. Generally, low flip angle bSSFP imaging is advantageous because it not only mitigates MT effects [30], but also allows scanning with low SAR. Consequently, synthetic trueCISS imaging may represent a valuable alternative if SAR-intensive sequences like CISS and SPACE or conventional bSSFP protocols fail due to safety constraints. This is especially interesting at ultra-high field strengths, where the application of SAR-intense sequences is challenging.

The synthetic contrast, as provided by maxCISS, reflects the maximum bSSFP signal intensities in each voxel for the underlying tissue properties (i.e. T_1/T_2). This contrast is not only impossible to acquire in practice, but it also renders the maxCISS signal independent of the transmit field inhomogeneity (B_1^+). Thus, the proposed maxCISS image contrast might be of particular interest in clinical applications where a strong B_1 variation is expected or the images contain many different types of tissues and the tuning for a reasonable flip-angle is challenging (e.g. knee, abdomen).

The noise behavior in the image should be considered when generating synthetic contrasts from the parameter maps that divert from the original sequence protocol (e.g., different flip angle). The synthesis may result in heterogeneous noise amplifications or reduction because the signal intensity scales nonlinearly, depending on the underlying contrast parameters

(i.e., M_0 , T_1/T_2 , and flip angle).

The steady-state magnetization image should be proton-density-weighted and therefore exhibit poor contrast between white and grey matter. However, we observe a greater contrast than expected, which may be due to an asymmetry of the bSSFP profile in some locations not accounted for in the signal model. These asymmetries were more closely studied in [31] and may be the reason for the subtle B_0 effects in the phantom experiment. Other physical effects, which are neglected in the model, contribute to the estimate of M_0 as well. Therefore, we consider M_0 is not a quantitative estimation of proton density; rather, it serves as a parameter used to accommodate multiple physical effects.

A limitation of the proposed method arises from the spatial regularization used in the compressed sensing reconstruction and the partial Fourier sampling of k-space that introduce blurring in the resulting images. Furthermore, simulations demonstrate that the sparsity that can be achieved with the Fourier transform across phase cycles greatly depends on T_1/T_2 and flip angle because lower T_1/T_2 and lower flip angles result in sharper transitions in the bSSFP profile. Additionally, the sparsity will depend on the amount of acquired phase cycles because data tend to become sparser as the dimensionality of the observation matrix increases. These limitations of the regularization should be taken into account when optimizing sequence protocols, because they may prohibit high acceleration factors and cause regularization artifacts, resulting in an overestimation of Λ during the dictionary fitting. Generally, more advanced regularization techniques, such as joint total variation along the phase cycles [32] could be used to further mitigate residual blurring. Another possibility to reduce blurring is to acquire fewer phase cycles and use the gained time to sample more k-space samples for each phase cycle. However, this may lead to an ill-posed fitting of the tissue parameters after the compressed sensing reconstruction.

Another source of error in the reconstruction is the accuracy of the coil-sensitivities used in the compressed sensing algorithm. The accuracy of the coil-sensitivity estimate can be flawed if the field-of-view of the acquisition is too small and

folding artifacts appear. This is a common problem in compressed sensing reconstructions and thus affects the quality of the resulting trueCISS images.

Moreover, the model-fitting procedure might introduce errors in the obtained images. Its overall accuracy depends on the ability to correctly estimate the bSSFP signal parameters in each voxel. Any nonmodelled difference due to hardware-related inconsistencies or physiological processes will result in biased estimates of M_0 , Λ and ϕ , which are visible as a suboptimal banding artifact removal in the final images. For example, severe intra-voxel susceptibility gradients could lead to a local transition of balanced to unbalanced or even to a completely dephased SSFP signal at TE. A decrease of the voxel size might be considered to mitigate those problems. Another more general problem is that the fitting procedure might become more sensitive with lower SNR. A correct fitting is therefore only guaranteed with sufficient resolution and the use of multiple receiver coils.

The methods proposed in this work address two different aspects: First, lengthy acquisition times are reduced by undersampling and a compressed sensing reconstruction using the Fourier transformed bSSFP profile as sparse domain. Second, banding artifacts that become even more severe with low flip angles are removed by using a dictionary-fitting algorithm and synthetic contrasts.

3.5 Conclusion

A compressed sensing reconstruction of a series of highly undersampled phase-cycled bSSFP images in combination with a dictionary-based fitting algorithm can be used to reconstruct banding artifact-free genuine bSSFP images, which we termed *trueCISS*. Moreover, synthetic bSSFP contrast images can be derived from the intrinsic parameter estimates, for example, the flip angle independent maxCISS signal, or enhanced tissue-fluid contrast images achieved at high flip angles, which are not possible to acquire directly due to either physical or safety constraints. From this, trueCISS might help to extend bSSFP

imaging to a wider range of clinical applications.

Acknowledgment

This work was supported in part by a grant from the Swiss National Science Foundation (SNF 325230-153332).

References

- [1] H Y Carr. “Steady-State Free Precession in Nuclear Magnetic Resonance”. In: *Phys. Rev.* 112.5 (1958), pp. 1693–1701. DOI: 10.1103/PhysRev.112.1693 (cit. on p. 51).
- [2] Klaus Scheffler *et al.* “Principles and applications of balanced SSFP techniques”. In: *Eur. Radiol.* 13.11 (2003), pp. 2409–2418. DOI: 10.1007/s00330-003-1957-x (cit. on p. 51).
- [3] J W Casselman *et al.* “Constructive interference in steady state-3DFT MR imaging of the inner ear and cerebellopontine angle”. In: *AJNR Am J Neuroradiol Am. J. Neuroradiology* 14.1 (1993), pp. 47–57. URL: <http://www.ajnr.org/content/14/1/47> (cit. on p. 51).
- [4] Shreyas S. Vasanawala *et al.* “Linear combination steady-state free precession MRI”. In: *Magn. Res. Med.* 43.1 (2000), pp. 82–90. DOI: 10.1002/(SICI)1522-2594(200001)43:1<82::AID-MRM10>3.0.CO;2-9 (cit. on p. 51).
- [5] Neal K. Bangerter *et al.* “Analysis of Multiple-Acquisition SSFP”. In: *Magn. Res. Med.* 51.5 (2004), pp. 1038–1047. DOI: 10.1002/mrm.20052 (cit. on p. 51).
- [6] Tolga Çukur *et al.* “Enhanced spectral shaping in steady-state free precession imaging”. In: *Magn. Res. Med.* 58.6 (2007), pp. 1216–1223. DOI: 10.1002/mrm.21413 (cit. on p. 51).
- [7] Ray Freeman *et al.* “Phase and intensity anomalies in fourier transform NMR”. In: *J. Magn. Res.* 4 (1971), pp. 366–383. DOI: 10.1016/0022-2364(71)90047-3 (cit. on p. 51).

- [8] Tobias Knopp *et al.* “Iterative off-resonance and signal decay estimation and correction for multi-echo MRI”. In: *IEEE Trans. Medical Img.* 28.3 (2009), pp. 394–404. DOI: 10.1109/TMI.2008.2006526 (cit. on p. 51).
- [9] Marcus Björk *et al.* “Parameter estimation approach to banding artifact reduction in balanced steady-state free precession.” In: *Magn. Res. Med.* 00 (2013). DOI: 10.1002/mrm.24986 (cit. on p. 51).
- [10] Qing-San Xiang *et al.* “Banding artifact removal for bSSFP imaging with an elliptical signal model”. In: *Magn. Res. Med.* 71.3 (Mar. 2014), pp. 927–933. DOI: 10.1002/mrm.25098 (cit. on p. 51).
- [11] Michael N. Hoff *et al.* “Combined geometric and algebraic solutions for removal of bSSFP banding artifacts with performance comparisons”. In: *Magn. Res. Med.* (Mar. 2016), n/a–n/a. DOI: 10.1002/mrm.26150 (cit. on p. 51).
- [12] Michael Lustig *et al.* “Sparse MRI: The application of compressed sensing for rapid MR imaging”. In: *Magn. Res. Med.* 58.6 (2007), pp. 1182–1195. DOI: 10.1002/mrm.21391 (cit. on pp. 51, 54).
- [13] M. Lustig *et al.* “k-t SPARSE: high frame rate dynamic MRI exploiting spatio-temporal sparsity”. In: *Proceedings 13th Scientific Meeting, International Society for Magnetic Resonance in Medicine, Seattle*. May 2006, p. 2420 (cit. on p. 51).
- [14] Tolga Cukur. “Accelerated Phase-Cycled SSFP Imaging With Compressed Sensing”. In: *IEEE Trans. Medical Img.* 34.1 (2015), pp. 107–115. DOI: 10.1109/TMI.2014.2346814 (cit. on p. 51).
- [15] Efe Ilicak *et al.* “Profile-encoding reconstruction for multiple-acquisition balanced steady-state free precession imaging”. In: *Magn. Res. Med.* (Nov. 2016). DOI: 10.1002/mrm.26507 (cit. on p. 51).
- [16] Robert Bridson. “Fast Poisson Disk Sampling in Arbitrary Dimensions”. In: *Engineering* (2006), pp. 1–1. DOI: 10.1145/1278780.1278807 (cit. on p. 53).
- [17] Herman Tulleken. *Poisson Disk Sampling*. 2009. URL: <http://devmag.org.za/2009/05/03/poisson-disk-sampling/> (visited on 02/05/2016) (cit. on p. 53).
- [18] S. S. Vasanawala *et al.* “Practical parallel imaging compressed sensing MRI: Summary of two years of experience in accelerating body MRI of pediatric patients”. In: *Proc. - Int. Symp. Biomed. Imaging*. 2011, pp. 1039–1043. DOI: 10.1109/ISBI.2011.5872579 (cit. on p. 53).
- [19] Daniel Brenner *et al.* “Two-dimensional accelerated MP-RAGE imaging with flexible linear reordering”. In: *MAGMA* 27.5 (2014), pp. 455–462. DOI: 10.1007/s10334-014-0430-y (cit. on p. 53).
- [20] E Mark Haacke *et al.* *Magnetic Resonance Imaging: Physical Principles and Sequence Design*. Vol. 1st. 1999, p. 914. DOI: 10.1063/1.3554697 (cit. on pp. 53, 55).
- [21] Martin Uecker *et al.* “ESPIRiT - An eigenvalue approach to autocalibrating parallel MRI: Where SENSE meets GRAPPA”. In: *Magn. Res. Med.* 71.3 (2014), pp. 990–1001. DOI: 10.1002/mrm.24751 (cit. on pp. 53, 54).
- [22] Oliver Bieri. “An analytical description of balanced steady-state free precession with finite radio-frequency excitation”. In: *Magn. Res. Med.* 65.2 (2011), pp. 422–431. DOI: 10.1002/mrm.22626 (cit. on p. 53).
- [23] Julia V. Velikina *et al.* “Accelerating MR parameter mapping using sparsity-promoting regularization in parametric dimension”. In: *Magn. Res. Med.* 70.5 (2013), pp. 1263–1273. DOI: 10.1002/mrm.24577 (cit. on p. 54).
- [24] M Guerquin-Kern *et al.* “A fast wavelet-based reconstruction method for magnetic resonance imaging.” In: *IEEE Trans. Medical Img.* 30.9 (2011), pp. 1649–60. DOI: 10.1109/TMI.2011.2140121 (cit. on p. 54).
- [25] Y. Zur *et al.* “Motion-insensitive, steady-state free precession imaging”. In: *Magn. Res. Med.* 16.3 (1990), pp. 444–459. DOI: 10.1002/mrm.1910160311 (cit. on p. 54).

Chapter 3. True Constructive Interference in the Steady State (trueCISS)

- [26] Carl Ganter. “Static susceptibility effects in balanced SSFP sequences”. In: *Magn. Res. Med.* 56.3 (July 6, 2006), pp. 687–691. DOI: 10.1002/mrm.20986 (cit. on p. 54).
- [27] Feng Huang *et al.* “A rapid and robust numerical algorithm for sensitivity encoding with sparsity constraints: Self-feeding sparse SENSE”. In: *Magn. Res. Med.* 64.4 (2010), pp. 1078–1088. DOI: 10.1002/mrm.22504 (cit. on p. 54).
- [28] Damien Nguyen *et al.* “Motion-insensitive rapid configuration relaxometry”. In: *Magn. Res. Med.* (2016), n/a–n/a. DOI: 10.1002/mrm.26384 (cit. on p. 54).
- [29] Dan Ma *et al.* “Magnetic resonance fingerprinting. (1)”. In: *Nature* 495.7440 (2013), pp. 187–192. DOI: 10.1038/nature11971 (cit. on p. 56).
- [30] M. Gloor *et al.* “Quantitative magnetization transfer imaging using balanced SSFP”. In: *Magn. Res. Med.* 60.3 (2008), pp. 691–700. DOI: 10.1002/mrm.21705 (cit. on p. 61).
- [31] K L Miller. “Asymmetries of the balanced SSFP profile. Part I: theory and observation”. In: *Magn. Res. Med.* 63.2 (2010), pp. 385–395. DOI: 10.1002/mrm.22212 (cit. on p. 61).
- [32] I Chatnuntawech *et al.* “Fast reconstruction for accelerated multi-slice multi-contrast MRI.” In: *Biomed. Imaging (ISBI), 2015 IEEE 12th Int. Symp. on. IEEE.* 2015, pp. 335–338. DOI: 10.1109/ISBI.2015.7163881 (cit. on p. 61).

4 Configuration-Based bSSFP Parameter Estimation and its Application to trueCISS Imaging at Ultra-High Fields

Damien Nguyen^{1,2,†}, Tom Hilbert^{3,4,5,†}, Carl Ganter⁶, Philipp Ehses^{7,8,9}, Klaus Scheffler^{7,8}, Benjamin R. Knowles¹⁰, Mark E. Ladd^{10,11}, Tobias Kober^{3,4,5} and Oliver Bieri^{1,2}

¹Division of Radiological Physics, Department of Radiology, University Hospital Basel, University of Basel, Basel, Switzerland

²Department of Biomedical Engineering, University of Basel, Basel, Switzerland

³Advanced Clinical Imaging Technology (HC CEMEA SUI DI PI), Siemens Healthcare AG, Lausanne, Switzerland

⁴LTS5, École Polytechnique Fédérale de Lausanne, Lausanne, Switzerland

⁵Department of Radiology, University Hospital (CHUV), Lausanne, Switzerland

⁶Department of Radiology, Klinikum rechts der Isar, Technical University of Munich, Munich, Germany

⁷High-Field Magnetic Resonance Center, Max Planck Institute for biological Cybernetics, Tübingen, Germany

⁸Department for Biomedical Magnetic Resonance, University of Tübingen, Tübingen, Germany

⁹German Center for Neurodegenerative Diseases (DZNE), Bonn, Germany

¹⁰Division of Medical Physics, German Cancer Research Center (DKFZ), Heidelberg, Germany

¹¹Faculty of Physics and Astronomy and Faculty of Medicine, University of Heidelberg, Heidelberg, Germany

† equally contributing authors

4.1 Introduction

Balanced steady state free precession (bSSFP) imaging typically requires a short repetition time (TR) to mitigate off-resonances that can lead to prominent signal losses, also known as banding artefacts [1, 2]. As a result, acquiring multiple bSSFP images is a common approach to remove off-resonance related image artifacts. To this end, bSSFP scans are acquired with different radio-frequency (RF) phase increments (phase-cycling) and banding artifacts are subsequently removed using appropriate image combination methods, such as maximum intensity projection [2], complex sum [3], sum-of-squares or magnitude sum [4], among others [5] - usually known as Constructive Interference in the Steady State (CISS) [2]. The imaging is typically performed with high flip angles, and thus shortening of the TR is not only limited by the gradient performance but also due to safety constraints related to energy deposition reflected by the specific absorption rate (SAR).

BSSFP imaging artefacts due to off-resonances aggravate, especially at ultra-high field (UHF) strengths due to both increasing field inhomogeneity and more restrictive flip angle limits stemming from SAR constraints. To address this problem, recent banding-suppression techniques focus on parameter-based approaches to retrieve tissue parameter maps and subsequently synthesize artifact-free bSSFP contrast images [6, 7] rather than combining multiple phase-cycled images. For example, efficient banding artifact suppression was demonstrated using a parameter-based two-dimensional dictionary fitting to multi-phase-cycled bSSFP data. Long acquisition times were avoided by an undersampling of k-space in combination with a compressed sensing reconstruction [8]. This approach, termed trueCISS, provided artifact-free and on-resonant bSSFP contrast images offering overall acquisition times similar to conventional CISS [2]. The dictionary-based parameter estimation method is based on a simultaneous estimation of both the local off-resonance and the relaxation times ratio.

In contrary to most parameter-based estimation methods relying on an analysis of the steady state magnetization in real space, we propose to

address the quantification problem by using configuration theory [9]. From an analysis of the decay properties of non-negative and negative configuration orders, both the local off-resonance and the relaxation times ratio are estimated using variable projection (VARPRO) [10]. The new configuration-based bSSFP signal reconstruction is then explored at 7 T and 9.4 T for trueCISS imaging to yield a variety of bSSFP contrasts within UHF safety constraints, which would otherwise not be possible to acquire.

4.2 Theory

We consider an equidistant train of instantaneous radio-frequency (RF) pulses with constant flip angle α and balanced gradient moments. For an isochromat with a constant phase increment ϑ within the repetition time (TR) interval and with given transverse (T_2) and longitudinal (T_1) relaxation times, the complex steady state magnetization immediately after the RF pulse is of the form

$$M^+(\vartheta) = \frac{ae^{-i\vartheta} + b}{c \cos \vartheta + d} \quad (4.1)$$

where

$$\begin{aligned} a &\triangleq -(1 - E_1)E_2 \sin \alpha \\ b &\triangleq (1 - E_1) \sin \alpha \\ c &\triangleq E_2(E_1 - 1)(1 + \cos \alpha) \\ d &\triangleq 1 - E_1 \cos \alpha - (E_1 - \cos \alpha)E_2^2 \end{aligned} \quad (4.2)$$

with the common definition $E_{1,2} \triangleq e^{-\text{TR}/T_{1,2}}$.

Notably, since the magnetisation M^+ is a periodic function of ϑ with 2π , the steady state can be expressed as an infinite series

$$M^+(\vartheta) = M_x + iM_y = \sum_{n=-\infty}^{\infty} e^{in\vartheta} M^{(n)} \quad (4.3)$$

enclosing all configuration orders $M^{(n)}$ [9].

We now consider the steady state magnetisation observed at time t , in the presence of noise n and for phase shifts $\vartheta_j \triangleq \frac{2\pi}{N}j \wedge j = 0, 1, \dots, N-1$

$$m_j(t, \vartheta_j) = e^{-\frac{t}{T_2}} e^{+i\vartheta_j \frac{t}{\text{TR}}} M^+(\vartheta_j) + n_j \quad (4.4)$$

Chapter 4. Configuration-based trueCISS at Ultra-High Fields

In the seminal work of Zur *et al.* [11], it was shown how the N -point discrete Fourier transform

$$z^{(n)} \triangleq \frac{1}{N} \sum_{j=0}^{N-1} \left(m_j e^{-i\vartheta_j t / \text{TR}} \right) e^{-i2\pi n j / N} \quad (4.5)$$

relates to the configuration orders $M^{(n)}$. For large enough N , this approximately yields

$$z^{(n)} \approx e^{-\frac{t}{T_2}} e^{in\vartheta} M^{(n)} + n^{(n)} \quad (4.6)$$

In practice, the phase shifts ϑ_j can be generated using RF phase increments φ_j that directly relate to the phase shifts via $\vartheta_j \equiv -\varphi_j$. In the following, we will use this configuration-based approach (Eq. (4.6)) to retrieve the local off-resonance ϑ and the relaxation times ratio $\Lambda \triangleq T_1/T_2$ from the sampled complex frequency response function (cf. Eq. (4.4)).

Configuration-based parameter estimation

As shown in [9], the decay of the configuration modes

$$M^{(n)} \propto \begin{cases} A^n & : n \geq 0 \\ A^{|n|-1} & : n < 0 \end{cases} \quad (4.7)$$

depends on a single factor $A < 1$, which in the limit of $\text{TR} \ll T_{1,2}$, takes the form

$$\begin{aligned} A &\approx \frac{\eta}{\eta + 2(1 + \sqrt{\eta + 1})} \\ \eta &\triangleq \frac{1 + \cos \alpha}{1 - \cos \alpha} \Lambda^{-1} \\ \Lambda &\triangleq T_1/T_2 \end{aligned} \quad (4.8)$$

and thus

$$\Lambda = \frac{1 + \cos \alpha}{1 - \cos \alpha} \frac{(1 - A)^2}{4A} \quad (4.9)$$

Combining Eqs. (4.6) and (4.7), the decay of non-negative (+) and negative (−) configuration orders is given by

$$y_{\pm}^{(n)} = a_{\pm} z_{\pm}^n + n_{\pm}^{(n)} \quad (4.10)$$

where we collected the order-dependent terms into a single factor

$$z_{+}^n \triangleq e^{in\vartheta} A^n, \quad z_{-}^n \triangleq e^{-in\vartheta} A^n \quad (4.11)$$

and thus

$$z_{+} \equiv \bar{z}_{-} \triangleq z \quad (4.12)$$

as expected from the theory.

Please note that the index n is not equivalent with the definition in Eqs. (4.6) and (4.7): it has the range $n \geq 0$ for both non-negative ($n \rightarrow n$) and negative ($|n| - 1 \rightarrow n$) configuration orders.

From Eq. (4.10), the general maximum likelihood (ML) problem using a minimum χ^2 estimation is of the form

$$\arg \min \chi^2 = \arg \min \left\| \mathbf{y} - \begin{bmatrix} a_{+} \mathbf{I}_n \\ a_{-} \mathbf{I}_n \end{bmatrix} \mathbf{z} \right\|_2^2 \quad (4.13)$$

using

$$\begin{aligned} \mathbf{z} &\triangleq [z^0, z^1, \dots, z^{N-1}]^T \\ \mathbf{y}_{\pm} &\triangleq [y_{\pm}^{(1)}, y_{\pm}^{(2)}, \dots, y_{\pm}^{(N)}]^T \\ \mathbf{y} &\triangleq [\mathbf{y}_{+} \ \bar{\mathbf{y}}_{-}]^T \end{aligned}$$

Following the variable projection (VARPRO) approach [10], we eliminate the explicit dependence of χ^2 on the linear parameters (a_{+} and \bar{a}_{-}) to determine the optimal \mathbf{z} and thus the off-resonance and the relaxation times ratio. To this end, we solve for $a_{+} \equiv a'_{+} + ia''_{+}$ (and analogously for $\bar{a}_{-} \equiv \bar{a}'_{-} + i\bar{a}''_{-}$)

$$\begin{aligned} \partial_{a'_{+}} \chi^2 = 0 \wedge \partial_{a''_{+}} \chi^2 = 0 \\ \partial_{\bar{a}'_{-}} \chi^2 = 0 \wedge \partial_{\bar{a}''_{-}} \chi^2 = 0 \end{aligned} \quad (4.14)$$

which, after a short calculation, yields

$$a_{+} = \frac{\langle \mathbf{z}, \mathbf{y}_{+} \rangle}{\langle \mathbf{z}, \mathbf{z} \rangle} \quad a_{-} = \frac{\langle \mathbf{z}, \bar{\mathbf{y}}_{-} \rangle}{\langle \mathbf{z}, \mathbf{z} \rangle} \quad (4.15)$$

Inserting Eq. (4.15) into Eq. (4.13) finally results in the following expression

$$\chi^2(\vartheta, A) = \langle \mathbf{y}, \mathbf{y} \rangle - \frac{|\langle \mathbf{z}, \mathbf{y}_{+} \rangle|^2}{\langle \mathbf{z}, \mathbf{z} \rangle} - \frac{|\langle \mathbf{z}, \bar{\mathbf{y}}_{-} \rangle|^2}{\langle \mathbf{z}, \mathbf{z} \rangle} \quad (4.16)$$

	7 T		9.4 T	
	Whole brain	3D slab	Whole brain	3D slab
Coil type	Head coil	Head coil	Head coil [12]	Head coil [12]
Coil channels	25 Tx/Rx	25 Tx/Rx	16 Tx/31 Rx	16 Tx/31 Rx
Orientation	Sagittal	Axial	Sagittal	Axial
Nb. phase cycles	16	16	16	16
Acc. factor	10	10	10	10
Flip angle [°]	15	15	15	15
Resolution [mm ³]	0.9 × 0.9 × 0.9	0.4 × 0.4 × 0.5	0.9 × 0.9 × 0.9	0.4 × 0.4 × 0.5
Imaging matrix	284 × 284 × 176	500 × 400 × 40	248 × 248 × 176	500 × 400 × 40
TR/TE [ms]	3.94 / 1.97	6.92 / 3.46	3.73 / 1.87	5.26 / 2.63
Slice overs. [%]	-	50	-	50
Scan time [min]	05:18	05:06	04:40	03:40

Table 4.1 – UHF scanning parameters for all the measurements presented in this work

4.3 Methods

Simulation and imaging

All numerical simulations, data analysis and visualizations are realized using MATLAB 9.2 (The MathWorks Inc., Natick, MA). Measurements and calibrations are performed on investigational 7 T and 9.4 T whole body systems (Siemens Healthcare, Erlangen, Germany) with actively shielded magnetic field gradient coils. Brain extraction was conducted manually for the slices presented in this work.

Imaging was performed using $N = 16$ phase-cycled and 10-fold incoherently undersampled bSSFP scans which are acquired over an equidistant range of radio-frequency (RF) phase increments $\varphi_j \triangleq -\frac{2\pi}{N}j \wedge j = 0, 1, \dots, N - 1$. The undersampled data is subsequently reconstructed using compressed sensing [8]. All the relevant scanning parameters used in the present work are collected in Table 4.1.

Dictionary-based fitting

As reported in [8], a two-dimensional dictionary-based fitting was used to retrieve voxel-wise estimates for Λ and ϑ from the reconstructed volumes followed by the estimation of a scaling factor proportional to the equilibrium magnetization M_0 to match simulated and experimental signals (see also [13] for details on the analytical signal model).

Configuration-based fitting

A derivative-free multivariate local minimum search Nelder-Mead simplex method [14] used by the `fminsearch` function in MATLAB was performed on Eq. (4.16) to retrieve an estimate for the local off-resonance ϑ and the relaxation-dependent parameter A . As a starting value, z (and thus ϑ and A , cf. Eqs. (4.6) and (4.7)) was estimated from Eq. (4.10) e.g. using a rank one matrix pencil [15] analysis on the non-negative configuration decay. In this work, only the first four non-negative and negative configuration orders were considered for the VARPRO estimation of Λ and ϑ .

From the retrieved parameter maps and in combination with the signal model (Eq. (4.1)), an on-resonant bSSFP contrast image can be derived, termed trueCISS, as well as artificial bSSFP contrasts for any arbitrary choice of the flip angle α .

4.4 Results

A comparison of the results from multi-dimensional dictionary-based parameter fitting and the proposed configuration-based estimation method is shown for the relaxation times ratio in Fig. 4.1 and the local off-resonance in Fig. 4.2. Parameter maps were generated from the analysis of the bSSFP complex frequency response function retrieved from 16 ten-fold undersampled phase-cycled bSSFP scans acquired at 7 T and 9.4 T after a compressed sensing reconstruction. Overall, the new

configuration-based parameter mapping provides more robust results as compared to the dictionary-based fitting method, visible through smoother parameter maps with less speckle-like artifacts; this can be especially seen on the phase maps at 9.4 T for regions close to the ventricles that might be prone to residual phase-related inconsistencies due to physiological motion. We also observe a substantial increase of the T_1/T_2 -ratio between 7 T and 9.4 T; as expected from the increase in T_1 and decrease in T_2 with increasing field strength [16–21].

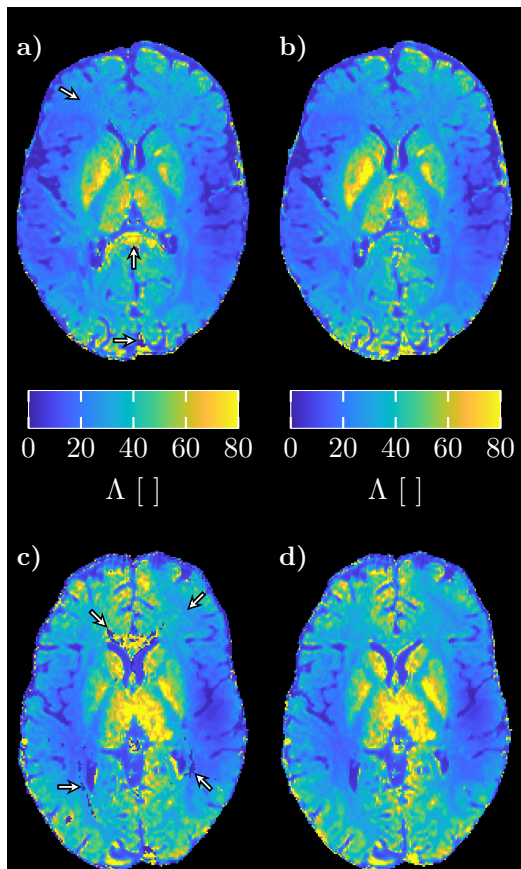


Figure 4.1 – Axial relaxation times ratio Λ parameter maps from the $0.9 \times 0.9 \times 0.9 \text{ mm}^3$ sagittally-acquired whole-brain datasets at 7 T **a** and **b**) and 9.4 T **c** and **d**). Λ is estimated using the original multi-dimensional dictionary fit **a** and **c**) and from the configuration-based approach **b** and **d**). The most prominent reconstruction artefacts are indicated by arrows.

From the configuration-based parameter maps, corresponding axial and sagittal trueCISS images are shown in Fig. 4.3. Overall, no image degradation from banding artefacts can be perceived over the whole volume. The apparent

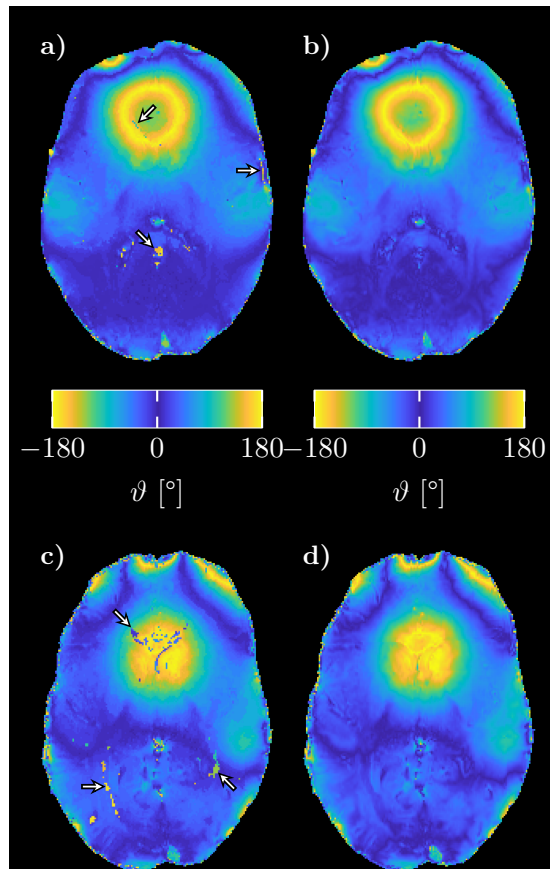


Figure 4.2 – Axial local off resonance ϑ parameter maps from the $0.9 \times 0.9 \times 0.9 \text{ mm}^3$ sagittally-acquired whole-brain datasets at 7 T **a** and **b**) and 9.4 T **c** and **d**). ϑ is estimated using the original multi-dimensional dictionary fit **a** and **c**) and from the configuration-based approach **b** and **d**). The most prominent reconstruction artefacts are indicated by arrows.

loss of signal in the 9.4 T data close to the nasal and buccal regions is likely the result of the sensitivity profile of the receive coil elements. Moreover, synthetic bSSFP contrast images in the high flip angle regime (50° and 90°) as well as the voxel-wise theoretical maximum bSSFP signal (maxCISS) are presented in Fig. 4.4 for both UHF datasets. At high flip angles, the contrast between fluids and tissues accentuates while the signal in the globus pallidus and thalamus markedly drops. This is a result of the high relaxation times ratios observed for these regions (see Fig. 4.1).

Finally, fast high-resolution trueCISS imaging is explored at UHF for voxel volumes as low as $0.45 \times 0.45 \times 0.5 \text{ mm}^3$ (Fig. 4.5), offering artifact-free imaging with minimal blurring from

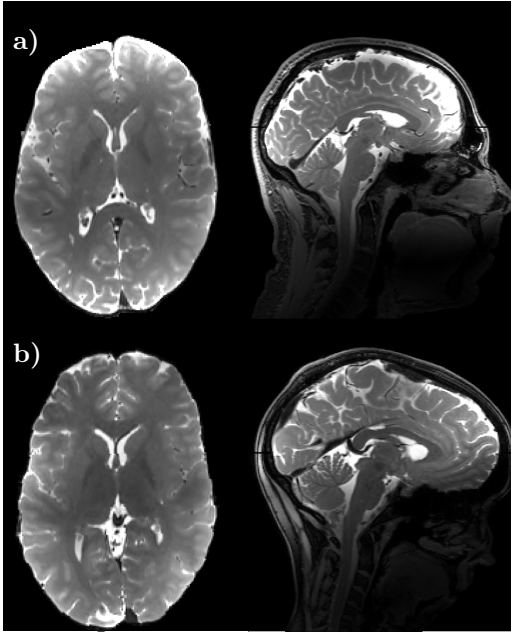


Figure 4.3 – Axial and sagittal slices from the $0.9 \times 0.9 \times 0.9 \text{ mm}^3$ sagittally-acquired whole-brain trueCISS acquisitions at 7 T **a** and 9.4 T **b** (TA 5 : 18 min and 4 : 40 min resp.). Reconstructions were performed using parameter maps derived with the configuration-based method.

the regularisation used in the compressed sensing reconstruction. In comparison to the whole brain datasets, the sharpness and visualisation of fine details, such as small blood vessels, is greatly increased.

4.5 Discussion

TrueCISS imaging does not require bSSFP imaging to be performed at high flip angles and can thus be used to overcome SAR constraints. This becomes especially important at UHF where the high flip angle regime of bSSFP, and thus contrasts at high flip angles, might only be reached using excessively long repetition times. Using a parameter-based approach offers not only the possibility to generate high-flip angle contrast images, but also to synthesize artificial contrasts, such as the theoretical maximum bSSFP signal for every voxel (see also Fig. 4.4 for both 7 T and 9.4 T acquisitions). However, accurate parameter estimation using the proposed configuration-based approach relies on proper estimation of the first

few configuration orders (cf. Eqs. (4.5) and (4.6)). Therefore, aliasing from the discrete Fourier transform should be avoided. Here, a set of $N = 16$ phase-cycled bSSFP scans was used, which is appropriate for tissues for modes up to at least the 4th order [11].

In contrast to the frontal white matter (Λ_{WM}), the central brain regions, such as the thalamus (Λ_T) and the putamen (Λ_P), showed much higher relaxation time ratios. This is in agreement with the literature, where a higher concentration of iron is expected for the basal ganglia, with maximum iron concentration found in the globus pallidus [22]. In comparison to studies based on spin-echo measurements [16–21], at 7 T values of $\Lambda_{WM} = 24 \pm 3$ (literature 30 – 35), $\Lambda_P = 51 \pm 8$ (literature 40 – 50), $\Lambda_T = 50 \pm 4$ (literature 35 – 40) are observed, whereas at 9.4 T for similar regions $\Lambda_{WM} = 32 \pm 3$ (literature 40 – 50), $\Lambda_P = 51 \pm 8$ (literature 60 – 70) and $\Lambda_T = 65 \pm 16$ (literature 45 – 55) have been measured. Overall, the Λ values are in a good range for the putamen, but the values appear to be slightly above the expected range for the thalamus and below the expectations for the frontal white matter. It might be noteworthy here that our Λ -maps were not corrected for B_1 field inhomogeneities. Generally, Λ -values become overestimated with positive deviations from the nominal flip angle (underestimated flip angles), but underestimated with negative deviations (overestimation of flip angles). Especially at UHF, the B_1 field is expected to be markedly inhomogeneous, typically featuring a prominent drop from the center to the periphery [12]. This would predict an overestimation of Λ in the center, such as for the thalamus, an underestimation in the periphery which includes the frontal white matter, and relatively unbiased values in the middle like for instance for the putamen; in excellent agreement with our observations.

As UHF slowly finds its way into clinical applications, robust parameter estimation methods, such as configuration-based estimation techniques, in combination with synthetic, parameter-based, artificial contrast methods such as trueCISS offer access to the whole range of bSSFP image contrasts explored at low fields.

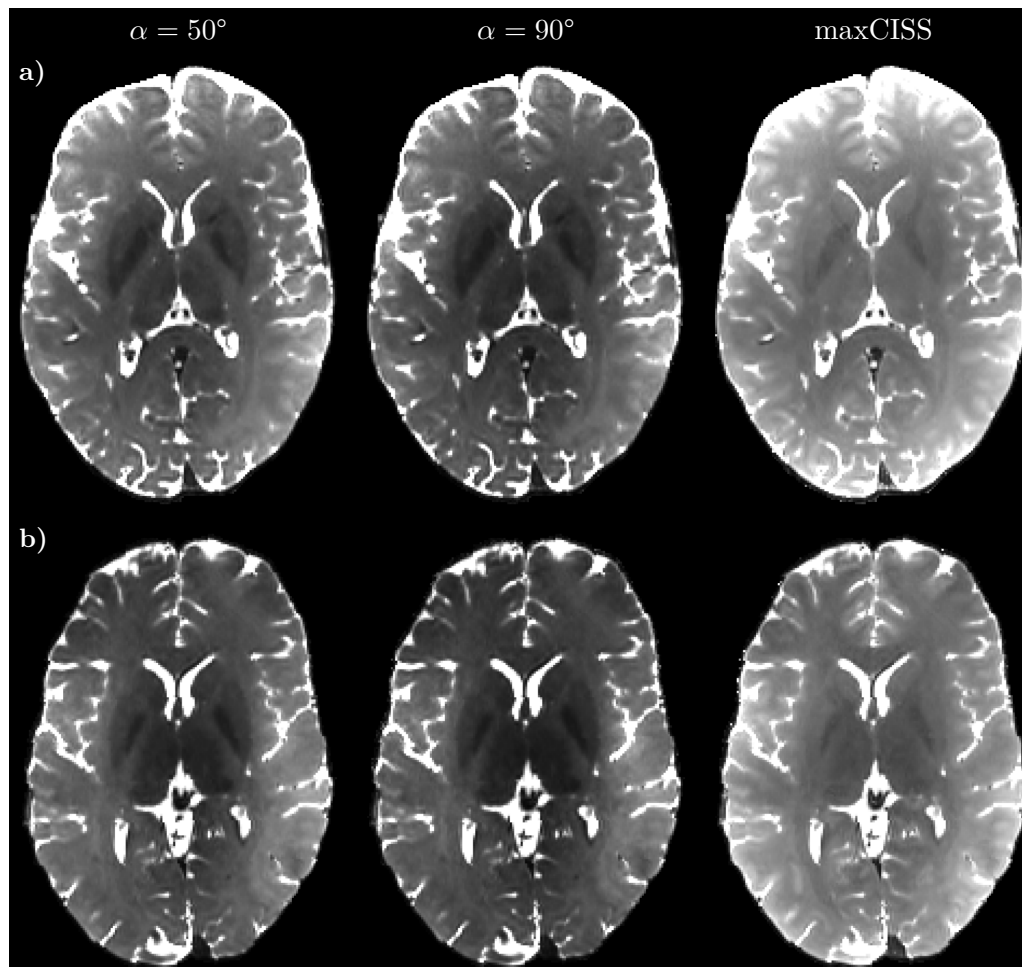


Figure 4.4 – Axial trueCISS reconstructions for flip angles 50° and 90° trueCISS and theoretical maximal bSSFP signal intensity (maxCISS) reconstruction from 3D sagittally-acquired whole-brain non-selective scans at 7T **a** and 9.4T **b** (see Fig. 4.3;TA 5 : 18 min and 4 : 40 min resp.). Each flip angle has been windowed independently to optimise visualisation. Virtually no reconstruction artefacts are visible giving a good indication of the quality of estimation and fitting of the configuration-based trueCISS reconstruction.

4.6 Conclusion

By developing configuration-based principal bSSFP parameter estimation theory, we are able to significantly improve the stability and quality of the trueCISS reconstruction even at ultra-high field strengths.

Acknowledgment

This work was supported in part by a grant from the Swiss National Science Foundation (SNF 325230-153332).

References

- [1] H Y Carr. “Steady-State Free Precession in Nuclear Magnetic Resonance”. In: *Phys. Rev.* 112.5 (1958), pp. 1693–1701. DOI: 10.1103/PhysRev.112.1693 (cit. on p. 67).
- [2] J W Casselman *et al.* “Constructive interference in steady state-3DFT MR imaging of the inner ear and cerebellopontine angle”. In: *AJNR Am J Neuroradiol Am. J. Neuroradiology* 14.1 (1993), pp. 47–57. URL: <http://www.ajnr.org/content/14/1/47> (cit. on p. 67).

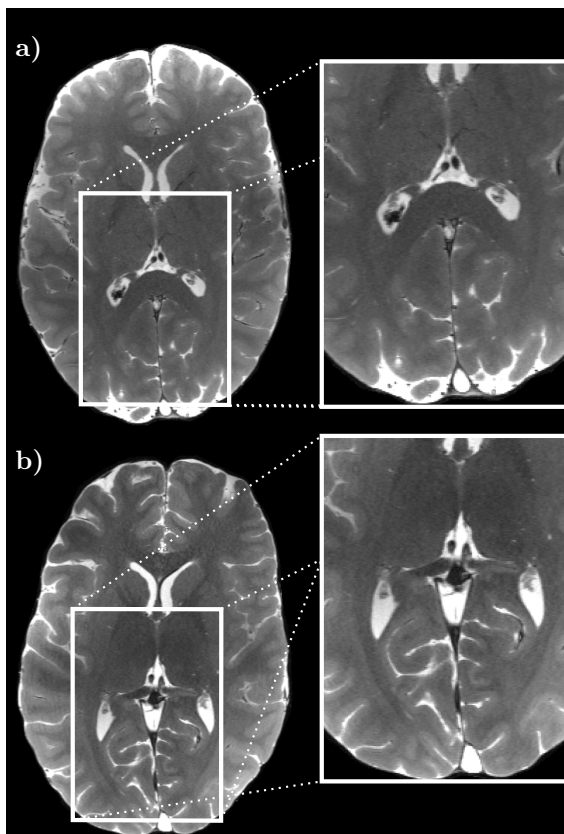


Figure 4.5 – Axial slices from high-resolution $0.45 \times 0.45 \times 0.50 \text{ mm}^3$ axial 3D trueCISS acquisitions at 7 T **a** and 9.4 T **b** using the parameter maps derived with the configuration-based method (TA 5 : 6 min and 3 : 40 min resp.). The panels on the right show an enlarged view of the marked regions on the left images.

- [3] Shreyas S. Vasanawala *et al.* “Linear combination steady-state free precession MRI”. In: *Magn. Res. Med.* 43.1 (2000), pp. 82–90. DOI: 10.1002/(SICI)1522-2594(200001)43:1<82::AID-MRM10>3.0.CO;2-9 (cit. on p. 67).
- [4] Neal K. Bangerter *et al.* “Analysis of Multiple-Acquisition SSFP”. In: *Magn. Res. Med.* 51.5 (2004), pp. 1038–1047. DOI: 10.1002/mrm.20052 (cit. on p. 67).
- [5] Tolga Çukur *et al.* “Enhanced spectral shaping in steady-state free precession imaging”. In: *Magn. Res. Med.* 58.6 (2007), pp. 1216–1223. DOI: 10.1002/mrm.21413 (cit. on p. 67).
- [6] Qing-San Xiang *et al.* “Banding artifact removal for bSSFP imaging with an elliptical signal model”. In: *Magn. Res. Med.* 71.3 (Mar. 2014), pp. 927–933. DOI: 10.1002/mrm.25098 (cit. on p. 67).
- [7] Marcus Björk *et al.* “Parameter estimation approach to banding artifact reduction in balanced steady-state free precession.” In: *Magn. Res. Med.* 00 (2013). DOI: 10.1002/mrm.24986 (cit. on p. 67).
- [8] Tom Hilbert *et al.* “True constructive interference in the steady state (trueCISS)”. In: *Magn. Res. Med.* (July 2017), pp. 1901–1910. DOI: 10.1002/mrm.26836 (cit. on pp. 67, 69).
- [9] Carl Ganter. “Static susceptibility effects in balanced SSFP sequences”. In: *Magn. Res. Med.* 56.3 (July 6, 2006), pp. 687–691. DOI: 10.1002/mrm.20986 (cit. on pp. 67, 68).
- [10] Dianne P. O’Leary *et al.* “Variable projection for nonlinear least squares problems”. In: *Comp. Optim. App.* 54.3 (Apr. 2013), pp. 579–593. DOI: 10.1007/s10589-012-9492-9 (cit. on pp. 67, 68).
- [11] Y. Zur *et al.* “Motion-insensitive, steady-state free precession imaging”. In: *Magn. Res. Med.* 16.3 (1990), pp. 444–459. DOI: 10.1002/mrm.1910160311 (cit. on pp. 68, 71).
- [12] G. Shajan *et al.* “A 16-channel dual-row transmit array in combination with a 31-element receive array for human brain imaging at 9.4 T”. In: *Magn. Res. Med.* 71.2 (Feb. 2014), pp. 870–879. DOI: 10.1002/mrm.24726 (cit. on pp. 69, 71).
- [13] Oliver Bieri. “An analytical description of balanced steady-state free precession with finite radio-frequency excitation”. In: *Magn. Res. Med.* 65.2 (2011), pp. 422–431. DOI: 10.1002/mrm.22626 (cit. on p. 69).
- [14] Jeffrey C. Lagarias *et al.* “Convergence Properties of the Nelder–Mead Simplex Method in Low Dimensions”. In: *SIAM J. Optim.* 9.1 (Jan. 1998), pp. 112–147. DOI: 10.1137/S1052623496303470 (cit. on p. 69).
- [15] Yung-Ya Lin *et al.* “A Novel Detection–Estimation Scheme for Noisy NMR Signals: Applications to Delayed Acquisition Data”. In: *J. Magn. Res.* 128.1 (1997), pp. 30–41. DOI: 10.1006/jmre.1997.1215 (cit. on p. 69).

Chapter 4. Configuration-based trueCISS at Ultra-High Fields

- [16] Randall LO. “Chemical Topography of the Brain”. In: *J. Biol. Chem.* 124 (1938), pp. 481–488. URL: <http://www.jbc.org/content/124/2/481.full.pdf?sid=351bb896-31d4-4ee8-adb7-17947746c97a> (cit. on pp. 70, 71).
- [17] B. Hallgren *et al.* “The Effect of Age on the Non-Haemin Iron in the Human Brain”. In: *J. Neurochem.* 3.1 (Oct. 1958), pp. 41–51. DOI: 10.1111/j.1471-4159.1958.tb12607.x (cit. on pp. 70, 71).
- [18] Neil Gelman *et al.* “Interregional variation of longitudinal relaxation rates in human brain at 3.0 T: Relation to estimated iron and water contents”. In: *Magn. Res. Med.* 45.1 (Jan. 2001), pp. 71–79. DOI: 10.1002/1522-2594(200101)45:1<71::AID-MRM1011>3.0.CO;2-2 (cit. on pp. 70, 71).
- [19] William D. Rooney *et al.* “Magnetic field and tissue dependencies of human brain longitudinal $^1\text{H}_2\text{O}$ relaxation in vivo”. In: *Magn. Res. Med.* 57.2 (Feb. 2007), pp. 308–318. DOI: 10.1002/mrm.21122 (cit. on pp. 70, 71).
- [20] Fumiyuki Mitsumori *et al.* “Toward understanding transverse relaxation in human brain through its field dependence”. In: *Magn. Res. Med.* 68.3 (Sept. 2012), pp. 947–953. DOI: 10.1002/mrm.23301 (cit. on pp. 70, 71).
- [21] Jinxia Zhu *et al.* “Relaxation measurements in brain tissue at field strengths between 0.35T and 9.4T”. In: *Proceedings 22nd Scientific Meeting, International Society for Magnetic Resonance in Medicine*. May 2014, p. 6286 (cit. on pp. 70, 71).
- [22] Domenico Aquino *et al.* “Age-related Iron Deposition in the Basal Ganglia: Quantitative Analysis in Healthy Subjects”. In: *Radiol.* 252.1 (July 2009), pp. 165–172. DOI: 10.1148/radiol.2522081399 (cit. on p. 71).

5 Conclusion

5.1 Summary

Within the framework of this thesis, new MRI methods based on bSSFP have been proposed, investigated and characterised in preliminary studies to develop fast, accurate and precise quantification of relaxation times as well as other important MR signal parameters, for possible future applications in the clinical routine. The main results, pointing out a few of the limitations of the approaches presented in this thesis, are summarised below for each chapter separately.

Chapter 2. Simulations and water phantom studies of the 3D motion insensitive rapid configuration relaxometry (MIRACLE) MRI technique at 3 T have demonstrated similar properties as the original triple echo steady-state relaxometry method [1]. Indeed, the estimation of T_1 and T_2 remains virtually unaffected by T_1 on T_2 or T_2 on T_1 biases, as well as negligible dependency on B_1 in the case of T_2 . However, due to the Fourier transformation of the bSSFP frequency response used in the estimation of the lower configuration orders, the relaxometry estimates, in particular for T_1 in the white matter, become sensitive to the underlying tissue micro-structure. Based on data in this study, as well as more recent comparisons between various T_1 -mapping techniques [2], the bias observed here seems only to be found in MIRACLE- T_1 estimates and thus may be an indication of a particular sensitivity that could potentially be the source of clinically relevant information in the future.

Chapter 3. Both studies in phantom and *in vivo* at 3 T have demonstrated that artefact-free on-resonant bSSFP images can be obtained from sixteen 8-fold undersampled bSSFP acquisitions using the proposed compressed sensing and dictionary-fitting methods without requiring additional acquisition time in comparison to conventional banding artefacts mitigation techniques. In addition, the quantitative nature of the method also allows the reconstruction of synthetic images that may not be otherwise acquirable due to safety constraints.

Chapter 4. The original trueCISS method is extended by using configuration-based parameter mapping and tested on the brain of healthy volunteers at ultra high field strengths (7 T and 9.4 T). The new improved quantification algorithm is shown to generate more robust quantification results than the original dictionary-fitting approach, therefore further improving artefact reduction in bSSFP images even at ultra-high field. However, compared to reference literature data for the relaxation times ratio, the values for that ratio in a few regions exhibit significantly overestimated values, particularly at 9.4 T. This could be linked to a combination of larger B_1 inhomogeneities and differences in the iron concentration depending on the regions considered.

5.2 Future work

Generally, gathering a better understanding of the complex relationship between the causes behind the asymmetries of the bSSFP frequency response and their effects on the configurations could lead to the development of novel techniques for improved diagnosis of brain diseases such as multiple sclerosis or characterisation of evolutionary processes like the myelination of the brain in infants. Early studies of the bSSFP frequency response profile (FRP) by Miller [3] and Miller *et al.* [4], based on the simple metric of the signal difference between the two peaks of the FRP, have shown correlation between the asymmetry of the FRP and the orientation of the white matter tracts as measured by diffusion-tensor imaging. Using configuration theory [5], it is known that any asymmetry present in the intra-voxel frequency distribution will lead to measurable change in the decay rate of the amplitude of the configurations. This could provide a more robust and sensible way of characterising the asymmetry and give potentially more insights about the underlying tissue micro-structure. A preliminary exploratory study [6] looking only at the difference between the decay rates of positive and negative has already shown interesting contrast mechanisms that relate to some extent to the results presented in [3, 4]. However, more work is still required to fully understand the contrast mechanisms of the method and hopefully design improved metrics that will be able to better characterise subtle tissue alterations commonly associated with neurodegenerative disorders.

In addition, quantitative methods based on configuration theory, such as the one introduced in Chapter 2, will generally be affected by any asymmetry present within a voxel. While correcting for the bias introduced due to the FRP's asymmetry might be possible in some cases, it may be more worth looking at the bias itself as a possible indicator of physiological importance. For example, early results from a comparison between the most common T_1 -mapping methods to date and MIRACLE- T_1 [2] seem to show that some correlation exists between the deviation in T_1 and the myelin water fraction inside the human brain. If this is confirmed by subsequent investigations, the T_1 deviation might therefore represent a fast and reliable bio-marker for myelination and de-myelination processes in the brain, such as for the detection and diagnosis of multiple sclerosis.

Further improvements of the methods presented in this work could include further development of the configuration-based quantification method described in Chapter 4 and combine the relaxation times ratio estimation with an iterative search for T_1 and T_2 in order to achieve more stable estimation of relaxation times than those achieved by MIRACLE. This, in combination with trueCISS imaging, could pave the way for very fast and accurate T_1 , T_2 and B_0 mapping of the human brain in clinically feasible times. Implementation of the reconstructions on the scanner hardware would also be desirable in order to distribute the sequence to other sites worldwide for further evaluations in various contexts.

In conclusion, this thesis explored the possibilities of developing quantification methods based exclusively on the balanced steady-state free precession sequence. The few new methods introduced here have the potential to offer useful tools and insights to researchers and clinicians in order to gain better understanding of the mysterious and wonderful machine that is the human body. My hope is that this work will in the future be used by others to further expand the knowledge and the diagnostic capabilities of MRI. However, irrespective of the progress of quantitative MRI in the future, it remains to be seen whether quantification actually provides significant benefits compared to conventional MR imaging methods when viewed from the perspective of automated and data-driven decision making and diagnostic processes based on artificial intelligence. This question will most definitely be answered in the near future, once hospitals manage to garner and automatically process the massive amount of data they generate on a daily basis. Hopefully within a few years, the validity of the quantification approach in MRI will have demonstrated its definite usefulness and have the path to its wider adoption in the clinical routines around the world sped up dramatically.

References

- [1] Rahel Heule *et al.* “Triple echo steady-state (TESS) relaxometry”. In: *Magn. Res. Med.* 71.1 (Apr. 2, 2013), pp. 230–237. DOI: 10.1002/mrm.24659 (cit. on p. 77).
- [2] Damien Nguyen *et al.* “On the sensitivity of T_1 mapping methods to myelin”. In: *Proceedings 26th Scientific Meeting, International Society for Magnetic Resonance in Medicine*. June 2018, p. 5486 (cit. on pp. 77, 78).
- [3] K L Miller. “Asymmetries of the balanced SSFP profile. Part I: theory and observation”. In: *Magn. Res. Med.* 63.2 (Jan. 23, 2010), pp. 385–395. DOI: 10.1002/mrm.22212 (cit. on p. 78).
- [4] K L Miller *et al.* “Asymmetries of the balanced SSFP profile. Part II: white matter”. In: *Magn Reson Med* 63.2 (2010), pp. 396–406. DOI: 10.1002/mrm.22249 (cit. on p. 78).
- [5] Carl Ganter. “Static susceptibility effects in balanced SSFP sequences”. In: *Magn. Res. Med.* 56.3 (June 2006), pp. 687–691. DOI: 10.1002/mrm.20986 (cit. on p. 78).
- [6] Damien Nguyen *et al.* “On the decay of SSFP configurations”. In: *Proceedings 25th Scientific Meeting, International Society for Magnetic Resonance in Medicine*. May 2017, p. 992 (cit. on p. 78).

Curriculum Vitae

Personal data

Name	Damien Nguyen
Date of birth	August 8, 1989
Place of birth	Lausanne VD
Place of citizenship	Val-de-Travers, NE

Education

Sept. 2014 – June 2018	PhD in Biophysics, University of Basel.
Sept. 2012 – July 2014	Master in Physics Engineering, Swiss Federal Institute of Technology Lausanne (EPFL)
Sept. 2011 – July 2012	Bachelor in Physics, Imperial College London
Sept. 2009 – July 2012	Bachelor in Physics, Swiss Federal Institute of Technology Lausanne (EPFL)
August 2005 – July 2008	Swiss high school degree, Gymnasium of Chamblandes, Pully VD, (main subject maths&physics), qualifying for university admittance